NORTHWESTERN UNIVERSITY

Synthesis and Catalysis Across a Series of Lanthanide Scandates

A DISSERTATION

SUBMITTED TO THE GRADUATE SCHOOL

IN PARTIAL FULFILLMENT OF THE REQUIREMENTS

for the degree

DOCTOR OF PHILOSOPHY

Field of Materials Science and Engineering

By

Emily P. Greenstein

EVANSTON, ILLINOIS

June 2024

ABSTRACT

Synthesis and Catalysis Across a Series of Lanthanide Scandates

Emily P. Greenstein

Designing heterogeneous catalysts–those in which an active metal is supported on a high-surface area substrate–is a complex challenge owing to the many ways the metal and support can interact. Lanthanide scandates, a series of perovskites of the form $LnScO_3$, are suited to studies of catalyst-support interactions because they retain many structure and property similarities as the lanthanide (Ln) is changed. Thorough characterization of a series of $LnScO_3$ supports enables catalytic performance to be attributed to precise changes in properties of the support, thus eliminating the confounding variables that would otherwise obscure metal-support interactions. This dissertation demonstrates the effectiveness of a series of five $LnScO_3$ (Ln = La, Pr, Nd, Sm, and Gd) through their synthesis, characterization, and catalytic testing.

Synthesis of high-purity (> 96 mol%) $LnScO_3$ is achieved via a hydrosauna approach guided by density functional theory (DFT). Hydrosauna synthesis applies humidity in an open system at near atmospheric pressure, in contrast to a typical sealed hydrothermal autoclave. In the hydrosauna method, too low water-vapor partial pressures inhibit

$LnScO_3$ particle growth, while an excess of water vapor results in undesired hydroxide and oxyhydroxide phases. The optimal humidity is shown to vary with the lanthanide in a non-monotonic manner: DFT is used to calculate the thermodynamics governing formation of undesired phases for each lanthanide, leading to precise prediction of the optimal water vapor pressure to synthesize faceted nanoparticles of each $LnScO_3$. Guided by these predictions, the partial pressures were observed to range from 1.0 torr (for synthesis of $LaScO_3$ and $GdScO_3$) to 8.5 torr (for $NdScO_3$ and $SmScO_3$)—much lower than the humidity of a typical lab.

DFT calculations for various $LnScO_3$, as well as established X-ray photoelectron spectroscopy measurements, indicate that their electronic structure gives rise to the non-monotonic behavior across the support series. The proximity of Ln 4f states to the Fermi energy for each $LnScO_3$ does not trend monotonically with the atomic number of the lanthanide but does correlate strongly with the strength of CO_2 chemisorption to the $LnScO_3$ surface. Pt/$LnScO_3$ catalysts are tested using CO oxidation and reverse water-gas shift to observe that reaction rates across the $LnScO_3$ series follow this non-monotonic trend in CO_2 binding strength. The Ln 4f electrons may cause an inductive effect which in turn allows neighboring oxygen atoms at the surface to better donate charge to species adsorbed on the metal. The binding of CO to $LnScO_3$-supported Pt metal is found to be governed by a combination of support effects, with contributions from both the electronic structure and the lattice parameter, which induces a strain at the Pt/$LnScO_3$ interface.

The consistent synthesis of well-faceted and highly phase pure $LnScO_3$ nanoparticles, combined with the understanding of how $LnScO_3$ electronic structure and properties change when varying the lanthanide ion, enables the use of the $LnScO_3$ series to identify

that strain affects Pt/$LnScO_3$ monotonically while electronic effects do not. This library of materials can therefore be applied to other reactions as trends in catalytic performance across the $LnScO_3$ series can indicate the most important properties for which to design new catalysts.

Acknowledgements

I would like to start by thanking my advisors, Professor Laurie Marks and Professor Ken Poeppelmeier, for their mentor-ship and support over the course of my Ph.D. Together and independently they have given me their patience, humor, encouragement, and a push when I needed it. From them I have learned everything from technical concepts to communicating effectively and "following the science." They have helped me grow as a scientist and as a person, and I will forever be grateful for the opportunity to work with them both.

I am very grateful to the members of my thesis committee and qualifying exam committee, Professor George Schatz and Professor Christopher Wolverton, for their encouragement and invaluable feedback. I would also like to acknowledge my funding through the Institute for Catalysis in Energy Processes, which received its funding from the U.S. Department of Energy Office of Basic Sciences, grant award number DE-FG02-03ER15457.

The work presented in this dissertation is the product of collaboration and technical support from many of Northwestern's experts. I'd like to thank Laurie once more for sharing his wealth of knowledge in electron microscopy and DFT. I'd also like to thank Ken for sharing his insight into chemistry and bonding, as well as his impressive knowledge of the scientific community; no matter the problem, Ken always knows where to look. Thank you also to Xiaobing Hu for all his assistance with the electron microscopes (and especially for helping us electron microscopy TA's) in EPIC, and to Zachary Mansley at

Northwestern and Jianguo Wen at Argonne National Lab for sharing their expertise in high-resolution TEM. Neil Schweitzer and Selim Alayoglu do amazing work in REACT, and I thank them for their support with many of the surface science and catalysis experiments in this work. I thank Jerry Carsello and Sumit Kewalramani for their hard work managing the Cohen X-Ray Facility. Thank you to Geun-Ho Han and GIANTFab for welcoming me into your lab to do ALD. Thank you to Ryan Paull, the pioneer of hydrosauna synthesis, for passing on to me his insights on the technique, and thank you to Robert Kennedy and Fenghua Ding for their support in designing and building the hydrosauna reactor on which most of my thesis work relies.

I have had the privilege of working with two amazing lab groups; I would like to extend my thanks to all KRP and LDM group members both past and present. Thank you to the Marks Group's other half, Karl, for reminding me to eat lunch and for being a great colleague, proofreader, and fellow man of science. Thank you to Kendall, who keeps me grounded, positive, and considerate of the cat's perspective. Thank you also to Patrick, whose calm in a crisis is infectious, as well as to Ian for many insightful discussions about chemistry and everything else. Thank you to Ryan for teaching me the ins and outs of synthesis and for providing the office music. Thank you to Chris and Tiffany answering my many questions with patience and thoughtfulness. Thank you to Zach for being a great collaborator and ANL road trip companion. In addition, I would like to express my gratitude to Bruce, Ella, Makayla, Ritesh, Alex, Peter, Evan, Michael, Chi, Matt, Steven, Jaye, Alessandro, Allison, Takumi, Sean, Anita, and all the rest for making the office(s) such a weird and wonderful place to work.

For filling my time at Northwestern with great adventures outside the lab as well as in it, I'd like to extend my thanks to Lele, Roger, Gwen, Sam, Dan, and the entire blessedly friendly and active MSE '18 cohort. I am so grateful for your camaraderie and company, and especially for all the times we have read books and kayaked rivers and noticed the line dislocations in our knitting.

Beyond Northwestern, many thanks to the professors and teachers who have nurtured my curiosity from the beginning.

Lastly, thank you to my family. To my sister, Nicole, who has always been my role model and my cheerleader. And, of course, thank you to my parents, the original Drs. Greenstein, who have supported me in every way there is to support a person. You gave me that itch for learning, and I will be forever grateful. Thank you to the moon and back.

List of Abbreviations

P_{H_2O}**:** water vapor partial pressure

ADF: annular dark field

ALD: atomic layer deposition

DFT: density functional theory

DRIFTS: diffuse reflectance infrared Fourier transform spectroscopy/spectra

HAADF: high-angle annular dark field

HREM: high resolution electron microscopy

ICP-MS: inductively coupled plasma mass spectrometry

ICP-OES: inductively coupled plasma optical emission spectrometry

pDOS: partial density of states

PXRD: powder X-ray diffraction

RWGS: reverse water-gas shift

SE: secondary electron

SMSI: strong metal-support interaction

STEM: scanning transmission electron Microscopy

STO: strontium titanate, $SrTiO_3$

TEM: transmission electron microscopy

TOF: turnover frequency

TPD-MS: temperature programmed desorption with simultaneous mass spectrometry

XPS: X-ray photoelectron spectroscopy

XRD: X-ray diffraction

Table of Contents

ABSTRACT 3

Acknowledgements 6

List of Abbreviations 9

Table of Contents 11

List of Tables 14

List of Figures 15

Chapter 1. Introduction 21

1.1. Motivation 21

1.2. Organization 29

Chapter 2. Experimental and Computational Methods 31

2.1. X-Ray Diffraction 31

2.2. Transmission Electron Microscopy 32

2.3. Atomic-Layer Deposition 36

2.4. Density Functional Theory 37

Chapter 3. Introduction to Hydrosauna Synthesis 39

3.1. Introduction 39

3.2. One-Line Hydrosauna Method 41

3.3. Back-Reactions: Effects of Water Vapor on Product Phases 45

3.4. In-Situ Hydrosauna Techniques 50

3.5. Conclusions 56

Chapter 4. Quantifying the Role of Water Vapor in Lanthanide Scandate Hydrosauna Synthesis 57

4.1. Introduction 57

4.2. Observing Environmental Effects on Hydrosauna Synthesis 60

4.3. Two-Line Hydrosauna Synthesis 63

4.4. Determining Optimal Water-Vapor Partial Pressures with DFT 64

4.5. Discussion 71

4.6. Conclusion 77

Chapter 5. Carbon Dioxide as a Probe for Electronic Effects in Lanthanide Scandate-Supported Gold 78

5.1. Introduction 78

5.2. Methods 79

5.3. Catalyst Characterization 81

5.4. CO Oxidation Over Au/$LnScO_3$ 85

5.5. Discussion 86

5.6. Conclusion 90

Chapter 6. CO Oxidation and Reverse Water-Gas Shift Over Lanthanide Scandate Supported Platinum 92

6.1. Introduction 92

6.2. Methods 94

6.3. Catalyst Characterization 96

6.4. Catalytic Performance of Pt/$LnScO_3$ 101

6.5. Role of Electronic Structure in Catalytic Performance 105

6.6. What Does the Compensation Effect Mean for Pt/$LnScO_3$? 109

6.7. Conclusion 112

Chapter 7. CO Chemisorption on Lanthanide Scandate Supported Platinum 114

7.1. Introduction 114

7.2. Methods 115

7.3. Estimating Strain Induced in Pt by $LnScO_3$ 118

7.4. CO Binding Configurations on Pt/$LnScO_3$ 123

7.5. Incorporating Non-Monotonic $LnScO_3$ Behavior: Bader Analysis 127

7.6. Conclusions 133

Chapter 8. Summary and Future Directions 136

8.1. Conclusions 136

8.2. Future Directions 137

References 154

Appendix A. Hydrosauna Synthesis Observations via In-Situ X-Ray Diffraction 178

Appendix B. Effects of Platinum Particle Size on CO DRIFTS 183

List of Tables

6.1 Apparent activation energy E_a, prefactor A, activation enthalpy $\Delta H^{\ddagger}$, and activation entropy $\Delta S^{\ddagger}$, calculated from observed reaction rates of CO oxidation and RWGS. 105

7.1 Lattice parameters of pseudocubic $LnScO_3$ and Pt nanoparticles supported on $LnScO_3$, and resulting strain induced in Pt by $LnScO_3$ supports. 122

7.2 Electron density at the Ln-O bonding critical point and Bader charge of the Ln atom for five $LnScO_3$ bulk structures. 130

8.1 Goldschmidt tolerance factors for $LnScO_3$ orthorhombic perosvkites. 146

List of Figures

1.1 Transmission electron micrograph of platinum nanoparticles supported on gadolinium scandate. 22

1.2 *Pbnm* orthorhombic perovskite structure of $LnScO_3$ and their pseudocubic lattice parameters. 28

3.1 Schematic of one-line hydrosauna tube furnace reactor. 42

3.2 Secondary electron scanning transmission electron microscopy images of $LaScO_3$ after each step of one-line hydrosauna synthesis. 43

3.3 SE STEM images of $LaScO_3$, $NdScO_3$, and $SmScO_3$ nanoparticles prepared via one-line hydrosauna synthesis. 43

3.4 SE STEM images of $NdScO_3$ nanoparticles from six different one-line hydrosauna synthesis batches. 45

3.5 Powder X-ray diffraction patterns of four different one-line hydrosauna synthesis $NdScO_3$ batches. 46

3.6 PXRD patterns of the products of three $NdScO_3$ syntheses cooled down by different means of quenching. 49

3.7 Raman spectra of $NdScO_3$ and its two precursor powders, Nd_2O_3 and Sc_2O_3. 53

3.8 In-situ Raman spectroscopy experimental set-up for $NdScO_3$ hydrosauna synthesis and Raman spectra localized to different regions of the sample. 55

4.1 PXRD patterns for the mixed-cation $GdSc(OH)_6 \cdot xH_2O$ ($x \approx 6$) gel precursor synthesized in various environments to test the role of the gel's water, accompanied by ADF and SE STEM images. 61

4.2 PXRD patterns of $NdScO_3$ synthesized under very wet and very dry conditions. 62

4.3 Schematic of the two-line hydrosauna tube furnace reactor. 63

4.4 PXRD patterns comparing $NdScO_3$ syntheses in one-line ($P_{H_2O} = 20$ torr) vs two-line ($P_{H_2O} = 10$ torr) hydrosauna syntheses. 65

4.5 Established experimental XPS valence spectra for $PrScO_3$, $NdScO_3$, $GdScO_3$, and $TbScO_3$. 67

4.6 DFT-calculated energy trends for the reactions $\frac{1}{2}Ln_2O_3 + \frac{3}{2}H_2O \rightarrow Ln(OH)_3$ and $LnOOH + H_2O \rightarrow Ln(OH)_3$ for multiple Ln, and corresponding P_{H_2O} that yields phase-pure $LnScO_3$ hydrosauna synthesis. 70

4.7 PXRD patterns of $LnScO_3$ (Ln = La, Pr, Nd, Sm, Gd) obtained via two-line hydrosauna synthesis, with ADF-STEM images of some of the nanoparticles produced. 71

4.8 PXRD patterns demonstrating how even small deviations from the calculated optimal P_{H_2O} affect the hydrosauna synthesis of $NdScO_3$ and $LaScO_3$. 72

4.9 Calculated partial density of states of various bulk $LnScO_3$. 74

5.1 SE STEM images of three different lanthanide scandate support nanoparticles, and aberration-corrected HREM of the $SmScO_3$ surface. 82

5.2 TPD-MS results illustrating the variation of the temperature dependence of CO_2 desorption on three different $LnScO_3$ substrates. 83

5.3 TEM image of Au nanopaticles on a $SmScO_3$ substrate, and average diameters of Au nanoparticles on three $LnScO_3$ supports. 84

5.4 Actiation energy and TOF of CO oxidation over Au/$LnScO_3$. 85

5.5 Density of states of $LaScO_3$, $NdScO_3$, and $SmScO_3$. 87

5.6 Proposed Eley-Rideal reaction pathway for CO oxidation over Au/$LnScO_3$. 89

6.1 Example experiment of CO oxidation over Pt/$NdScO_3$ showing flow and temperature conditions, CO conversion, and the Arrhenius relationship used to calculate reaction rate. 97

6.2 Variation of the temperature dependence of CO_2 desorption on five different $LnScO_3$ substrates, measured via TPD-MS. 99

6.3 CO_2 TPD-MS results normalized by $LnScO_3$ support surface area. 100

6.4 TEM images and size distributions of Pt nanoparticles supported on five different $LnScO_3$ substrates. 101

6.5 Bar graphs comparing CO oxidation rates of reaction for five different $Pt/LnScO_3$ catalysts, measured under two different O_2:CO ratios (40:1 and 16:1). 102

6.6 Bar graph depicting rates of RWGS over five different $Pt/LnScO_3$ catalysts. 103

6.7 Arrhenius plots for the reactions of various $Pt/LnScO_3$-catalyzed CO oxidation and RWGS reactions. 104

6.8 Plots displaying the relationship between activation enthalpy, $\Delta H^{\ddagger}$, and activation entropy, $\Delta S^{\ddagger}$, for both CO oxidation (where [O_2 109

6.9 Plot displaying the relationship between activation enthalpy, $\Delta H^{\ddagger}$, and activation entropy, $\Delta S^{\ddagger}$, for CO oxidation under a lower-O_2 condition (where O_2:CO is 16:1). 111

7.1 Representative electron micro-graphs of $NdScO_3$ and $Pt/NdScO_3$. 116

7.2 Schematic illustration of a DRIFTS experiment. 117

7.3 (a) Example Rietveld refinement on the XRD pattern of $Pt/LaScO_3$ used to measure the lattice parameter of $LaScO_3$ experimentally. (b) Plot of various pseudo-cubic $LnScO_3$ lattice parameters as a function of Ln. 119

7.4 Schematic representation of the strain experienced by a single Pt particle supported on a larger $LnScO_3$ substrate. 121

7.5 Schematics of CO bound to Pt in linear and bridged configurations. CO DRIFTS for each of five Pt/$LnScO_3$ catalysts. 124

7.6 Plot showing percentage of CO bound to Pt/$LnScO_3$ in a bridged configuration, as compared to the estimated Pt/$LnScO_3$ tensile strain. 126

7.7 Diagram illustrating how the charge density surface is used to define the volume associated with each atom in a molecule. 128

7.8 $LnScO_3$ *Pbnm* structure, viewed along [110], with the locations of the critical points in the charge density along Ln-O bonds indicated by the positions of pink spheres. 129

7.9 Structures of MgO, CuO, and Cu_2O with metal-oxygen bonding critical points highlighted by pink spheres. 130

7.10 Table displaying five $LnScO_3$ and the binary oxides MgO, CuO, and Cu_2O arranged in order of increasing ρ_{CP} or decreasing ionicity. 131

7.11 Plot illustrating a quantitative estimation of the relative role of the pseudocubic lattice parameter of $LnScO_3$ and the electron density at the Ln-O bond critical point in CO adsorption. 133

8.1 SE STEM images of $GdScO_3$ prepared via hydrosauna synthesis under two different carrier gas flow rates. 139

8.2 PXRD patterns and average crystallite sizes of $SmScO_3$ nanoparticles prepared via hydrosauna synthesis under two different carrier gas flow rates. 140

8.3 PXRD patterns of $DyScO_3$ made by hydrosauna synthesis. 148

8.4 PXRD pattern resulting from $TbScO_3$ hydrosauna synthesis. 149

8.5 PXRD pattern and Rietveld refinement of high-purity $MgCrMnO_4$ made via hydrosauna synthesis. 153

A.1 Illustration of in-situ XRD hydrosauna synthesis experimental set-up. 179

A.2 X-ray diffraction taken throughout heating and cooling of a $NdScO_3$ precursor gel. Only the alumina sample holder can be seen. 181

A.3 X-ray diffraction patterns of $NdScO_3$ both during and after in-situ hydrosauna synthesis. 182

B.1 DRIFTS of $Pt/SmScO_3$ after CO saturation for three different sizes of Pt. 183

CHAPTER 1

Introduction

1.1. Motivation

1.1.1. Supported Heterogeneous Catalysts

Heterogeneous catalysts, those with a different solid phase than the reactants or products, facilitate the global-scale control of emissions, production of food and industrially manufactured products, refinement of petroleum, and more.[**1, 2**] These catalysts generally function by adsorbing some reactants to provide a pathway for a chemical reaction to proceed. The products then desorb and escape, leaving the catalyst restored and still functional. A catalyst's surface contains its active sites; thus, its surface area and surface properties, such as adsorbate affinity or binding strength, determine its overall catalytic behavior. The catalyst must bind reactants to function, but product adsorbates that are too strongly bound will not quickly or easily be released again to free up the active site. This general phenomenon is known as Sabatier's principle.

The number of active sites provided by a given amount of catalytic material can be increased by using nanoparticles. Common catalysts such as nanoparticles of platinum (Pt) or gold (Au) are often supported on larger substrate particles to prevent their sintering or coarsening at reaction conditions. These supports should maintain a high overall catalyst surface area while being thermally stable. As such, a complete catalyst may consist of small metal nanoparticles, less than 5 nm in diameter, which are supported on larger

metal oxide particles.[**1**] An example of a supported metal catalyst is shown in Figure 1.1, where 3-5 nm Pt metal nanoparticles are supported on a 50 nm gadolinium scandate ($GdScO_3$) particle.

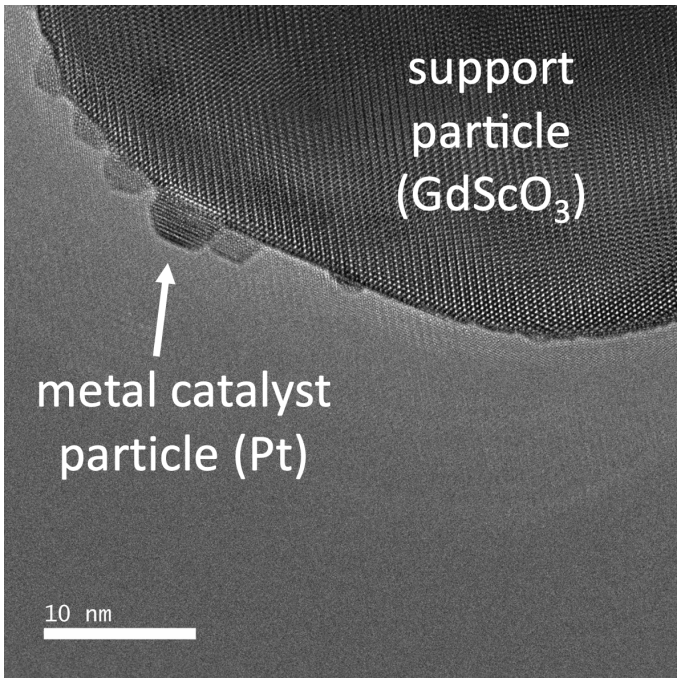

Figure 1.1. Transmission electron micrograph of platinum nanoparticles (3-5 nm diameter) supported on gadolinium scandate (20 nm width).

While supported catalysts augment efficiency by way of enhancing thermal stability and surface active site availability, they also complicate studies owing to the non-uniformity of interactions between the support and the metal catalyst. The role of the support material is not purely to prevent sintering, and both the basicity and epitaxial strain of catalytic nanoparticles can change the local coordination of active sites at nanoparticle/oxide/gas triple-points.[**3, 4, 5, 6**] Physical properties such as particle size[**7**] and available active sites at the metal-oxide interface[**8**] will also play a role. In addition, chemical bonding interactions between the catalyst and its support called

strong metal-support interactions, or SMSI's, can create an interfacial zone of either improved or suppressed catalytic activity depending on the catalyst and gases involved in the reaction.[**4, 5, 9**] For example, a reducible oxide support like TiO_2 can diffuse onto the metal surface when reduced, which may mask a significant portion of active sites for a given catalytic application. Irreducible supports like SiO_2, on the other hand, may not invade a metal surface as easily.[**10**]

Bearing in mind these potential interactions between support and catalyst materials, the study of heterogeneous catalysts is by nature interdisciplinary. Fundamental studies of supported catalyst systems requires bridging the gap between materials-focused characterization of model crystalline surfaces and the operation of complex high-surface area structures under the high-pressure, high-temperature demands of catalytic processes. There are two main components to this gap. The first is a "pressure gap," arising from the fact that many materials characterization techniques such as transmission electron microscopy (TEM) or X-ray photoelectron spectroscopy (XPS) generally operate at very low pressures (below 10^{-6} torr).[**1, 11**] Experimental results obtained using these methods must then be interpreted in the context of much more extreme reaction conditions, which can be achieved via extrapolation with computational models or with the development of advanced instrumentation.[**1**]

The focus of this dissertation is the second component to the gap, often called a "materials gap." This gap widens as catalyst design grows more informed and complex: research today highlights the synthesis, characterization, and use of high-surface area catalysts including increasingly complicated zeolites,[**12, 13**] mesoporous materials,[**14**] and

supported metal catalysts[**1, 5**]; see Figure 1.1. The model catalysts used in many experimental studies are single crystals cut at a variety of angles to expose desired structures.[**15**] While the chemistry and structure of surfaces of many of these crystals have been very well defined, they can differ greatly in nanomaterials of the same composition. High surface area catalysts present various surface facets, each potentially different from those exposed in the bulk or on polycrystalline supports, and each with different capabilities for selectivity and reactivity.[**6, 16**] As a result, many nanoparticle catalysts remain largely undefined, complicating the ability to design catalysts with particular surface properties and reactivity.

Bridging this materials gap requires controlling the surface properties of supports used in catalysis. Since the beginning of the twentieth century, the Wulff construction has been used to predict and describe the shape of free-standing metal nanoparticles.[**17**] It has also long been understood that a metal nanoparticle supported on a substrate will instead adopt the modified version of the Wulff construction known as a Winterbottom construction.[**18**] More recently, fundamental research has characterized nanoparticles in great detail, solving surface structures of metal nanoparticles,[**19**] epitaxial interfaces of metal-support interfaces,[**16**] and even complex and anomalous structures such as multiply-twinned particles.[**20**]

Proceeding in parallel to these fundamental nanoparticle studies, advances have also been made in understanding the role of these structures in heterogeneous catalysis.[**21**] At the metal-support interface, researchers have demonstrated electronic band bending[**22**] and epitaxial stabilization of catalysts[**23**] via control of exposed facets.[**16**] The vast array of support options available today creates opportunities for new systematic catalyst

studies. To predict which of an array of supports will yield the best catalytic activity for a given reaction, one must consider many support properties and metal-support interactions. Countless combinations of micro- and mesoporous materials, metal-organic frameworks, solid oxides, and metals will all have different surface chemistry, crystal symmetry, electronic structure, interfacial strain, and numerous other properties. Several reviews discuss the scope of metal-support interaction research, many highlighting how this diversity in support properties makes it difficult to elucidate overarching patterns in support effects.[**24, 25, 26, 27**] Often the supports are polycrystalline with many different surface facets, so catalytic performance is a statistical average over these. In such cases one cannot make clean conclusions about the role of the support. Instead, we need samples where only a limited number of variables change in a controlled fashion.

Important steps have been taken towards eliminating confounding variables to observe support effects caused by a single property. For example, Yan et al. have isolated strain from other support effects by depositing metal films on polymer substrates and applying strain externally with a mechanical tensing machine.[**28**] However, the polymer backing may not be truly inert; at higher strains, localized strain and interface debonding limit the generalizability of that study.[**29**] Other works have combined computational and experimental techniques to separate chemical, electronic, and mechanical effects,[**30**] but it is recognized that these are only applicable within a narrow window of strains and particle sizes. Fundamental research that can further the systematic design of catalysts, i.e. elucidating which particular support or interface properties contribute to a given catalytic behavior, will thus require experimental use of a family of support materials which are largely similar, but differ in a few key well-controlled ways.

The familiarity of the cubic ABO_3 perovskites, particularly strontium titanate ($SrTiO_3$, abbreviated STO), makes this family of materials a frequent choice for elucidating the role of the support.[**23, 31, 32**] STO has a robust record of demonstrated use in catalysis, including both technological advances[**33, 34**] and fundamental research.[**35, 36, 37**] Because STO is so well-studied as a model cubic perovskite,[**38, 39**] it provides a good stepping stone across the aforementioned materials gap. Advances in morphological control of STO have also made it possible to change its dominant surface facets or surface terminations, providing another approach towards isolating the effects of certain support factors.[**23, 32, 37**]

However, switching the A-site cation to another Group 2 element changes many properties that could contribute to metal-support effects. Consider, for example, barium titanate, or $BaTiO_3$ (BTO), a material often treated as an analog of STO.[**40**] Though a BTO unit cell is larger than that of STO, with a less electronegative A-site cation both have the same structure and TiO_2-rich surfaces, and share many other properties. Yet, they still differ in their defect chemistry and mechanisms of vacancy formation,[**40, 41**] which impacts these materials' interactions with adsorbates and thus the way they behave as catalytic supports. The same can be said of calcium titanate, $CaTiO_3$. All three of these perovskites have different photocatalytic behavior, electronic properties, and temperature- or synthesis-dependent morphology.[**42, 43, 44, 45**] Thus, these three chemically and structurally similar materials from the same family introduce a host of confounding variables that complicate how they are studied in the context of supported heterogeneous catalysis.

The goal of this work is to develop a set of materials that eliminates many of these confounding variables. Whereas $CaTiO_3$, $SrTiO_3$, and $BaTiO_3$ are all "2-4" perovskites (i.e. of the form $A^{2+}B^{4+}O_3$) in which switching the A-site cation with another from the same group will introduce a very different electronegativity, a series of "3-3" pervovskites ($A^{3+}B^{3+}O_3$) can be altered by switching the A-site cation with another from the same family. This dissertation focuses on 3-3 perovskites in which the A-site cation is a lanthanide ion. Switching that cation from one lanthanide to another in the series maintains a more similar structure and properties.

1.1.2. Lanthanide Scandates as Catalytic Supports

An ideal series of supports to use in studying metal-support interactions and designing catalysts will be chemically and structurally similar and will enable changing only a few controlled properties in a quantifiable manner. Lanthanide scandates ($LnScO_3$, Ln = lanthanide element) such as the $GdScO_3$ support in Figure 1.1 meet these criteria. The lanthanides earn their title of "rare earths" not by being scarce[**46, 47**] but by being chemically similar: most lanthanides are stable in an Ln^{3+} oxidation state, with similar ionic bonding, minimal or absent redox activity, and other chemical properties.[**48**]. These similarities make lanthanide behavior so similar as to complicate the process of separating them from the ore deposits in which they are found.[**48, 49**] As such, we might expect the lanthanide scandates to be a family of materials that reduces the number of confounding variables when comparing them as catalytic supports.

$LnScO_3$ are orthorhombic ABO_3 perovskites with the *Pbnm* structure[**50**] shown in Figure 1.2(a). The structure in Figure 1.2(a) is viewed along the [110] axis, as $LnscO_3$

may alternately be described as pseudocubic with respect to the $< 110 >$ and $< 001 >$ directions of the orthorhombic unit cell.[**50, 51, 52**] (The pseudocubic reference frame will be indicated as $(hkl)_{pc}$ herein.) As the lanthanide in the A-site cation position is varied across the series, the $LnScO_3$ lattice parameter decreases as shown in Figure 1.2(b).[**53, 54**] Bulk and thin film lanthanide scandates have many potential applications. For example, they find use in metal-oxide-semiconductor field effect transistor technology owing to their large optical bandgaps and stability in contact with silicon.[**55**]

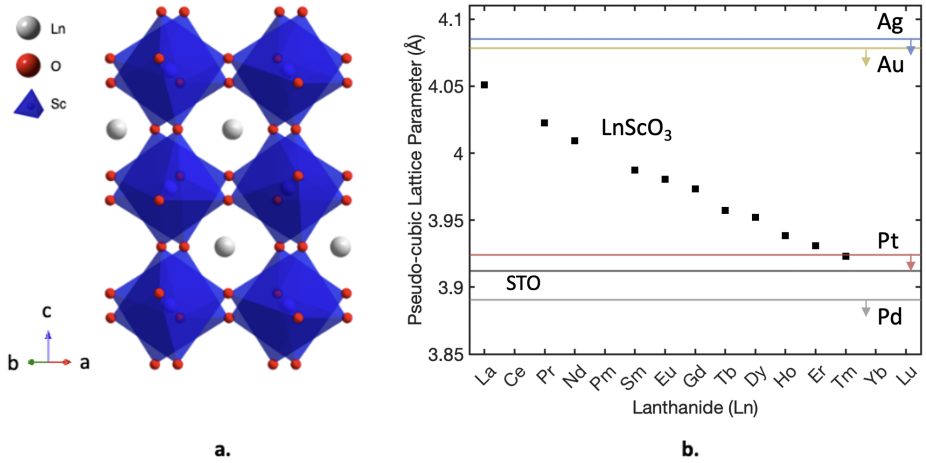

Figure 1.2. (a) The *Pbnm* distorted-perovskite structure of lanthanide scandates, viewed along [110]. (b) Pseudocubic lattice parameters of $LnScO_3$ across the for all lanthanides across the series (except Ce and Pm).[**56**] Horizontal lines represent the lattice parameters of $SrTiO_3$ (STO) and bulk noble metals typically used as catalysts; nanoparticle lattice parameters are generally contracted as compared to the bulk,[**57**] as indicated for the noble metals by a downward arrow. Figure adapted from Reference [**56**].

This work focuses on lanthanide scandate nanoparticles, whose interesting surface properties[**58, 59**] and potential for morphological control[**60**] make them particularly well suited to fundamental studies of catalyst-support interactions. Each lanthanide scandate also has a lattice parameter which is well-matched to that of various noble metal

catalysts, represented by the horizontal lines in Figure 1.2(b). Interestingly, while STO nanoparticles have been demonstrated to exhibit cube-on-cube epitaxy with deposited Pt nanoparticles,[**16**] the pseudocubic lattice parameters of $LnScO_3$ are all greater than that of bulk Pt. As such, a series of $LnScO_3$-supported Pt catalysts should all induce in the Pt tensile strain of varying degrees.

$LnScO_3$ can meet the need for a series of structurally similar supports. Each $LnScO_3$ has a different lattice parameter while maintaining the same bulk *Pbnm* structure.[**50, 51, 52**] The $LnScO_3$ nanoparticles also share similar electronic structures and surface terminations.[**58, 61**] These similarities minimize the number of confounding variables that could affect catalytic behavior, enabling us to attribute variations in catalysis to properties such as lattice parameter and surface basicity,[**59**] whose changes we can then predict as a function of lanthanide ion.

1.2. Organization

This dissertation aims to elucidate trends across the lanthanide series and utilize them for the synthesis and catalytic applications of lanthanide scandate nanoparticles. Chapter 2 provides details of the experimental and computational methods used to prepare and characterize the lanthanide scandate catalysts that are discussed throughout this work. Chapter 3 introduces the "one-line hydrosauna" method of synthesizing lanthanide scandates and describes various attempts to understand the role of water vapor in the hydrosauna technique, including in-situ methods. Chapter 4 then details the so-called "two-line" hydrosauna approach, a synthetic method for precise water vapor control that is guided by DFT-calculated thermodynamic trends for enhanced $LnScO_3$ phase purity

and morphological control. The synthesis method presented in Chapter 4 is used to generate the material for the catalytic studies covered in later chapters.

After discussion of the lanthanide scandate synthetic method, this thesis focuses on characterizing the $LnScO_3$ material in the context of catalytic behavior after the deposition of noble metal catalyst particles on the $LnScO_3$ supports. Chapters 5 and 6 explore the surface adsorbate binding behavior of $LnScO_3$-supported gold (Au) and platinum (Pt) respectively, with particular focus on the contribution of Ln 4f electrons to metal-support interactions in heterogeneous catalysis. Chapter 7 looks to the metal/oxide interface, using carbon monoxide binding to probe how the various $LnScO_3$ induce strain in the metals they support, and how that strain contributes to catalytic behavior. Finally, future directions for this work including the application of $LnScO_3$ supports to other probe molecules and chemical reactions are discussed in Chapter 8.

CHAPTER 2

Experimental and Computational Methods

This chapter provides a more detailed description of the most significant experimental and computational methods that recur throughout this thesis.

2.1. X-Ray Diffraction

The first step in characterizing many crystalline materials is X-ray diffraction (XRD), which reveals the structural fingerprint of a material. Powder XRD, or PXRD, is particularly useful for nanoparticles, as it can identify the crystalline phases produced as well as quickly estimate the average particle size. In an XRD experiment, X-rays are scattered by atomic planes in a crystalline lattice structure, with maximum constructive interference occurring at incidence angles that obey Bragg's law:

$$2d_{hkl}sin\theta = n\lambda$$

where d_{hkl} is the interplanar spacing between adjacent (hkl) planes, θ is the angle of incidence relative to the sample, n is a positive integer, and λ is the wavelength of X-rays provided by the source.

This work utilized a Bragg-Brentano geometry, in which both the X-ray source and the detector are moved simultaneously to generate a diffraction pattern of intensity vs angle that is unique to the sample; the angles of maximum diffraction are determined by the particular interplanar spacings of the material phase being studied. From this pattern,

one can resolve the relative amounts of each crystalline phase present by conducting a fit to calculated patterns. Rietveld refinement, a technique which calculates a PXRD pattern by adjusting simulated structural and instrument parameters to minimize the least squares difference between calculated and experimental patterns, also enables the determination of things such as unit cell dimensions and phase fractions.[**62**] A Scherrer analysis relates the width of a diffraction peak and the shape and size of a crystallite to estimate the average crystallite size.[**63**] Important to note is that this strategy only accounts for the crystalline components of a powder sample; while the relative crystallinity of samples can be gauged from their PXRD patterns, alternative methods are required to learn more about any amorphous material that may be present in a sample.

Crystalline phase identification in this dissertation was done in the J. B. Cohen X-Ray Facility at Northwestern University via PXRD on a Rigaku Ultima diffractometer using a Cu (λ = 1.54 Å) source and the Bragg-Brentano geometry with a Kβ nickel filter. The diffractometer was operated at 40 kV and 35 A. To maintain high peak intensity, no monochromatization was done; the Kβ lines do not appear at the diffraction peak intensities observed in these experiments. Peak identification and phase fraction calculations were done using whole pattern fitting with JADE software.[**64**]

2.2. Transmission Electron Microscopy

Transmission electron microscopy (TEM) is a powerful tool for characterization of nanoscale materials and is used throughout this work to obtain high-resolution real-space images and diffraction information of $LnScO_3$ nanoparticles and metal/$LnScO_3$ catalyst

samples. There are several types of signal that can be collected in an electron microscope, each based upon the interactions between an electron beam and the sample.

In conventional TEM, a parallel electron beam passes through an extremely thin (generally <100 nm for good high-resolution imaging) sample.[**11**] The transmitted electrons form a projected image of the sample on an electron detector. Conventional TEM is used in this dissertation to observe real-space images of $LnScO_3$ and Pt nanoparticles that have been deposited on $LnScO_3$ particle substrates. The microscopes used for conventional TEM in this dissertation include a JEOL 2100F TEM and JEOL ARM200CF probe-corrected S/TEM, both operated at 200 kV and both available in Northwestern's Electron Probe Instrumentation Center (EPIC).

Scanning transmission electron microscopy (STEM), on the other hand, rasters a focused (rather than parallel) beam across the sample to obtain an image pixel-by-pixel. This process is similar to scanning electron microscopy (SEM), but STEM uses both a higher voltage and smaller probe size than SEM, enabling better resolution. Secondary electron (SE) STEM imagining is used in this work to obtain real space shape and faceting information. SE images result from secondary electrons which, under the electron beam, are ejected from the conduction or valence band of a material, meaning they leave the sample with low energies and therefore have a small mean escape path (on the order of 1 nm).[**11, 65**] That means SE imagining is particularly sensitive to the area within a few nanometers of a sample surface; SE-STEM imaging is thus used in this dissertation to observe nanoparticle topology and morphology.

Another STEM technique, annular dark field (ADF) imaging, is used in this work to obtain real space $LnScO_3$ shape and size while simultaneously observing the presence of

other phases, e.g. un-reacted precursor materials or amorphous phases. ADF works by collecting only scattered electrons via an annular detector around the beam. At very high angles, electrons are incoherently scattered due to electrostatic interactions between the nucleus and the electron beam, meaning thicker regions of the sample or elements with higher atomic number (Z) can often (though not always) be expected to appear brighter in a high-angle annular dark field (HAADF) image. To interpret an image this way, care must be taken that the collection angles are high enough to avoid significant contributions from diffraction contrast owing to orientation changes and grains, strain, or other effects, rather than "Z-contrast."[**66**] Both SE and ADF STEM images shown in this work were collected at Northwestern's BioCryo Facility using a Hitachi HD2300 STEM operated at 200 kV.

Lastly, high resolution electron microscopy (HREM) was used to characterize the $LnScO_3$ surfaces and Pt/$LnScO_3$ interfaces more closely. HREM is a conventional TEM technique that makes an image primarily with phase contrast from interference with diffracted electron beams at the image plane. While phase contrast is often present in TEM imaging, in HREM it is the dominant source of contrast, so this technique can be used effectively to image atomic structure. Because contrast is generated by interference, an HREM image is not a direct image of the atomic planes in a sample. This makes interpretation of HREM images quite complicated, so analysis of these images uses image simulations such as multislice simulation,[**67**] conducted by Z. Mansley, where possible. HREM was done either at EPIC on the JEOL ARM200CF or at Argonne National Lab using the Argonne Chromatic Aberration-Corrected TEM (ACAT), which is an FEI Titan

80-300 with a combined chromatic and spherical aberration corrector. These microscopes were also operated at 200 kV.

In all electron microscopy methods, sample preparation and cleaning are an essential part in obtaining meaningful images and diffraction patterns with the greatest possible resolution. All samples were prepared by drop casting after sonicating powders for 10 min in 200 proof ethanol. The sample synthesis and preparation processes often introduce hydrocarbons and other adsorbates to the surfaces of TEM samples. Under the electron beam, these contaminants polymerize and condense around the sample, greatly obscuring it. Samples must be cleaned in a manner that removes these unwanted adsorbates without damaging the sample itself or altering its original structure. In this work, $LnScO_3$ and Pt/$LnScO_3$ samples were cleaned for 2 min in O_2-Ar plasma using an SPF SBT Plasma Cleaner. Au/$LnScO_3$ samples were cleaned with an ozone cleaner instead, as small Au nanoparticles were more prone to sintering during plasma cleaning than Pt.

Important to note is one major limit of electron microscopy: the area of sample that can be analyzed is very small, on the order of nanometers to microns across at any given time. Therefore, care is taken in this work to ensure that all S/TEM data is truly representative of the entire sample. This is done by a combination of redundancy (i.e. depositing the same sample on multiple TEM grids and characterizing multiple samples that were produced using the same method) and corroboration with XRD and other characterization techniques.

2.3. Atomic-Layer Deposition

Atomic layer deposition (ALD) is a vapor-phase technique originally developed by Suntola and Hyvarinen for the synthesis of thin film materials.[**68**] This technique utilizes self-limiting reactions between a substrate and a series of gaseous precursors to deposit material layer by layer. Synthesis by ALD is conducted in cycles of half-reactions. First, one gaseous precursor flows over the substrate surface, depositing a layer that converts the functionality of the surface. Next, after purging that reactant from the system, a second reactant is flowed over the substrate to complete the overall reaction. Reactants are designed to be self-limiting, i.e. each reactant will react at the sites generated by the previous gas but not its own sites. In principle, one cycle generates one layer of the desired compound. In practice, the initial stages of metal deposition by ALD generally result in the formation of discrete islands,[**69**] and thus in the low-cycle limit this technique can controllably deposit metal nanoparticles.[**70**]

In this work, one ALD cycle was used to deposit platinum nanoparticles on $LnScO_3$ substrates with an Arradiance GEMStar deposition system in Northwestern's GIANTFab facility. At 200 °C, thirty-three pulses of trimethyl(methylcyclopentadienyl)platinum(IV) ($MeCpPtMe_3$) at 3 s each were used as the platinum source with each pulse followed by a 40 s stagnant delay (i.e. no carrier flow). The ligands were oxidized and removed by twenty ozone pulses of 5 s each, with a 60 s delay after each pulse. Nitrogen purging between precursor exposures was done at 50 sccm.

2.4. Density Functional Theory

The behavior of electrons and atoms is described quantum mechanically by the Schrödinger equation $\hat{H}\Psi = E\Psi$ which relates the energy E of a system described by wave function Ψ to the Hamiltonian, $\hat{H}$. The Hamiltonian operator defines the total energy of the wave function including kinetic and potential energy but also electron-electron and electron-nucleus interactions. While this equation can be solved exactly for certain simple cases, analytical solutions quickly become untenable in real solids with many atoms and many electronic interactions.

The Hohenberg-Kohn theorems[**71**] and Kohn-Sham equations[**72**] proposed ways to think about many-electron problems. Hohenberg, Kohn, and Sham theorized that the ground state energy of a system can be uniquely determined by finding the electron density that minimizes the total energy (i.e. the ground state energy is a functional of the electron density). Using electron density as a fundamental variable greatly simplifies the many-body problem put forth by the Schrödinger equation or other theories (e.g. Hartree-Fock) which deal directly with wave functions: the wave function-based solution for a system with N electrons has 3N variables, while the electron density is always a function of only three spatial variables.

This important shift to density-based solutions is one of the foundations of density functional theory (DFT), a quantum mechanical model for calculating the behavior of electrons in a solid. The total energy of the system can be calculated as a function of the electron density, with terms accounting for the external potential, the kinetic energy, and an exchange-correlation energy arising from the Coulombic and spin interactions between electrons.

Throughout this work, DFT is applied to both hydrosauna synthesis optimization and characterization of electronic structures of various $LnScO_3$. All calculations were done with WIEN2k, an all-electron augmented plane wave + local orbitals package.[**73**] The code partitions a unit cell into atomic spheres, defined by local orbitals inside specified muffin-tin radii, and interstitial regions defined by a plane wave expansion.

This body of work uses the PBEsol functional[**74**] in an on-site hybrid approach, which applies an exact exchange hybrid correction on correlated electrons within the muffin tins which would otherwise be poorly described by conventional functionals.[**75**] Hybrid fractions of 0.38 and 0.50 were used for the Ln 4f and Ln 5d orbitals, respectively, shown by Mizzi et al. to describe $LnScO_3$ accurately[**61**] and confirmed via force minimization to describe the lanthanide oxides, hydroxides, and oxyhydroxides as well. In all cases, the plane-wave expansion parameter RKMAX was 7.2 for calculations of $LnScO_3$, and muffin-tin radii of 2.02, 1.50, and 1.82 Bohr were used for Ln, O, and Sc, respectively. A ferromagnetic model was used in calculations of $LnScO_3$; as the Néel temperatures for the lanthanide scandates are generally below 5 K,[**54**] the difference between ferromagnetic and antiferromagnetic ordering is negligible.

CHAPTER 3

Introduction to Hydrosauna Synthesis

3.1. Introduction

For use as a structurally similar series of catalytic supports in accordance with the goals of this work, lanthanide scandates ($LnScO_3$) must be synthesized at relatively low temperatures—to minimize particle sintering—using a method that generates consistently phase pure material, with consistent morphology, for multiple lanthanides. Various $LnScO_3$ have been synthesized in the past by others as thin films by atomic layer deposition (ALD)[**76**] or pulsed laser deposition,[**77**] and as powders through solid-state reactions, though these generally require high temperatures and/or pressures.[**50**]

Hydrothermal synthesis is a well-studied synthetic method to produce nanomaterials because the greater pressure allows liquid-state diffusion at relatively low temperatures. In work by a prior student $GdScO_3$ and other $LnScO_3$ were hydrothermally synthesized at temperatures as low as 300 °C from a mixed-cation gel precursor.[**60, 78**] This method forms reasonably well-faceted particles, though fine control of the resulting particles' size or morphology can be very difficult. Most crucially for this work, a hydrothermal approach results in too high an activity of water, which favors formation of ScOOH, LnOOH, and $Ln(OH)_3$, rather than the desired perovskite $LnScO_3$ phase as will be discussed below. It has been hypothesized that this phenomenon is caused by too high a concentration of water vapor in the synthesis environment.[**60**] For instance, considering the reaction:

$$2LnScO_3 + 4H_2O \longleftrightarrow LnOOH + ScOOH + Ln(OH)_3 + Sc(OH)_3$$

excess water vapor will drive this reaction to the right, suggesting that the water vapor partial pressure must play an important role in the synthesis outcome.

As suggested by Paull et al., one way to address this challenge is a switch from a hydrothermal approach to a so-called hydrosauna approach.[**60**] In the hydrosauna method, the same mixed-cation gel precursor, approximated as $\mathrm{LnSc(OH)_6} \cdot x\mathrm{H_2O}$ ($x \approx 6$), is calcined in a humid environment, nominally to maintain openness of the gel precursor matrix; dry heating was argued to result in the matrix's collapse, generating an amorphous product. This humid environment may be provided by the gel itself in an autoclave, as in the traditional hydrothermal approach, or it may be provided externally in an open-flow system as in the hydrosauna method, such that the water activity remains constant and relatively low throughout most of the synthesis, rather than increasing as the gel itself dries out.[**60**] As will be shown, there are more details to the process.

In this chapter, I first provide an overview of the lanthanide scandate precursor gel formation and the hydrosauna technique in Section 3.2. Then, Section 3.3 includes some results from hydrosauna syntheses, demonstrating a range of possible phase purity and morphology and investigating the contribution of water vapor to back-reactions and the formation of undesired hydroxide phases. In-situ techniques are explored in Section 3.4 as a means of understanding more about the structure of the precursor gel and its crystallization process. These experiments presented many difficulties but introduced some further insights into the operation of the hydrosauna technique, which will be discussed in this section as well, and explored in greater detail in Chapter 4.

The synthesis work in this chapter benefitted from discussion with Dr. Ryan Paull, who developed the original hydrosauna technique for lanthanide scandates, as well as Professor Laurence D. Marks and Professor Kenneth R. Poeppelmeier. The in-situ Raman experiments were done with guidance from Dr. Selim Alayoglu.

3.2. One-Line Hydrosauna Method

The synthesis of $LnScO_3$ in this chapter was done via modifications of the water vapor-assisted sol-gel hydrosauna reaction first described by Paull et al.[**60**] First, an equimolar solution of lanthanide and scandium ions was prepared by dissolving 4 mmol of Ln_2O_3 (Ln = La, Nd, Sm, Gd) and Sc_2O_3 in 20 mL of 15.8 N nitric acid stirred at 90 °C. After the liquid evaporated, this nitrate precursor was dissolved in 20 mL of deionized water and then added dropwise to 50 mL of 10 M NaOH in an ice bath to precipitate a mixed-cation hydroxide gel, the precursor for $LnScO_3$ growth. The gel was isolated via centrifuge at 4500 rpm for seven minutes and washed three times with deionized water before being transferred to the furnace, which is shown schematically in Figure 3.1. To generate a humid environment, argon gas was flowed through a water bubbler upstream of the furnace, introducing a partial pressure of water vapor estimated to be the saturation pressure of water in argon gas (about 17.9 torr).[**60**] Many mechanisms have been discussed for the contribution of water in water-assisted nanoparticle syntheses, including water as a sintering agent,[**79**] a catalyst,[**80**] and a means for maintaining of the openness of the gel matrix[**78**] among others.[**81**] The role of water vapor in this synthesis will be discussed in more detail in Ch. 4, which outlines studies done to determine water

vapor effects and shows how controlling water vapor concentration is required to improve phase purity and consistency.

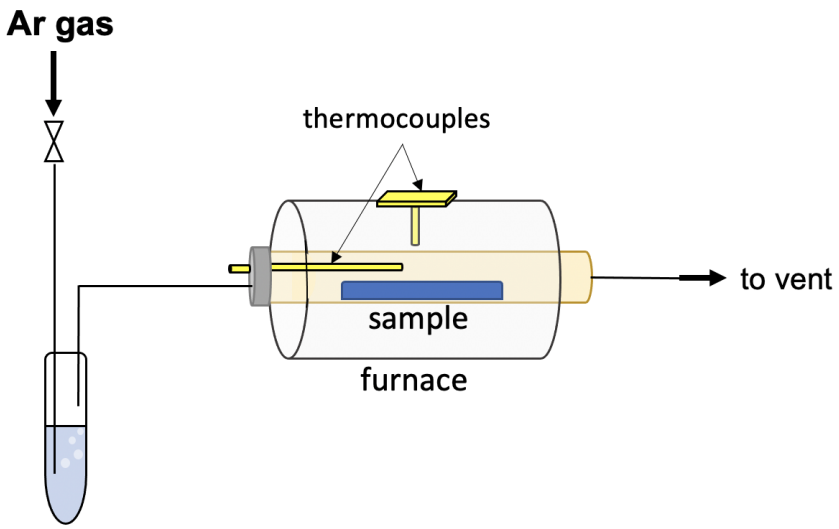

Figure 3.1. Schematic of the one-line hydrosauna tube furnace reactor. A bubbler is used to generate a humid environment with a partial pressure of water vapor near the saturation pressure of water in argon at room temperature (17.9 torr).

After preparation, the gel was calcined in the furnace using a two-step treatment: a high-temperature step at 450 °C for two days, and then a low-temperature step at 300 °C for one day.[**60**] This treatment utilizes our knowledge of the kinetic growth regimes of hydrothermally synthesized particles.[**82**] The products of each synthetic step are shown in Figure 3.2. After the high-temperature step in Figure 3.2(a), there has been nucleation of many small $LaScO_3$ particles, while after both the high-temperature and low-temperature steps, we observe a greater population of larger, more faceted $LaScO_3$ particles. The higher temperature is required to nucleate the perovskite phase, and the lower temperature step enables particle growth and surface smoothing and faceting. The final product was rinsed

with deionized water and centrifuged several times, and then put into a drying oven at 80 °C overnight.

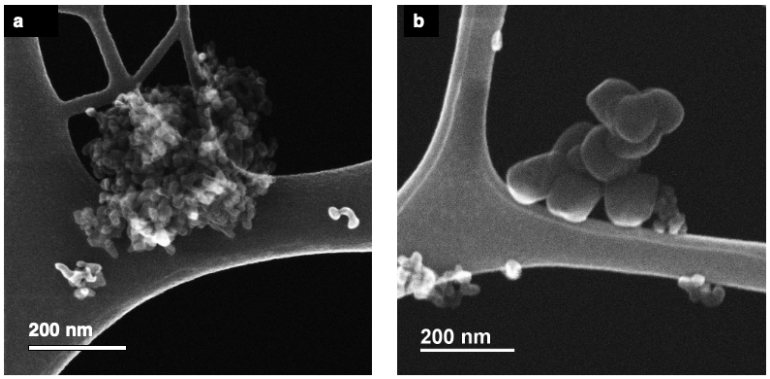

Figure 3.2. Secondary electron STEM images of $LaScO_3$ produced by hydrosauna synthesis for (a) 450°C for 48 hours, and (b) 450°C for 48 hours, then 300°C for 24 hours.

This one-line hydrosauna method generally produces faceted particles with an average width of 120 nm, shown in Figure 3.3. Lanthanide scandate particles for Ln = La, Nd, Sm, and Gd have been prepared in this manner, generating beveled nanocuboids terminated with majority $\{100\}_{pc}$ and $\{110\}_{pc}$ faces.[**60**]

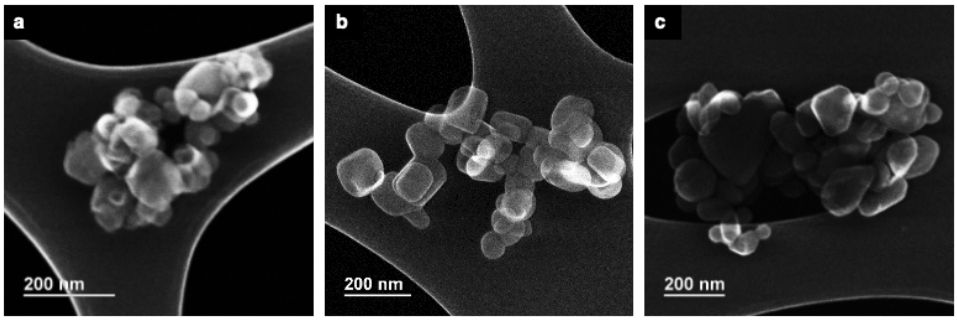

Figure 3.3. SE STEM images of (a) $LaScO_3$, (b) $NdScO_3$, and (c) $SmScO_3$ prepared with the one-line hydrosauna method.

In interpreting SE images of lanthanide scandates, note that the morphology of these $LnScO_3$ is not simply cuboidal; rather, the particles themselves often take on an orthorhombic shape with a long axis. Thus, particles that appear cuboidal in (S)TEM are simply viewed as a two-dimensional projection along this long axis. Also note the range in topographic contrast of the SE images, particularly in Figure 3.3(c); charging of $LnScO_3$ significantly reduces the SE signal, except in areas where carbon can locally compensate charge. Thus particles imaged over carbon show large topographical contrast as expected from an SE STEM image, while those over holes in the carbon give less signal.

As with many nanoparticle syntheses, while the one-line hydrosauna method effectively produces various well-faceted lanthanide scandate nanoparticles, there still exists much room for improvement in precise control of the products. Between batches of nominally equal syntheses, for example, one can observe a wide distribution of particle morphology, as shown for several relatively high-purity $NdScO_3$ syntheses in Figure 3.4. There must also be parameters to adjust in order to improve phase purity and consistency; as represented in Figure 3.5, repeated $NdScO_3$ syntheses generate a few other phases, mostly NdOOH and $Nd(OH)_3$, with notable discrepancies even between two boats of precursor material calcined in the same furnace at the same time. (These boats are centered about the thermocouple, with one being "upstream" of the other, or closer to the gas inlet feed. In Figure 3.5, diffraction patterns from upstream boats appear in blue, and downstream in red.) Peak identification and phase fraction calculations were done using whole pattern fitting with JADE software.[**64**]

The observed variety in both morphology and phase purity is attributed to environmental changes,[**60**] particularly small but critical changes in water vapor partial pressure

that were beyond the detection and control capabilities of the experimental set-up. The next sections of this chapter detail experimental techniques that were utilized to enhance our understanding of the steps that occur in a hydrosauna synthesis of $LnScO_3$ from a precursor gel, and whether water vapor may have an important role to play in the process.

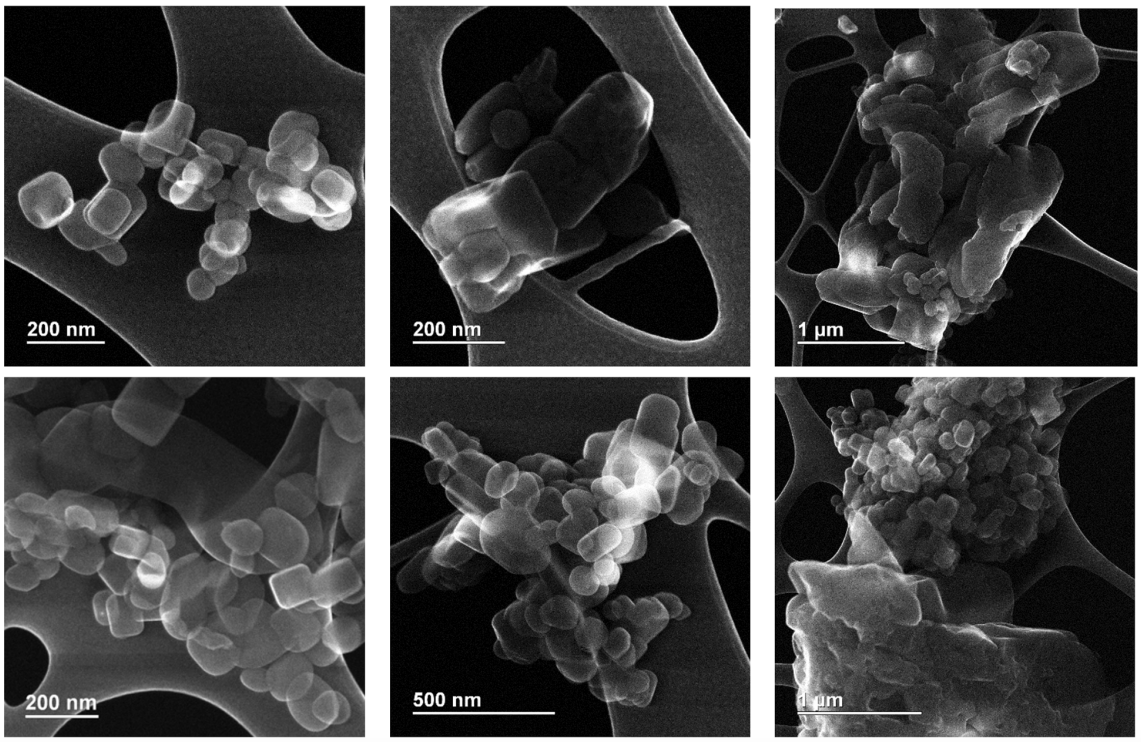

Figure 3.4. SE STEM images of $NdScO_3$ nanoparticles from six different synthesis batches, each prepared using a nominally identical one-line hydrosauna procedure.

3.3. Back-Reactions: Effects of Water Vapor on Product Phases

The presence of $Ln(OH)_3$, LnOOH, $Sc(OH)_3$, and ScOOH in the products of the one-line hydrosauna synthesis, as well as in hydrothermal or autoclave syntheses, indicates that water vapor has an important role to play. One goal of this work is to understand how this hypothesis could be confirmed and then leveraged to control synthetic outcomes.

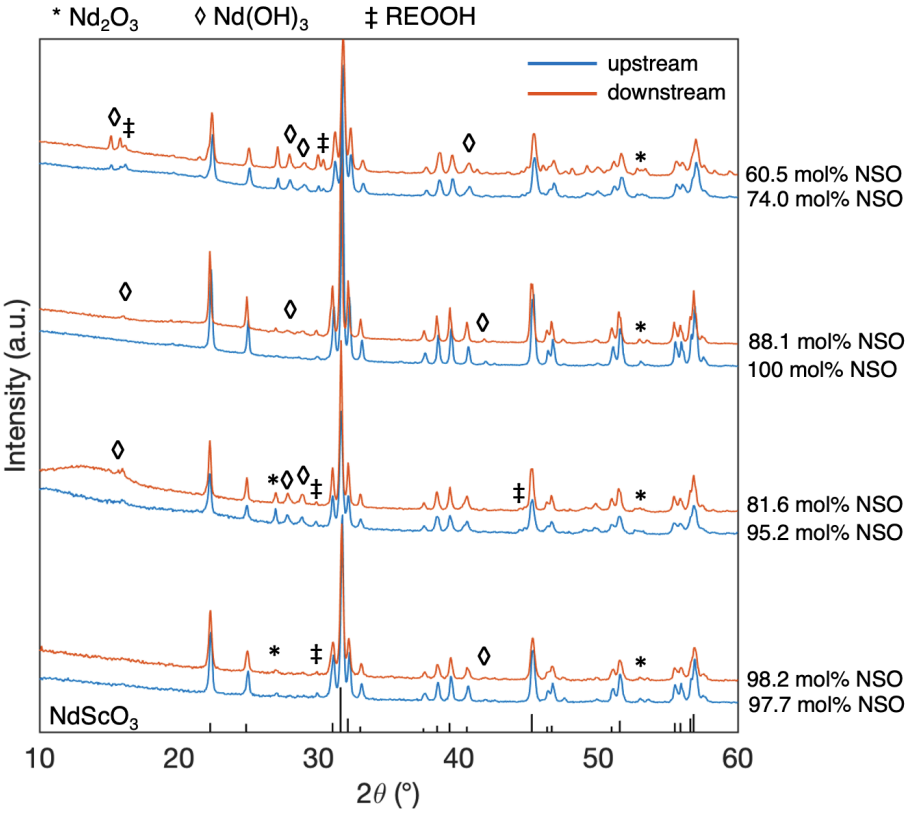

Figure 3.5. PXRD patterns of four different $NdScO_3$ batches, each prepared using the same one-line hydrosauna technique. For each batch, the upstream (blue) and downstream (red) patterns are shown, with the mol% of $NdScO_3$ displayed on the right. The calculated pattern for $NdScO_3$ from Ref. [**83**] is shown in black at the bottom of the plot. Undesired phases are indicated by symbols: * for hexagonal Nd_2O_3, ◊ for $Nd(OH)_3$, and ‡ for REOOH (RE = Nd or Sc).

There are several indicators that the flow of water vapor affects synthetic outcomes. One of these can be observed by dividing a single precursor gel batch into two alumina boats to be fed into the tube furnace such that one is "upstream" of the other, as previously described. Gel produced in each batch, when subjected to the same flow rate of saturated argon gas and thermal treatment as the others, should yield similar results. However, Figure 3.5 illustrates a discrepancy between the $NdScO_3$ phase purity of single batches: in

many cases, there is stark contrast between the results of the upstream and downstream boats. It is therefore likely that certain inconsistencies outside of the control of this experimental set-up are responsible, at least in part, for some of these incongruous results. For example, note that in many cases the downstream sample is more likely to contain a higher fraction of hydroxide- and oxyhydroxide-containing phases than the upstream sample; as the gel dehydrates, one might expect the downstream boat to experience a locally increased partial pressure of water vapor if there is an excess of water vapor in the system.

In addition, while the precursor gel contains an average of 75% water by volume, there is some variation in this value between batches and even within a batch. In each centrifuge tube of cleaned precursor, the gel will be denser at the bottom. If one boat contains a higher fraction of this denser gel, then early in the heating process as the gel is dehydrating, the local environment of that boat will be more humid. (Indeed, the water provided by the gel itself is proven to influence the hydrosauna products in Chapter 4.) One can distribute the gel as evenly as possible to lessen this effect, but a more quantifiable depiction of the role of water vapor in the reaction may be understood from the later stages of the synthesis. Above about 300 °C, when the gel has lost most of its water, the majority of water in the system is delivered by the saturated carrier gas. Thus, we can more clearly observe the effects of differing carrier gas humidity at these late stages.

Back-reactions upon cooling provide another important indication of the effects of water vapor in the hydrosauna synthesis. The impacts of these reactions were determined via a series of quenched synthesis experiments; after the completion of the lower-temperature

(300 °C) synthesis step, two different cooling and quenching methods were used. The PXRD patterns of the products resulting from these syntheses are shown in Figure 3.6. First, the control sample was allowed to cool naturally in the furnace, with no change in the flow rate of carrier gas through the upstream bubbler until the samples reached room temperature and were removed from the furnace. This sample shows the greatest fraction of $Nd(OH)_3$. In another case, an analogous synthesis was completed, but while the sample cooled naturally in the furnace, gas flow was stopped. Reducing the input of "fresh" water vapor leaves the samples to cool in stagnant furnace conditions. Lastly, an analogous synthesis was completed, except that the sample was removed from the furnace while still hot (300 °C), enabling the powder to be quenched in air on the lab bench. Each of these experiments was repeated three times to ensure that the trends in hydroxide formation were a result of quenching method, rather than natural variation in synthesis conditions.

The quenching studies depicted in Figure 3.6 illustrate how an excess of water vapor during furnace cooling leads to an increased fraction of lanthanide hydroxide and oxyhydroxide compounds in the product. A typical one-line hydrosauna synthesis, as described in Section 3.2, flows Ar through a water bubbler throughout the entire process of heating, holding at temperature, and cooldown. This process was the control in the quenching studies, and has a significant probability of producing undesired $Ln(OH)_3$ or LnOOH, as illustrated by the diffraction patterns in both Figure 3.5 and Figure 3.6 (blue curve). One way to decrease the fraction of undesired hydroxide-containing phases is simply to reduce the water vapor concentration in the system on cooling. In an environment of reduced water vapor partial pressure, any un-reacted material has a greater probability of forming

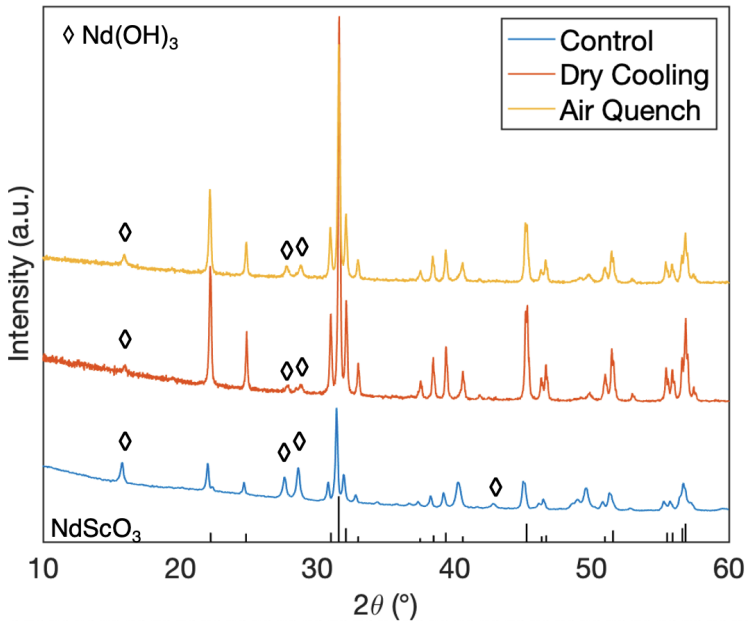

Figure 3.6. PXRD patterns of the products of three $NdScO_3$ one-line hydrosauna syntheses. The control (blue) is a synthesis in which the furnace is ramped to 450 °C, held for 48 hours, and then cooled to room temperature, with a water bubbler providing consistent water vapor throughout heating, calcining, and cooling to room temperature. The dry cooling synthesis (red) follows the same thermal profile but turns off the flow of gas through the bubbler as soon as the 48 hours of heating are up, such that the sample cools without any further addition of water vapor to the system. The air quenched synthesis (yellow) again follows the same thermal profile, except that after the 48 hours of heating, while the sample is still at temperature, the bubbler is turned off and the powder is removed from the furnace to cool in air on the lab bench. The pattern for $NdScO_3$ from B. Veličkov et al. [**83**] is shown in black at the bottom of the plot and the ◊ symbol indicates peaks from the $Nd(OH)_3$ structure.

the desired $LnScO_3$ phase instead of back-reacting to thermodynamically stable $Ln(OH)_3$. This phenomenon is illustrated by the enhanced $NdScO_3$ phase purity in the yellow and red diffraction patterns in Figure 3.6. The greatest improvement to phase purity was

obtained via dry cooling in the furnace, indicating that the water vapor concentration, rather than a faster cooling rate, is responsible for this change.

Worth noting, however, is that the PXRD technique can only convey quantitative information about crystalline material. Any amorphous material, such as amorphous scandia, is not contained in the molar fractions of $NdScO_3$ that have been calculated from PXRD. Furthermore, the precursor gel itself appears amorphous when observed with XRD. "Turning off" the water vapor in the hydrosauna system during cooling may be an effective method for reducing the molar fraction of LnOOH and $Ln(OH)_3$ in the products by eliminating back-reactions on cooling, but it still does not enable us to obtain phase pure $LnScO_3$; we cannot yet describe the role of water vapor throughout the majority of the synthesis process.

3.4. In-Situ Hydrosauna Techniques

Thus far, we have described the potential impacts of water vapor partial pressure in both the early stage of synthesis, as the gel is first heating and dehydrating, and the last stage of synthesis, as the final products are cooling down. The natural next step is to design experiments that allow us to observe what happens in between. A wealth of information could be gained from experiments that resolve the gel structure or phases present as a function of time throughout the synthesis. For example, hydroxide and oxyhydroxide phases are observed in the final products; do these crystallize early on, as required intermediates for the $LnScO_3$ formation, or are they produced solely during back-reactions? There are often complexities in interpreting data obtained with in-situ

techniques, and as we will see, the hydrosauna synthesis of $LnScO_3$ from their precursor gels provide a particular challenge.

One method of directly observing the progression of crystalline phases throughout a reaction is in-situ XRD. Time-resolved XRD studies have been conducted at synchrotron and lab X-ray sources since the 1990's[**84**] to monitor phase transitions during syntheses and other process,[**85, 86, 87**] and even to observe the formation of precursor and intermediate compounds during crystallization from a sol-gel.[**88**] In-situ XRD is therefore of particular value in studying the crystallization of $LnScO_3$ during hydrosauna synthesis, as evidence suggests that formation of lanthanide oxyhydroxides may be a required step in subsequent crystallization of lanthanide scandates.[**60**] A similar phenomenon has been observed in the hydrothermal synthesis of rare-earth manganates ($REMnO_3$, RE = rare earth).[**89**] While the back-reaction quenching studies of the previous section did not yield LnOOH as frequently as $Ln(OH)_3$, one must consider the possibility of re-hydration upon cooling, as well as the possibility that the LnOOH stability varies with the chosen lanthanide. These hypotheses could be proven or disproven with the observation of crystalline phases present at various stages of the hydrosauna synthesis of $LnScO_3$ that in-situ XRD could provide.

The $LnScO_3$ precursor gel's large water content complicates our ability to study $LnScO_3$ crystallization with in-situ XRD. The gel contains about 75% water by volume on average. As the material calcines, it undergoes a significant shape change that introduces major difficulties in monitoring this hydrosauna synthesis by in-situ XRD. These complications are discussed, and results presented, in Appendix A.

3.4.1. In-Situ Raman Spectroscopy

While PXRD is useful for identifying crystalline phases present throughout a synthesis, Raman spectroscopy can also provide vital characterization of the gel structure. Raman scattering is a complementary tool to XRD that is particularly useful during the early stages of gel crystallization, as the technique is highly sensitive to local structure, including bond lengths and stretching modes, as well as bonding environment. In addition to monitoring X-ray amorphous phases[**90**] or hydrogen and hydroxide binding[**43**] in-situ in a calcining hydrogel, the high sensitivity of Raman scattering also enables its use to investigate the subtle differences in the orthorhombic distortion of the lanthanide scandates' *Pbnm* structures that result from changing the A-site cation.[**91**]

To replicate the hydrosauna conditions in an in-situ Raman experiment, a 50 mL/min flow of N_2 gas was passed through a bubbler upstream of the sample once again. Some $NdScO_3$ precursor gel was placed in a furnace with a sample holder whose position could be moved manually throughout the experiment to maintain the sample's position under the beam as the precursor gel dried, thus potentially overcoming one challenge of in-situ XRD for this system. The sample was heated to 750 °C using a variable transformer, with voltage calibrated to approximate a 5 °C/min ramp rate. This higher temperature (750 °C rather than the 450 °C used in the established hydrosauna procedure from Section 3.2) was selected to ensure crystallization of $NdScO_3$ within a reasonable time while the system was being tested.

Prior to in-situ heating, Raman spectra were collected for Sc_2O_3, Ln_2O_3, and $LnScO_3$ to elucidate the Raman signatures that may be expected in the final product. Two different sources were used: $\lambda = 488$ nm (17.5 mW), encompassing the Raman shift range

of the oxides, and $\lambda = 244$ nm (5.1 mW), encompassing the Raman shift range of peaks associated with the hydroxide bonding expected in the gel. For the case of Ln = Nd, these test spectra are shown in Figure 3.7. The $NdScO_3$ Raman spectra (blue) are consistent with that of single-crystal $NdScO_3$, with Raman-active A_g modes at 302, 380, 433, and 492 cm^{-1}, and B_{2g} modes around 340 and 434 cm^{-1}.[**92**] Here, the modes designated A_g and B_g represent vibrational modes that are symmetric or asymmetric with respect to the principal axis of symmetry, respectively.

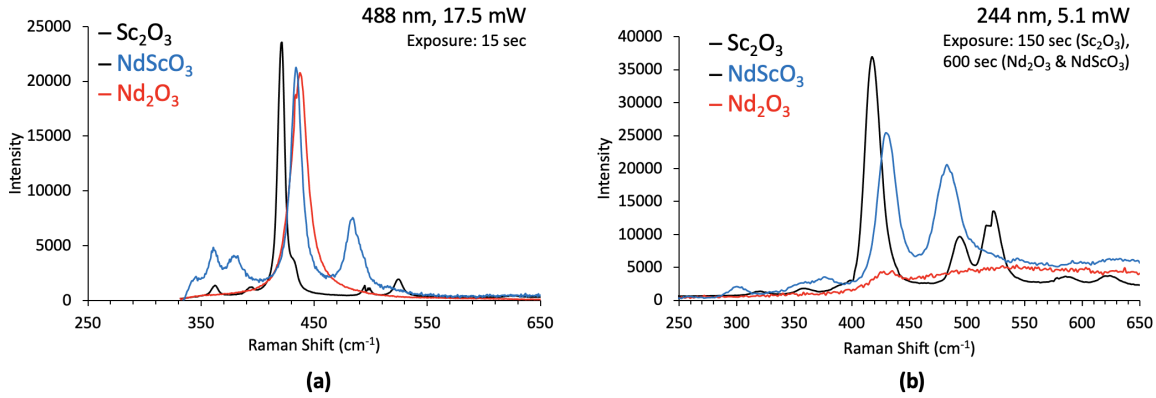

Figure 3.7. Raman spectra of $NdScO_3$ powder and the two binary oxide powders from which it is made, Nd_2O_3 and Sc_2O_3. Spectra were collected using two different sources: (a) $\lambda = 488$ nm (17.5 mW), encompassing the range of peaks associated with the various oxides, and (b) $\lambda = 244$ nm (5.1 mW), encompassing the range associated with hydroxide bonding during earlier stages of hydrosauna synthesis. Combined, these spectra reveal expected Raman-active A_g modes at 302, 380, 433, and 492 cm^{-1}, and B_{2g} modes around 340 and 434 cm^{-1}.[**92**]

This experimental set-up was conducive to collecting localized spectra, monitoring progression of the synthesis at different positions in the sample. Taking advantage of this functionality, we can observe that the crystallization of $LnScO_3$ did not occur homogenously; Figure 3.8 illustrates the experimental set-up and shows $\lambda = 488$ nm Raman

spectra taken from different points on the sample taken at 750°C, after about 5 hours at temperature. Each region is marked with a unique symbol. In the thickest region of the sample near the center, marked with the yellow triangle in Figure 3.8(c), no lanthanide scandate nor oxide peaks of any kind are resolved in the corresponding Raman spectrum in Figure 3.8(d). In a slightly thinner area, marked by the blue star in Figure 3.8(c), there are distinct peaks at 427 and 470 cm^{-1}, which are not signatures of $NdScO_3$ nor any of the starting binary oxides. However, they could be $NdScO_3$ peaks that have shifted towards smaller wavelength; bond distances may expand with longer exposure to the high temperatures used in this experiment. The thinnest region of the sample, indicated by the red diamond and the slightly paler color in Figure 3.8(c), is closest to an edge where the most drying has occurred, and displays the prominent $NdScO_3$ Raman peaks in the 350 – 500 cm^{-1} region of the corresponding spectrum in Figure 3.8(a).

Such drastically different results over the span of a 5 mm pellet of sample point to yet another difficulty with in-situ hydrosauna synthesis from a precursor gel. Quite apart from the water vapor provided by a bubbler, the water in the gel itself seems to have a large impact on the local environment. The main challenge of in-situ Raman spectroscopy for this system is essentially opposite to that of in-situ XRD: while the footprint of a typical lab-source X-ray beam is too wide to deliver strong signal from the shrinking calcined gel, the footprint of the Raman source is too narrow to provide an accurate depiction of the entire synthesis process on average.

Despite not enabling a highly detailed look at the evolution of the gel structure as it crystallizes to $LnScO_3$, $Ln(OH)_3$, or LnOOH, this difficulty offers an important insight into the hydrosauna synthesis. The water vapor delivered by the gel itself in thicker

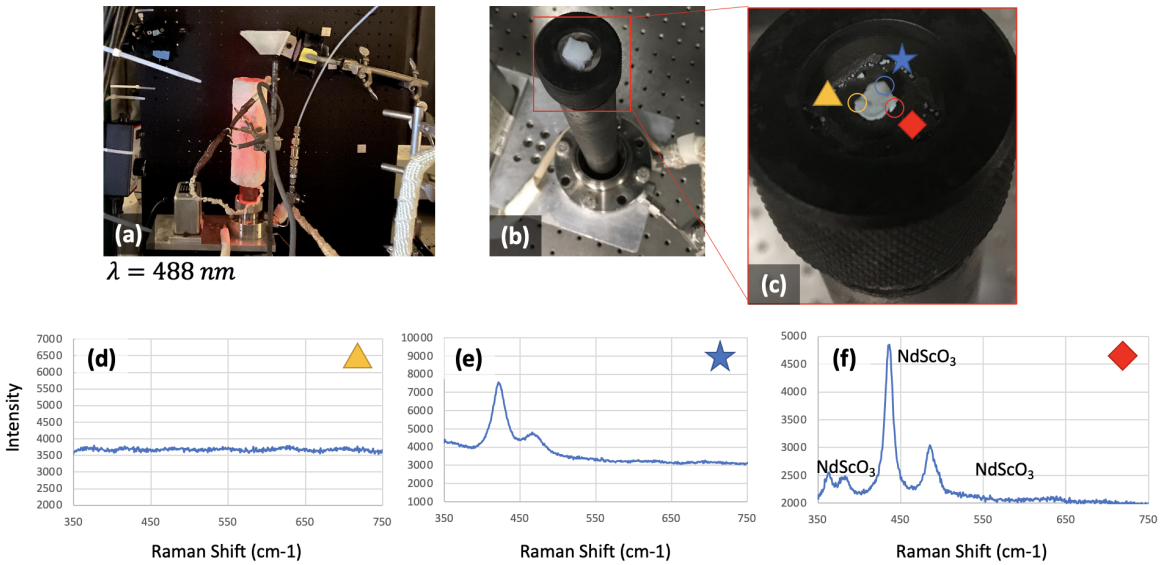

Figure 3.8. (a) Photograph of Raman spectroscopy experimental set-up. (b) The $NdScO_3$ precursor gel sitting in the Raman sample holder. The boxed region is magnified in (c), which shows the three spots at which a Raman spectrum was collected after calcining the gel for 2 hours at 750°C. The corresponding Raman spectra are shown in (d) – (f).

regions of sample may inhibit $LnScO_3$ crystallization. In multiple iterations of this Raman experiment, areas of sample with a higher surface area to volume ratio, or those which will experience faster rates of drying at the beginning of the synthesis, generate more phase pure $LnScO_3$. Thus, to enable consistent high-purity $LnScO_3$ hydrosauna synthesis, one must precisely control the water vapor in the environment, calibrating for the water provided by the gel itself and maintaining a very low water vapor partial pressure. Any in-situ hydrosauna experimental design must therefore account for sample shape to maintain both sample position and appropriate humidity conditions.

3.5. Conclusions

This chapter demonstrates the functionality of hydrosauna synthesis in forming faceted lanthanide scandate nanoparticles at relatively low temperatures. However, consistency in phase-purity and morphology have room for improvement via synthetic parameters and methods. In particular, the presence of back-reactions and dependence on gel geometry and gas flow rate indicate that water vapor partial pressure is one of the most important parameters to control precisely.

In-situ techniques can be a valuable tool in characterizing the hydrosauna synthesis further, especially in terms of monitoring the hydrogel precursor's structure and the presence of hydroxides and oxyhydroxides as intermediate phases. However, because the hydrogel is 75% water by volume and must be calcined in a very particular humid environment, it provides a challenge in this arena. Future attempts to study hydrosauna $LnScO_3$ synthesis with in-situ techniques must consider both how to keep the final product in the line of the beam, and how to control the sample shape, packing density, and gas flow rate to mimic hydrosauna conditions despite necessarily using a smaller volume of precursor gel. Chapter 8 will offer some exploration of these factors and discussion of how to work around them, including the introduction of other techniques beyond X-ray diffraction and Raman scattering. Meanwhile, in the next chapter computational studies on the thermodynamics of lanthanide hydroxide formation are combined with ex-situ experiments as an alternative way of understanding the role of water vapor in hydrosauna synthesis of lanthanide scandates.

CHAPTER 4

Quantifying the Role of Water Vapor in Lanthanide Scandate Hydrosauna Synthesis

4.1. Introduction

In a previous chapter, it was explained why hydrosauna synthesis is preferred over more traditional hydrothermal methods for lanthanide scandates, but the water vapor partial pressure (P_{H_2O}) was not yet adequately controlled, nor its role elucidated. While hydrothermal synthesis is often an effective and accessible route to producing oxide nanoparticles,[**93, 94**] synthetic conditions impact the product in ways that are difficult to quantify.[**36, 94, 95**] The variable compositions and environmental sensitivities of a material's precursors complicate our ability to predict what occurs inside an autoclave or other reactor. Predicting synthetic conditions such as humidity therefore requires an understanding of the thermodynamic stability of potential undesired phases, as well as the target phase. In the past this has been done by formulating thermodynamic metrics for compound "formability" under various conditions, for example a thermodynamically derived maximum driving force[**96**] or an activity coefficient model for non-ideal solutions under hydrothermal conditions.[**97**] More recently, machine learning has been used to predict perovskite synthesis with training data sets based on experimentally observed perovskite syntheses[**98**] and even on the synthetic conditions used in unsuccessful syntheses.[**99**]

The lanthanide scandates ($LnScO_3$) provide a particular challenge in the realm of predictive materials synthesis. While $LnScO_3$ nanoparticles may find uses in a wide array of applications owing to their large optical band gap,[**53**] potential for morphological control,[**60**] and catalytically useful surface properties[**59**] (see Chapter 1), the thermodynamics of lanthanide perovskite formation was previously not completely understood.[**89, 100**]

Chapter 3 highlighted several factors that complicate a purely experimental understanding of $LnScO_3$ formation in the hydrosauna environment. First, given its sensitivity to water content, the hydrogel precursor is not amenable to common in-situ X-ray techniques (see Appendix A). Sample holders frequently used for in-situ XRD experiments such as capillary tubes alter the gel's water exposure and drying rate by increasing the gel packing density and the area exposed to flowing gas. Furthermore, assumptions that hold for in-situ studies of other perovskite materials or even hydrothermally synthesized $Ln(OH)_3$ may not hold for the $LnScO_3$ material system in a hydrosauna environment,[**89, 100, 101**] as the phase diagrams of the Ln_2O_3-H_2O system are known to vary greatly for various Ln.[**100, 102**] Lastly, while it is common to extrapolate or assume linear trends across the lanthanide series because of linear or near linear trends in Ln^{3+} cation radius and Ln-O bond length,[**103, 104**] evidence suggests that Ln^{3+} electronic structure[**105**] and resulting properties such as Lewis acidity,[**59, 106**] do not trend linearly (or monotonically) with increasing Ln atomic number. This is not surprising, as occupation energies for 4f shells are known not to be linear. It is therefore difficult to determine experimentally how the thermodynamics of the Ln_2O_3-H_2O system will impact $LnScO_3$ formation and how that impact can be exploited in designing its synthesis.

We have thus far hypothesized that the presence of hydroxide and oxyhydroxide phases after $LnScO_3$ synthesis was due to an uncontrolled and often relatively high concentration of water vapor in the synthesis environment. Here, this hypothesis is proved rigorously using both experiment and density functional theory (DFT), and consistent high-purity $LnScO_3$ synthesis is achieved for five different lanthanides (Ln = La, Pr, Nd, Sm, and Gd). We approach the synthesis with a hydro-sauna method that uses an open environment with a lower humidity than hydrothermal or other hydrosauna approaches.[**60**] Because slight changes in the chemical potential of water can result in a wide range of $LnScO_3$ phase purity, and because—as this chapter will demonstrate—the optimal chemical potential of water varies for each Ln, this modification to the typical hydrosauna method is required.

DFT modeling of the thermodynamics of the Ln_2O_3-H_2O material system is used to guide the choice of water vapor partial pressure in the $LnScO_3$ hydro-sauna synthesis. Our understanding of the thermodynamics of $LnScO_3$ formation coupled with a modified hydrosauna synthesis method enables us to generate nearly phase pure $LnScO_3$ for multiple lanthanides.

The two-line modification to the hydrosauna reactor described in Section 4.3 was designed and built with help from Dr. Robert Kennedy and Dr. Fenghua Ding. The DFT calculations and analysis in Section 4.4 benefitted greatly from discussion with Professor Laurence D. Marks. Other analysis in this chapter was the result of much discussion with Professor Laurence D. Marks and Professor Kenneth R. Poeppelmeier, and appears in Reference [**107**].

4.2. Observing Environmental Effects on Hydrosauna Synthesis

Without control of the partial pressure of water in the flowing carrier gas, the hydro-sauna process can yield a variety of results, generating powders with 60 - 99 wt% (55 – 98 mol%) $LnScO_3$ (see Section 3.2). We attributed this range in product yield to humidity changes caused by unintentionally varied bubbler temperature or flow rates. This chapter discusses both experimental and theoretical approaches to determining the role of water vapor partial pressure in the synthesis of each $LnScO_3$.

To observe the effects of water vapor directly, experiments were designed to take advantage of the water in the gel itself. The gel's water can evaporate during calcination to provide differing levels of humidity depending on the exact water content. First, a $GdSc(OH)_6 \cdot xH_2O$ ($x \approx 6$) mixed-cation precursor gel was prepared according to the procedure described in Section 3.2. Then, instead of calcining the as-prepared wet gel using the previously defined method, in what I will henceforth refer to as a "standard" hydro-sauna synthesis, the gel was first dried in air at room temperature for three days. This dried gel was then calcined in the established one-line hydro-sauna method. PXRD and STEM results of this experiment are shown in Figure 4.1.

The inability to resolve sharp diffraction peaks in Figure 4.1(a) shows that the precursor gel is X-ray amorphous (i.e. has small grains, roughly less than 1 nm), and largely remains so after drying out at room temperature. Even so, nucleation of the perovskite $GdScO_3$ phase can still be identified after calcination in the hydro-sauna condition in the yellow pattern in Figure 4.1(a), though the SE and corresponding ADF STEM images in Figure 4.1(b-g) indicate the resulting particles were very small, typically below 10 nm

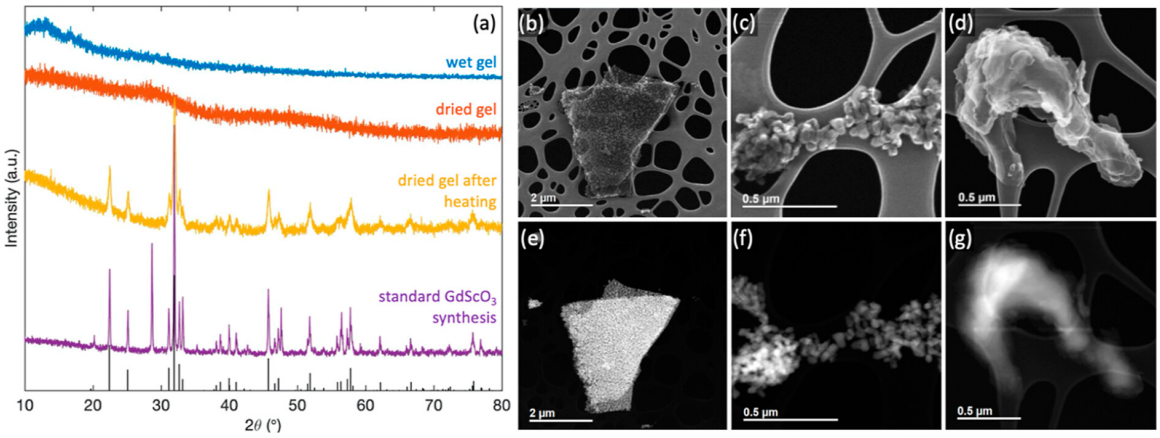

Figure 4.1. (a) PXRD patterns for the mixed-cation $GdSc(OH)_6 \cdot xH_2O$ ($x \approx 6$) gel precursor (blue) as produced, (red) after drying in air at room temperature for three days, and (yellow) after calcining the air-dried gel in the one-line hydro-sauna reactor according to the established two-step procedure, compared to (purple) $GdScO_3$ resulting from a standard hydro-sauna synthesis directly from the wet gel. Patterns are presented on a linear scale and shifted vertically for clarity. The calculated pattern for pure $GdScO_3$, obtained from the crystal structure determined by B. Veličkov et al.,[**83**] is shown in black at the bottom. Broad peaks are indicative of amorphous material or small nanoscale grains. (b-d) SE STEM and (e-g) corresponding ADF STEM images of randomly selected powder resulting from this hydro-sauna synthesis of the pre-dried gel.

wide on average. These small particles also do not have a well-faceted nanocuboid morphology, as seen in Figures 4.1(d) and 4.1(g). By comparing the PXRD pattern of the calcined dried gel to that of a standard $GdScO_3$ synthesis (i.e. calcined from wet gel) in Figure 4.1(a) it can also be seen from the narrower, sharper crystalline peaks that the crystallite size was increased significantly by calcining the wet gel. Notably, all hydroxide and oxyhydroxide phases are absent from the dried-gel PXRD pattern in Figure 4.1(a), I will argue because of the lack of excess water vapor, but these undesired phases are present in the standard one-line hydrosauna synthesis pattern.

In a successful $LnScO_3$ synthesis, the chemical potential of water must be large enough to allow particle growth, while remaining relatively low to minimize formation of hydroxide and oxyhydroxide phases. This phenomenon can be observed clearly for $NdScO_3$ in Figure 4.2, which establishes an upper and lower limit to the P_{H_2O} required for achieving crystalline, well-faceted $NdScO_3$ nanoparticles. A high P_{H_2O} yields the undesired hydroxide and oxyhydroxide phases, while a low P_{H_2O} yields very small crystallites, leading to peak broadening and a nearly X-ray amorphous pattern. Modifications to the hydrosauna reactor must therefore be made to control the water vapor pressure precisely within these limits.

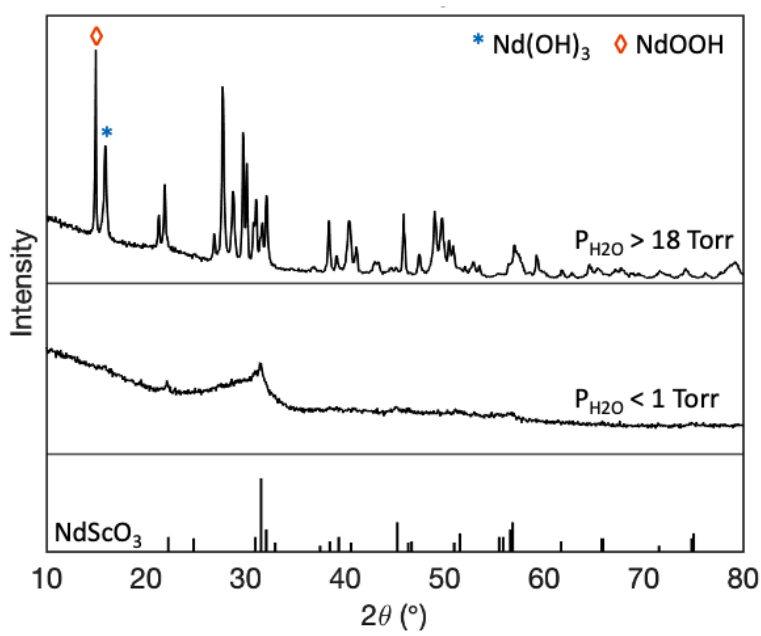

Figure 4.2. PXRD patterns of powder resulting from two $NdScO_3$ syntheses. The top pattern shows the presence of $Nd(OH)_3$ and NdOOH in the case where water vapor partial pressure (P_{H_2O} is too high. The middle pattern shows an X-ray amorphous material in the case where P_{H_2O} is too low. Patterns are presented on a linear scale and are shifted vertically for clarity. The calculated pattern for $NdScO_3$ is shown at the bottom, obtained from the crystal structure of B. Veličkov et al.[**83**]

4.3. Two-Line Hydrosauna Synthesis

Water vapor partial pressure must be controlled precisely to attain highly phase pure $LnScO_3$. In addition, the optimal water chemical potential for each of the two synthetic stages may be different, as will be discussed later. To control these factors, a "two-line" reactor with variable water chemical potential was used as shown in Figure 4.3.

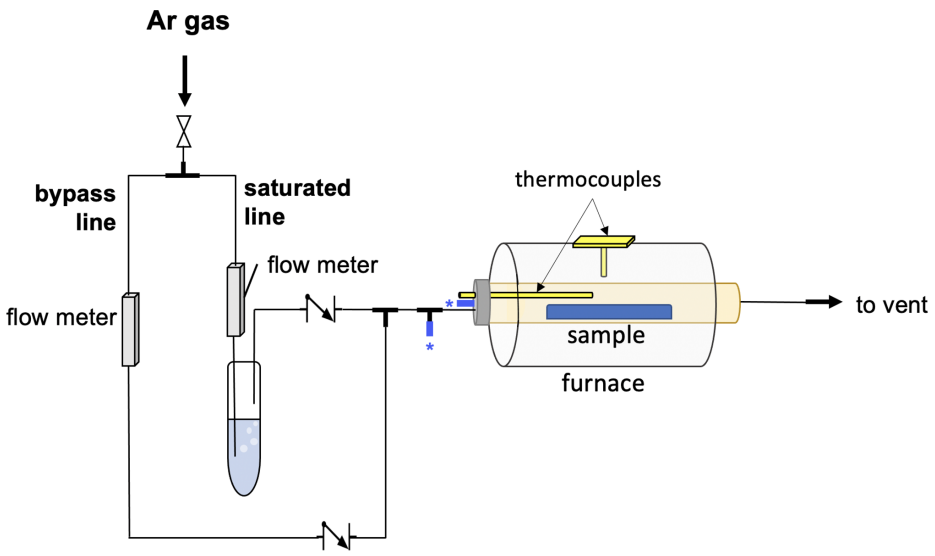

Figure 4.3. Schematic of the hydrosauna tube furnace reactor including the two-line mechanism for controlling water vapor partial pressure. The bypass line provides dry argon gas, while the saturated line passes the gas through a bubbler filled with deionized water. Blue inlet lines marked with an asterisk (*) indicate locations at which a hygrometer was placed to monitor humidity.

Variable-area flow meters allowed for precise monitoring of argon gas flow rates through two lines: a saturated line passing through the water bubbler, and a bypass line that remains dry. Adjusting the flow rates through each line allows for control of P_{H_2O} in the inlet gas stream, ranging from 0.1 torr to 17.9 torr; the latter is the saturation pressure of water in argon gas at lab temperature (23 °C). These values were confirmed by direct

measurement of the relative humidity with a hygrometer placed upstream of the furnace and use of the equation:

$$Relative\ humidity = \frac{P_{H_2O}}{P_{vap}} \times 100\%$$

where P_{vap} is the vapor pressure of water and P_{H_2O} is the partial pressure of water vapor.

Importantly, introducing two lines to the hydrosauna reactor allows for water vapor partial pressures below the saturation pressure of water in a carrier gas. The absence of hydroxide and oxyhydroxide phases in the pre-dried gel in Figure 4.1 indicates that these phases are the result of an excess of water vapor. Meanwhile, the lower limit in Figure 4.2 indicates that some water vapor is required for nucleation of $NdScO_3$ nanoparticles; evaporation of water from the gel alone does not provide sufficient humidity for the duration of the synthesis. Evidence supporting this is shown in Figure 4.4, which compares PXRD patterns of $NdScO_3$ made via one-line hydrosauna synthesis (black curve) and two-line hydrosauna synthesis (red curve). The one-line reaction must be conducted near the saturation pressure of water vapor in the carrier gas (here argon) at lab temperature, 17.9 torr. The two-line reaction in this case utilized the bypass line to generate a P_{H_2O} of 10 torr. Nearly halving P_{H_2O} eliminated almost all $Nd(OH)_3$ formation while maintaining sharp $NdScO_3$ peaks.

4.4. Determining Optimal Water-Vapor Partial Pressures with DFT

We have thus far explored the role of P_{H_2O} in hydrosauna synthesis experimentally and developed a new reactor to control for this parameter. However, this information was insufficient to produce highly phase pure $LnScO_3$ for multiple lanthanides; the optimal

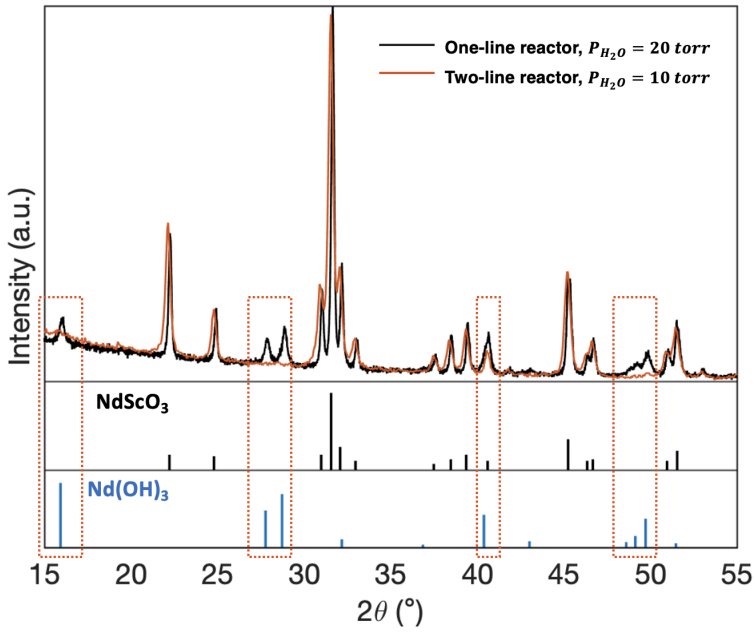

Figure 4.4. PXRD patterns of (black) $NdScO_3$ synthesized in a one-line hydrosauna reactor for which $P_{H_2O} = 10$ torr and (red) $NdScO_3$ synthesized in a two-line hydrosauna reactor for which $P_{H_2O} = 20$ torr. Marks at the bottom indicate the calculated patterns of $NdScO_3$ (black) and $Nd(OH)_3$ (blue), from Velickov et al.[**83**] and Uecker et al.[**53**] respectively. Dashed red boxes highlight differences between the two patterns.

chemical potential of water is different for each Ln and would be difficult to determine by experiment alone. For example, the $P_{H_2O} = 10$ torr environment utilized in Figure 4.4 works well for $NdScO_3$ synthesis, but does not yield phase-pure $LaScO_3$ or $GdScO_3$.

The value of the optimal P_{H_2O} depends on the thermodynamics of the formation of $LnScO_3$, $Ln(OH)_3$, and LnOOH from the starting materials, Sc_2O_3 and Ln_2O_3. Since not all lanthanides readily form the LnOOH phase, and properties such as Lewis acidity are not linear across the lanthanide series for Ln^{3+} or $LnScO_3$,[**59, 106**] we cannot assume linearity with increasing Ln atomic number in these thermodynamics.

A modeling approach provides one path to determining the trend. The formation energies of the involved hydroxide, oxyhydroxide, and oxide phases can be calculated with DFT, giving some indication as to the water affinity of each lanthanide. This knowledge then informs which $LnScO_3$ syntheses require lower P_{H_2O}, and by how much, to maximize $LnScO_3$ production and minimize production of hydroxide and oxyhydroxide phases. However, this route also has problems to overcome, namely the handling of the 4f electrons in $LnScO_3$. Previous studies have treated 4f systems using generalized gradient approximation and a Hubbard + U method.[**54**] DFT + U methods place 4f states far below the valence band maximum, where they are wrongly treated as core-like states.[**61**] Experimental studies of the valence band structure of $LnScO_3$ by X-ray photoelectron spectroscopy (XPS) show that Ln 4f electrons in these materials are valence active, and should not be treated as core states.[**61, 105, 108, 109, 110**]

XPS and other photoelectron spectroscopy techniques probe primarily the occupied density of states,[**111**] with results for the valence region yielding spectra such as those in Figure 4.5.[**108, 109, 110, 112**] This technique is well-suited to accurate measurements of electronic structure even in correlated electron systems because, at the incident X-ray energies typically used for XPS (1253.6 – 9251.7 eV),[**113**] Ln 4f photoionization cross sections are notably higher than the cross sections of other states contributing to the valence band,[**114**] namely Sc 3d and O 2p states.[**105, 54**] For instance, at 1253.6 eV the cross-section for O 2p is 0.005 whereas that for Gd 4f is 0.038.[**114**] Thus differences between XPS valence spectra of various $LnScO_3$ reflect Ln 4f contributions.

From the XPS valence spectra we see that Ln4f states reside close to or in some cases at the valence band maximum,[**105**] and therefore should not be treated as core-like states

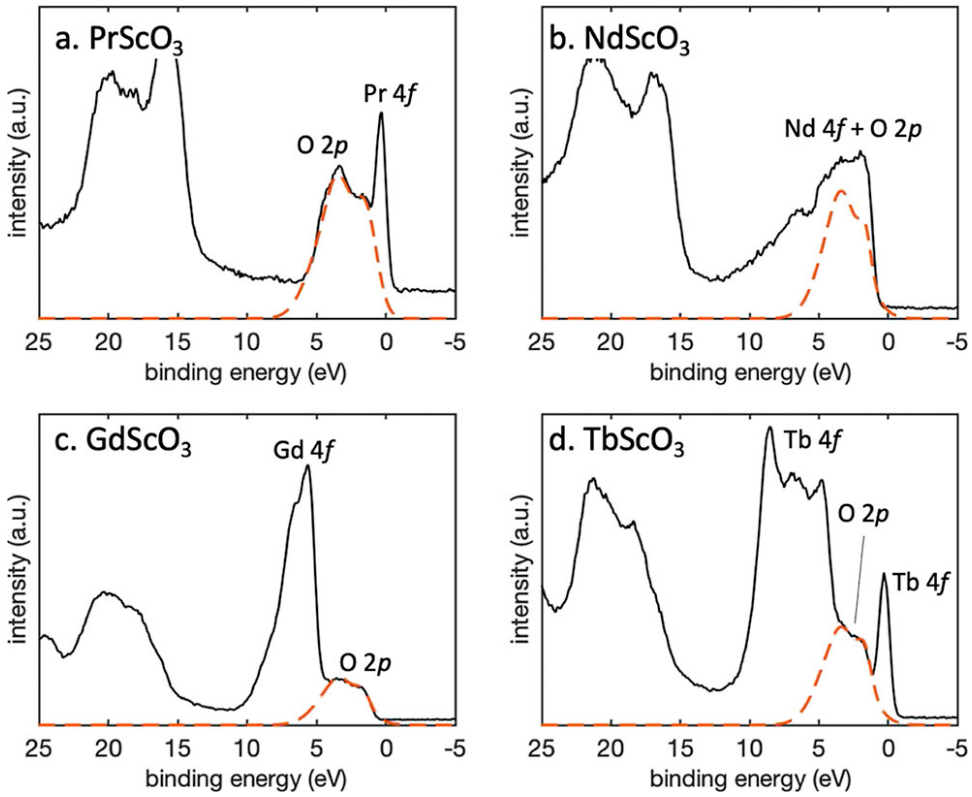

Figure 4.5. This figure reproduces (with some scale changes) data from Haasch et al.[**105, 108, 109, 110, 112**] XPS valence spectra of four $LnScO_3$ (110) bulk crystals aer shown: (a) $PrScO_3$, (b) $NdScO_3$, (c) $GdScO_3$, and (d) $TbScO_3$. As a guide to the eye, the approximate magnitude of the O 2p contribution is marked by the dashed orange lines. O 2p states maintain approximately the same magnitude and position for each $LnScO_3$, while the Ln4f peak magnitude and position vary. The X-ray source was monochromatic Al Kα radiation with an energy of 1486.6 eV; note that at this energy, Ln 4f photoionization cross sections are notably greater than other valence band contributors.[**114**] The features from 15 – 25 eV correspond to the Ln 5p doublet and O 2s peaks, which also remain relatively constant for each $LnScO_3$.

as in DFT + U methods.[**61**] For example, in the experimental XPS valence spectrum for GdScO shown in Figure 4.5(c), there is a clear distinction between O2p states near the valence band edge, where the binding energy is at or just above 0 eV, and the Gd 4f states which are farther down but still present at the bottom of the valence band. The magnitude

and position of O 2p peaks in $LnScO_3$ remain approximately constant regardless of the lanthanide, as represented by the dashed red lines in Figure 4.5. In contrast, the Ln 4f peak resides much closer to the valence band edge in $NdScO_3$ or $PrScO_3$, and $TbScO_3$ has seven states far from and one near the valence band edge. Herein we accurately handle the Ln 4f states by avoiding DFT + U methods and instead using an on-site hybrid DFT approach,[**75**] which is described further in the next section and has previously shown very good agreement between experimental XPS valence spectra and simulated spectra for several $LnScO_3$.[**61**]

4.4.1. Computational Methods: Representing $LnScO_3$ with DFT

DFT calculations were done with WIEN2k, an all-electron augmented plane wave + local orbitals package.[**73**] The PBEsol functional[**74**] was used in an on-site hybrid approach[**75**] as detailed in Section 2.4. Muffin-tin radii of 2.02, 1.2, and 0.5 Bohr were used for Ln, O, and H atoms, respectively, in the cases of LnOOH and $Ln(OH)_3$. In calculations of Ln_2O_3 and $LnScO_3$, a muffin-tin radius of 1.82 Bohr was used for Sc atoms, and the radius of O atoms was increased to 1.5 Bohr to accommodate the absence of short O-H bonds. The plane-wave expansion parameter RKMAX was 7.2 for all oxides and 3.0 for all hydroxides and oxyhydroxides.

4.4.2. Thermodynamic Trends for Optimal $LnScO_3$ Hydrosauna Synthesis

To establish the thermodynamic trends that will guide our choice of P_{H_2O} for $LnScO_3$ syntheses, DFT was used to calculate the formation enthalpy of each relevant compound

identified during $LnScO_3$ hydrosauna synthesis. First, the formation enthalpy of LnOOH from the starting lanthanide sesquioxide Ln_2O_3 was calculated according to Eq. 4.1:

$$\frac{1}{2}Ln_2O_3 + \frac{1}{2}H_2O \rightarrow LnOOH \tag{4.1}$$

for multiple Ln across the lanthanide series. These results are shown in Figure 4.6(a). Next, formation enthalpies of Ln(OH)3 were calculated from both Ln2O3 (Eq. 4.2), and LnOOH (Eq. 4.3) as a function of lanthanide across the series.

$$\frac{1}{2}Ln_2O_3 + \frac{3}{2}H_2O \rightarrow Ln(OH)_3 \tag{4.2}$$

$$LnOOH + H_2O \rightarrow Ln(OH)_3 \tag{4.3}$$

This trend can inform our hydrosauna synthesis conditions. For those lanthanides with a stronger tendency to form $Ln(OH)_3$, the optimal P_{H_2O} for $LnScO_3$ formation will be lower by a factor proportional to the difference in $Ln(OH)_3$ formation energy. Therefore, experimentally determining the optimal P_{H_2O} for one lanthanide scandate enables nearly phase pure synthesis of the rest by following the trends calculated with DFT. The P_{H_2O} used for the formation of all five lanthanide scandates are shown in Figure 4.6(b). By adjusting P_{H_2O} accordingly across the lanthanide series, we generate nearly phase pure $LnScO_3$ nanoparticles for all five lanthanides tested, as can be seen in the PXRD patterns

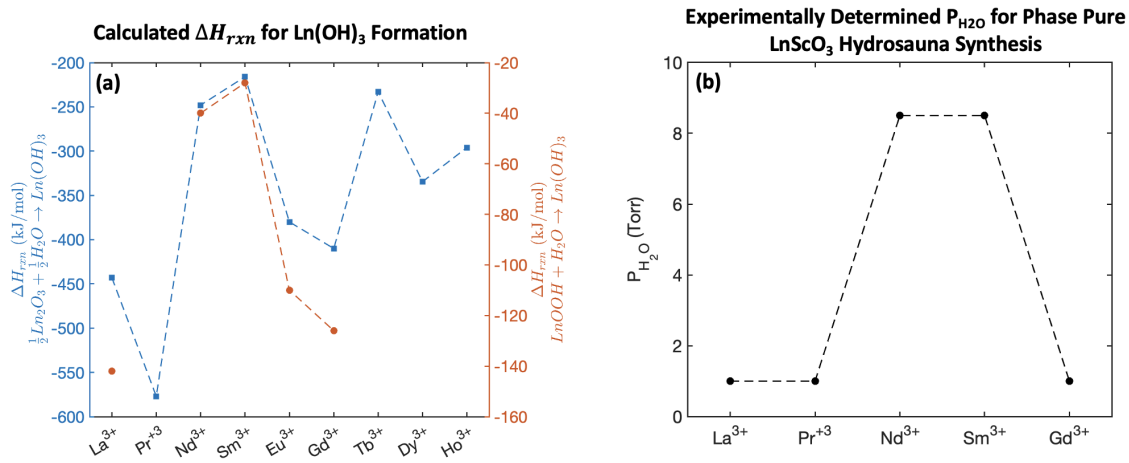

Figure 4.6. DFT-calculated energy trends for various lanthanides in the reactions $\frac{1}{2}Ln_2O_3 + \frac{3}{2}H_2O \rightarrow Ln(OH)_3$ (blue square, left axis) and $LnOOH + H_2O \rightarrow Ln(OH)_3$ (red circle, right axis). Data points which are not shown (e.g. Tb, Dy, Ho) are those for which no experimental LnOOH structure was found. (b) P_{H_2O} used to synthesize high purity $LnScO_3$ in the two-line hydrosauna reactor. Dashed lines serve only as a guide to the eye.

in Figure 4.7(a). The morphology of the resulting $LnScO_3$ nanoparticles is shown in Figures 4.7(b-e) for Ln = La, Nd, Sm, and Gd. Contrary to those in Figure 4.1, $LnScO_3$ nanoparticles made under optimized conditions are well faceted and fairly uniform in shape and size.

The values of P_{H_2O} used to generate the results in Figure 4.7 are only subtly different, yet they are experimentally confirmed optimum values. This phenomenon is demonstrated more explicitly in Figure 4.8. Conducting a hydro-sauna synthesis of $NdScO_3$ with the P_{H_2O} that is optimal for $LaScO_3$ (1.0 torr) instead of the predicted 8.5 torr in Figure 4.6(b) results in smaller crystallite sizes or X-ray amorphous material, shown by comparing Figures 4.8(a) and 4.8(b). Calcining $LaScO_3$ in the P_{H_2O} that is optimal for $NdScO_3$ (8.5 torr) instead of the predicted 1.0 torr results in significant $Ln(OH)_3$ formation—shown

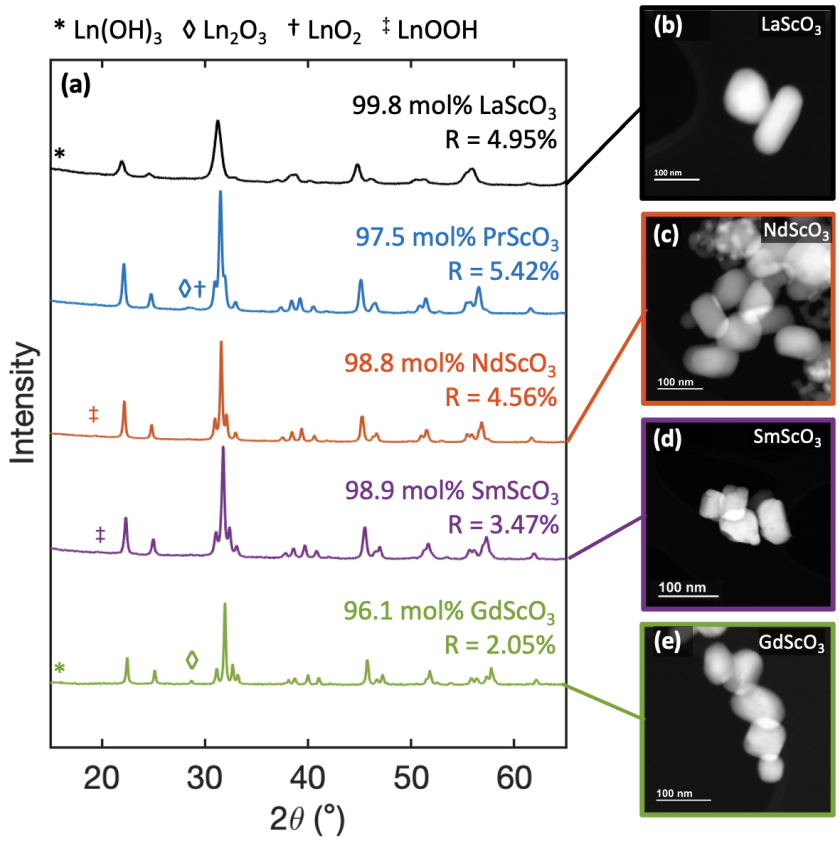

Figure 4.7. (a) PXRD patterns of $LnScO_3$ Ln = La, Pr, Nd, Sm, Gd) obtained via two-line hydrosauna synthesis by adjusting P_{H_2O} according to the trends calculating in Figure 4.6. Peaks marked with a symbol are indicative of undesired phases: * for $Ln(OH)_3$, ◊ for Ln_2O_3, † for LnO_2, and ‡ for LnOOH. (b-e) ADF STEM images of $LaScO_3$, $NdScO_3$, $SmScO_3$, and $GdScO_3$, respectively.

by comparing Figures 4.8(c) and 4.8(d)—and, especially in the cases of Nd and Sm, the formation of LnOOH.

4.5. Discussion

Reducing P_{H_2O} by transitioning from a hydrothermal to one-line hydro-sauna approach was not sufficient to form phase pure $LnScO_3$ for all lanthanides. As in Figure 4.8, the

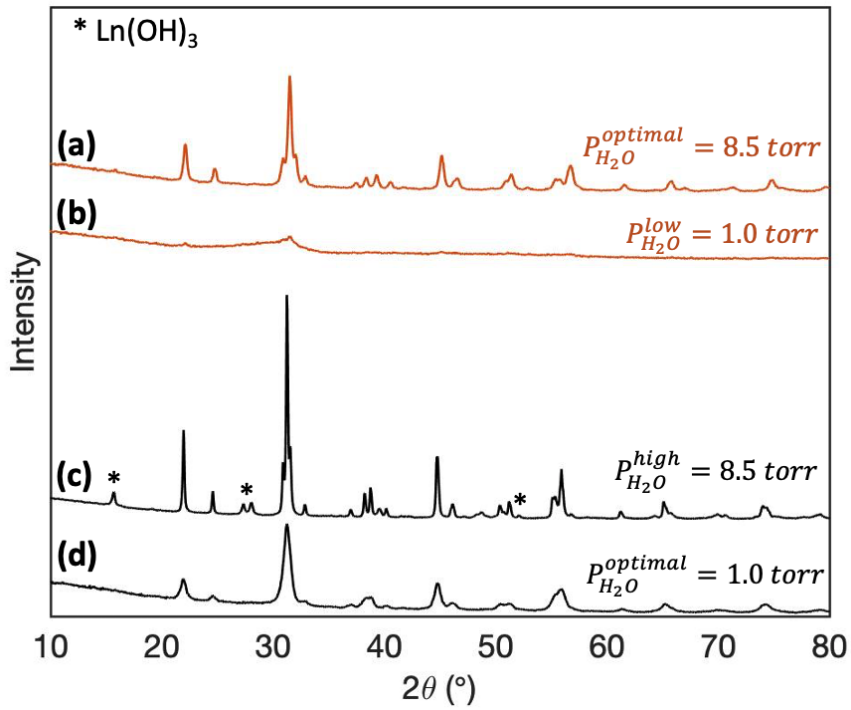

Figure 4.8. Red curves: PXRD patterns comparing $NdScO_3$ (a) synthesized at its optimal P_{H_2O} of 8.5 torr, and (b) synthesized at a lower P_{H_2O} of 1.0 torr, with broader peaks resulting from smaller crystallite sizes. Black curves: PXRD patterns comparing $LaScO_3$ (c) synthesized at its optimal P_{H_2O} of 1.0 torr and (d) synthesized at a higher P_{H_2O} of 8.5 torr, introducing La(OH)3.

amount of water vapor in the synthesis environment will significantly affect the outcome. A two-line hydro-sauna approach is needed to enable precisely controlled low P_{H_2O}. The diffraction patterns in Figure 4.7(a) further show that by adjusting P_{H_2O} in accordance with thermodynamic trends across the lanthanide series, multiple $LnScO_3$ can be achieved with a high degree of phase purity. The trend in calculated reaction energy of Eqs. 4.2 and 4.3, shown in Figure 4.6, closely correlates with the trend in P_{H_2O} that is required to synthesize high purity $LnScO_3$. Both trends essentially illustrate the water affinity of the lanthanides. $La(OH)_3$ and $Gd(OH)_3$, for example, are predicted to be more stable

compounds than other $Ln(OH)_3$ tested, which is consistent with experimental results in which the syntheses of $LaScO_3$ and $GdScO_3$ are more sensitive to excess water vapor. If we consider changing P_{H_2O} from 3 torr to 10 torr at 725 K (450°C), for example, this change corresponds to a change in water chemical potential of 7.25 kJ/mol. The increased chemical potential will have a greater effect when the driving force to form the hydroxide is small, for instance in $SmScO_3$, than it will when the driving force is large, for instance in $GdScO_3$. Thus, synthesizing $GdScO_3$ instead of $Gd(OH)_3$ requires a larger decrease in the chemical potential of water. Both the reaction energies for $Ln(OH)_3$ formation and the optimal P_{H_2O} for $LnScO_3$ crystallization exhibit this trend. The correlation demonstrates that, as hypothesized, P_{H_2O} is a crucial parameter to control phase purity in $LnScO_3$ hydro-sauna synthesis.

The electronic structure of the $LnScO_3$ gives us some insight into what causes energetic differences or differences in binding for various Ln. The partial density of states (pDOS) has been calculated for various bulk $LnScO_3$ and is shown in Figure 4.9. These pDOS indicate that Ln 4f states are closer to the valence band edge for some $LnScO_3$, for instance $NdScO_3$, than for others like $GdScO_3$. (This connects to the XPS in Figure 4.5.) The pDOS of some lanthanide scandates beyond those synthesized in this work (Ln = Pm, Eu, Tb) are also shown in Figure 4.9 to contextualize these results. The pDOS agree with the experimental XPS data shown in Figure 4.5. Compare, for instance, the sharp Pr 4f XPS peak in Figure 4.5(a) with the corresponding Pr 4f pDOS peak in Figure 4.9(b). Similarly, Figure 4.5(c) illustrates $GdScO_3$ as having purely lower-lying 4f occupied states, consistent with the Gd 4f states lying further below the valence band edge in Figure 4.9(g). The 4f electrons will therefore likely be more active in bonding in some Ln-containing compounds,

such as $PrScO_3$ or $NdScO_3$, than in others like $GdScO_3$, forming one possible contribution to the non-monotonic thermodynamics of $LnScO_3$ formation.

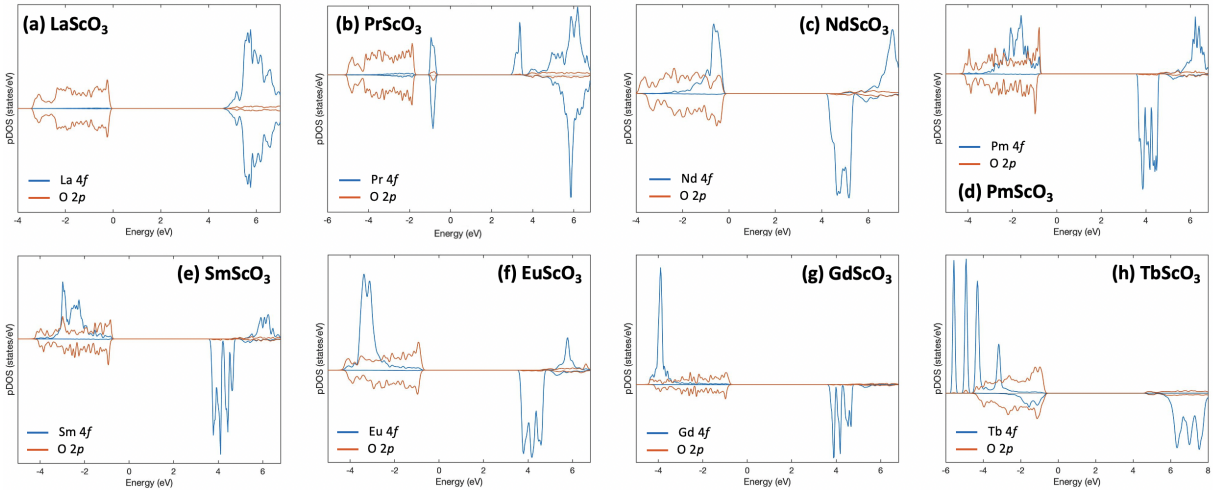

Figure 4.9. DFT-calculated pDOS of various bulk $LnScO_3$. Red lines represent the oxygen 2p contribution, while the lanthanide 4f contribution is in blue. In (a) $LaScO_3$, (f) $EuScO_3$, and (g) $GdScO_3$, the valence band edge consists largely of O2p states, while in (b) and (c) the valence band edge is dominated by Pr4f and Nd4f states, respectively. The remaining (d) $PmScO_3$, (e) $SmScO_3$, and (h) $TbScO_3$ display a more intermediate mixture of Ln4f and O2p contributions at the valence band edge.

While the trends calculated from DFT allow us to get a better handle on $LnScO_3$, there are several factors that complicate our ability to determine an exact value of the true optimal P_{H_2O} for each lanthanide. One must also consider the possibility of back-reactions: LnOOH formed during calcination may be reverted to $Ln(OH)_3$ on cooling if water vapor is still present. Given the evidence that LnOOH is more reactive and water-soluble than $Ln(OH)_3$, and thus may more easily form the mixed-cation perovskite phase,[**89, 101**] hydro-sauna synthesis was done using a two-step regime for water vapor: the appropriate DFT-predicted P_{H_2O} was applied during the high-temperature (nucleation) calcination step, then lowered by a factor of one half before cooling down to the lower-temperature

(growth) calcination step. By reducing P_{H_2O} before cooling, we can prevent back-reactions from LnOOH to the more stable $Ln(OH)_3$, resulting in a higher $LnScO_3$ weight fraction in the final product. The two-line hydro-sauna reactor allows water-saturated air to be rapidly replaced by dry argon at the appropriate time. Experiments that can elucidate the role of P_{H_2O} regimes in particle faceting and morphology are discussed further in Chapter 8.)

Another factor to consider is the polymorphic and polyphasic nature of lanthanide sesquioxides, especially those with cations of intermediate size, such as Sm_2O_3. While the hydro-sauna synthesis method requires dissolution of these oxides in nitric acid, Ln_2O_3 is still occasionally present in the final product, for example Gd_2O_3 in the $GdScO_3$ synthesis depicted in Figure 4.7(a). It follows that either some Ln_2O_3 remains unreacted or new Ln_2O_3 is formed during calcination. DFT calculations were performed using the equilibrium polymorph of Ln_2O_3 below 2000°C. For larger lanthanides, e.g. sesquioxides La_2O_3 and Nd_2O_3, their structure is hexagonal (A-type, space group $P63/mmm$); for smaller lanthanides as in Gd_2O_3, the structure is cubic (C-type, space group $Ia\bar{3}$) and for intermediate size lanthanides as in Sm_2O_3 and Eu_2O_3, the monoclinic structural form (B-type, space group $C2/m$) is most common.[**102, 115, 116, 117**] In reality, however, the Sm_2O_3 and Gd_2O_3 starting material will contain a polyphasic mixture of C- and B-type grains at room temperature. While polymorphism in the rare-earth sesquioxides has been studied extensively, the stability of certain phases and the exact nature of the polymorphic phase transitions $C \rightarrow B$ and $B \rightarrow A$ are still debated.[**100, 117, 118**] Thus, because of the limitations of the ex-situ techniques used in this work, it is difficult to say at which stages in the synthesis each secondary phase is present. These phases may include unexpected

Ln_2O_3 polymorphs, or LnOOH that is formed but not present in the final product due to rehydration to $Ln(OH)_3$ on cooling.

These complicating factors suggest there is more information to be gained about this system from in-situ X-ray techniques. Variations among the four $LnSc(OH)_6 \cdot xH_2O$ precursors prepared in this study, intermediate structures, or overall reaction mechanisms with varying Ln^{3+} could further corroborate the results of the previous section, explaining more precisely the results shown in Figure 4.8 and the underlying differences responsible for the dependence on P_{H_2O}. (In-situ X-ray techniques are discussed further in Chapter 8, with preliminary results in Appendix A.)

The PXRD results presented in Figure 4.7 demonstrate that the thermodynamic trends established herein are sufficient to guide hydro-sauna synthesis of great than 96 mol% $LnScO_3$ for five lanthanides. By combining the two-line hydro-sauna method with the thermodynamic trends calculated using DFT, the consistency of nearly phase pure $LnScO_3$ synthesis is much improved. This approach should be generalizable to other oxide materials beyond the lanthanides as well; materials made hydrothermally from a hydrogel can likely be made with greater consistency and phase purity in large batches in a hydro-sauna environment.

Challenges arise in extrapolating these findings to $LnScO_3$ of smaller lanthanides. These syntheses require higher temperatures, so we must alter our thermodynamic calculations accordingly to predict the appropriate hydrosauna condition. This idea is discussed in more detail along with preliminary results for the synthesis of $DyScO_3$ and $TbScO_3$ in Chapter 8.

4.6. Conclusion

A mixed cation hydroxide gel was calcined in a controlled humid environment to produce various $LnScO_3$. It was determined that water vapor is required to crystallize $LnScO_3$ particles with some control over their morphology, but that too high a chemical potential of water will result in the formation of LnOOH and $Ln(OH)_3$ at the expense of $LnScO_3$. By combining water-saturated and dry argon gas feeds, the humidity was greatly reduced and controlled. To determine the optimal water vapor partial pressure P_{H_2O} as a function of lanthanide, DFT was used to calculate thermodynamic trends in LnOOH and $Ln(OH)_3$ formation from water and Ln_2O_3. These trends served as a guide to the required P_{H_2O} for each lanthanide, resulting in enhanced $LnScO_3$ phase purity and consistency of results for five lanthanides. Synthesizing scandates of the smaller lanthanides i.e., beyond gadolinium, requires different considerations of stability but can still make effective use of combining computational analysis of thermodynamic trends with experiment. This approach may be general to other complex oxides as a route to consistent and scalable open-system synthesis. It also enables the development of a series of similar, highly phase-pure $LnScO_3$ nanoparticles which will be used for catalytic studies throughout the remainder of this work.

CHAPTER 5

Carbon Dioxide as a Probe for Electronic Effects in Lanthanide Scandate-Supported Gold

5.1. Introduction

While the lanthanide scandates share many chemical and structural properties, they differ from each other in two key ways. One is the lattice parameter, which will be discussed in depth in Chapter 7. The other is their electronic structure, which was discussed in Chapter 4 as a contributor to the non-monotonic thermodynamics of $LnScO_3$ formation. Here, we continue the discussion of the electron structure of $LnScO_3$ through their electron-donating capabilities. In metal oxides, electron-donating capability and basicity greatly impact their use in a variety of environmental and industrial applications.[**119**][**120**] These descriptors relate to a support material's surface chemistry and therefore to catalytic selectivity.[**121**][**122**][**123**][**95**] Thus, as catalytic supports, the electron donation of $LnScO_3$ surfaces must be isolated and quantified. This work will measure electron donation at $LnScO_3$ surfaces through chemisorption of carbon dioxide (CO_2).

Oxide-supported gold nanoparticles have long been recognized as effective catalysts in the oxidation of carbon monoxide (CO) to CO_2.[**124**] The reaction path to CO oxidation over supported Au, which minimizes intermediate phases and side reactions, allows for easier analysis and attribution of catalytic performance to fundamental properties of the

$LnScO_3$ support. As an acidic oxide CO_2 molecules adsorbs strongly onto basic oxide sites, but very weakly on noble metal particles.[**125, 126**] To highlight the role that an oxide support plays in catalysis, this chapter discusses the use of three $LnScO_3$-supported Au catalysts (Ln = La, Nd, Sm) to examine the widely-studied CO oxidation reaction:[**127, 128, 129, 130, 131, 21**]

$$CO + \frac{1}{2}O_2 \longleftrightarrow CO_2$$

Prior to reaction, the CO_2 binding strength of the support is quantified by measuring CO_2 desorption over a range of temperatures, with gas molecules desorbed at higher temperatures being more strongly chemisorbed to the $LnScO_3$ surface. This support CO_2 binding strength is identified as a significant factor in determining CO oxidation reaction rates and energy barrier in the Au/$LnScO_3$ system. While the behavior of the Au nanoparticles varies little across the supports and the $LnScO_3$ lattice parameter decreases monotonically from $LaScO_3$ to $NdScO_3$ and then to $SmScO_3$, the electron donating ability of these supports is not monotonic and correlates strongly with reaction rate.

Much of the CO oxidation study in this chapter was done in collaboration with R. Paull, Z. Mansley, E. Cheng, A. Gosavi, and J. Notestein, and appears in Reference [**59**].

5.2. Methods

5.2.1. Preparation and characterization of catalysts

Faceted $LnScO_3$ (Ln = La, Nd, Sm) were prepared via one-line hydrosauna synthesis (see Chapter 3).[**60**] The undecorated supports' surface CO_2 affinity was measured with CO_2 temperature programmed desorption with simultaneous mass spectrometry (TPD-MS)

using an AMI 200 and a SRS Universal Gas Analyzer 100, conducted by collaborator E. Cheng. The samples were heated to 350 °C for 3 h and then pre-treated with CO_2 at 50°C for 20 min before heating to 800 °C at a ramp rate of 10 °C/min with simultaneous data collection. Each $LnScO_3$ was also characterized with BET analysis using a Micromeritics 3Flex to determine the surface area.

Gold nanoparticles were deposited via deposition-precipitation by A. Gosavi guided by the method outlined by Zanella et al.[**132**] Size distribution of Au nanoparticles was conducted with Z. Mansley using annular dark field STEM performed on an FEI Talos operated at 200 kV at Argonne National Lab or a JEOL ARM300F operated at 300 kV at Northwestern University. A hemispherical shape was assumed for calculating the number of active sites. The weight loadings of Au were analyzed with either inductively coupled plasma optical emission spectrometry (ICP-OES) or inductively coupled plasma mass spectrometry (ICP-MS), using either Thermo iCAP 7600 ICP-OES operated in axial mode or a Thermo iCAP Q ICP-MS instrument operated in kinetic energy discrimination mode. The samples were digested in HCl and then diluted to a 5% concentration for analysis.

5.2.2. CO oxidation reactions

To study CO oxidation reactions of $Au/LnScO_3$, 10-15 mg of each catalyst (Ln = La, Nd, Sm) was mixed with 400 mg of quartz sand and dried for 90 min at 150 °C in a mixture of 40 sccm O_2 and 10 sccm He. The samples were then brought up to 250 °C and held for 5 h under 40 sccm O_2, 10 sccm He, and 20 sccm CO to assess catalyst stability. Under this same gas composition, catalyst performance was measured for 15 min each at 125, 150,

175, and 200 °C in order, with gases bypassing the reactor during temperature changes. Flow rates were controlled using a Camile data acquisition and control system, and the products were measured using a Pfeiffer Thermostar Q200 mass spectrometer.

5.3. Catalyst Characterization

Thorough characterization of the Au/$LnScO_3$ system was conducted beginning with the undecorated $LnScO_3$ supports. Nanoparticles of $LaScO_3$, $NdScO_3$, and $SmScO_3$ are shown through SE-STEM images in Figure 5.1, with an aberration-corrected profile view HREM image of $SmScO_3$. The faceted, cuboidal morphology in Figure 5.1(a) is consistent with what has been observed thus far in Chapters 3 and 4. The double-layer surface structure observed in Figure 5.1(b) agrees well with the results of various studies of the (110) surface of $LnScO_3$, confirming that these cuboidal shapes expose the pseudocubic $(100)_{pc}$ planes.[**52, 58, 133, 134, 135, 136, 137**] Analysis by BET yields surface areas of approximately 6 m^2/g for all three supports, which corresponds to an average side length of approximately 150 nm assuming a perfect cuboidal morphology. TEM and STEM analysis of the various $LnScO_3$ indicate that true particle widths range from about 90 nm for $LaScO_3$ to 200 nm for $SmScO_3$.

Each $LnScO_3$ was also characterized by CO_2 desorption as shown in Figure 5.2. The $LaScO_3$ and $SmScO_3$ supports desorb 30-40% of CO_2 in the low-temperature regime below 500 °C, while the $NdScO_3$ support desorbs 90% of CO_2 at higher temperatures. This finding indicates that $NdScO_3$ binds CO_2 molecules to the surface more strongly than the other two supports tested. (Regarding the choice of boundary between CO_2 weak- and strong-binding temperature regimes, note that any demarcation above 100 °C results in

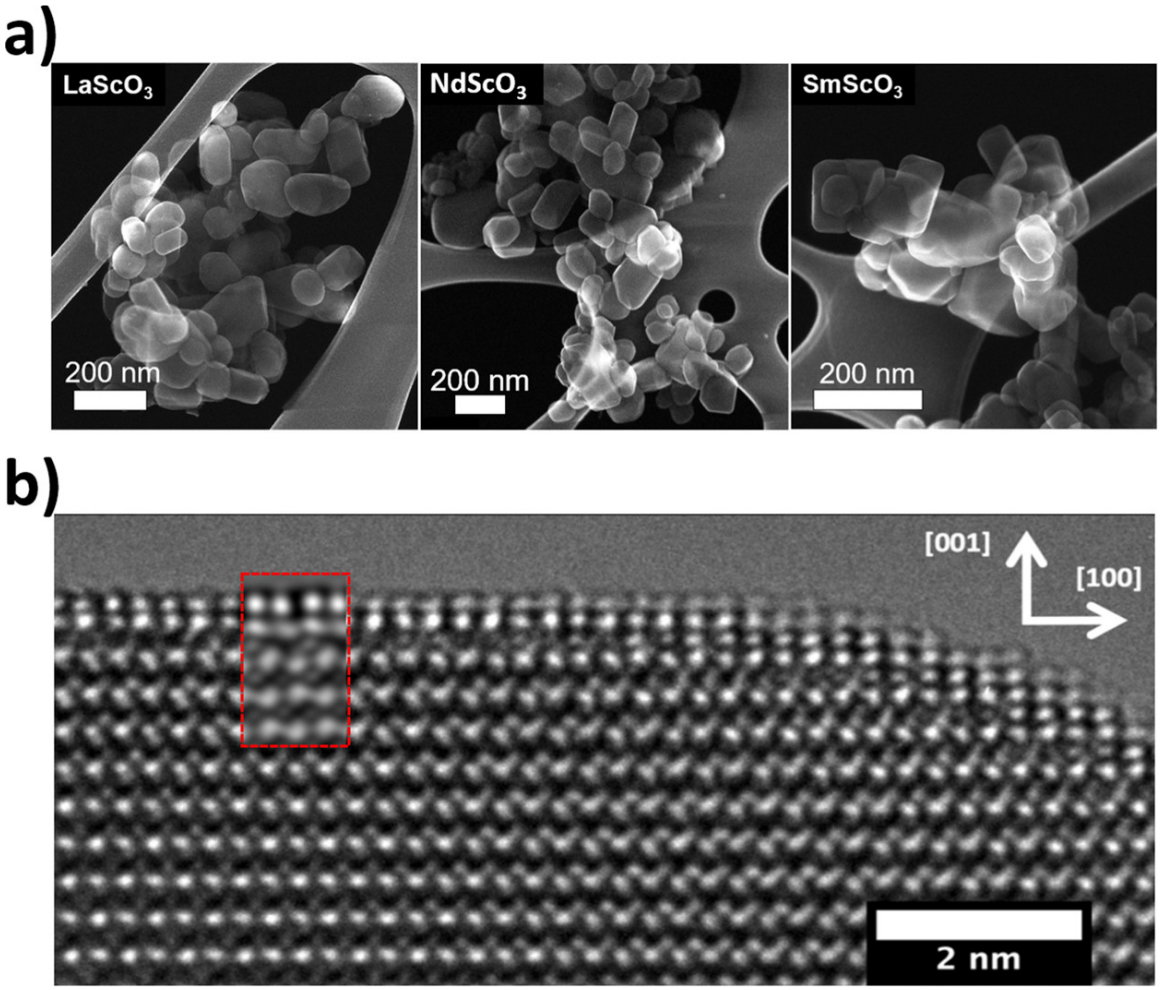

Figure 5.1. (a) Secondary electron STEM images of the different $LnScO_3$ support nanoparticles, with (b) an aberration-corrected profile image of the $SmScO_3$ surface. Highlighted in red is an inset multislice simulation generated by collaborator Z. Mansley using the MacTempasX program based on a double layer surface structure.[**52, 58, 136, 137**]

$NdScO_3$ having the highest proportion of strongly bound CO_2.) Between 125 and 275 °C, the range probed by CO oxidation experiments, $NdScO_3$ retains the most CO_2 and H_2O on the surface, followed by $SmScO_3$ and then $LaScO_3$. In addition to binding CO_2 more strongly than the other two supports, $NdScO_3$ also binds a larger overall amount of

adsorbates, on the order of $1E-4$ mol CO_2/m^2 and $1.5E-4$ mol H_2O/m^2 as compared to less than $0.2E-4$ mol/m^2 of each adsorbate measured on $LaScO_3$ and $SmScO_3$.

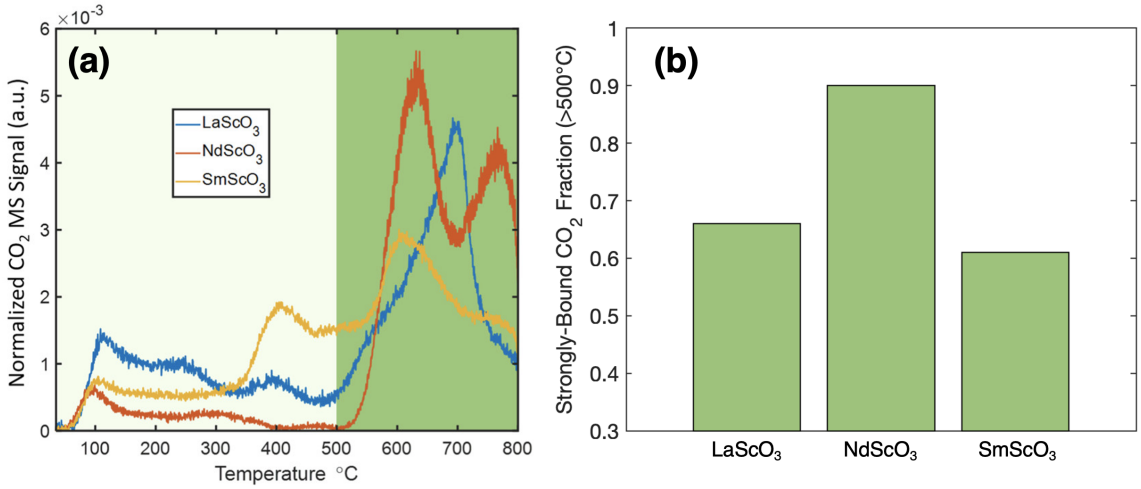

Figure 5.2. Variation of the temperature dependence of carbon dioxide desorption on three different $LnScO_3$ substrates. (a) CO_2 TPD-MS results normalized by integrated CO_2 desorption. The plot has been divided between low- and high-temperature desorption regimes at 500 °C as a means of quantifying the CO_2 binding populations of each $LnScO_3$.[**59**] (b) Fraction of strongly bound CO_2 on each $LnScO_3$.

After characterization of the bare supports, Au was deposited with measured loadings of 0.18 to 4.77 mol%. The resulting Au/$LnScO_3$ were then characterized as described in Section 5.2.1. The supported Au nanoparticles exhibited both single-crystalline and polycrystalline morphologies, as shown in Figure 5.3. Most of the polycrystals had a twinned structure, as is common in Au nanoparticles.[**138, 139, 140**] Note that the Winterbottom shape (i.e. truncated Wulff shape at the surface)[**18**] and its equivalent for twinned particles[**141**] is largely the same for particles on each of the three substrates, indicating that the free energy of the interfaces had minimal dependence on both Au particle morphology and lanthanide ion of the substrate.[**23, 140**]

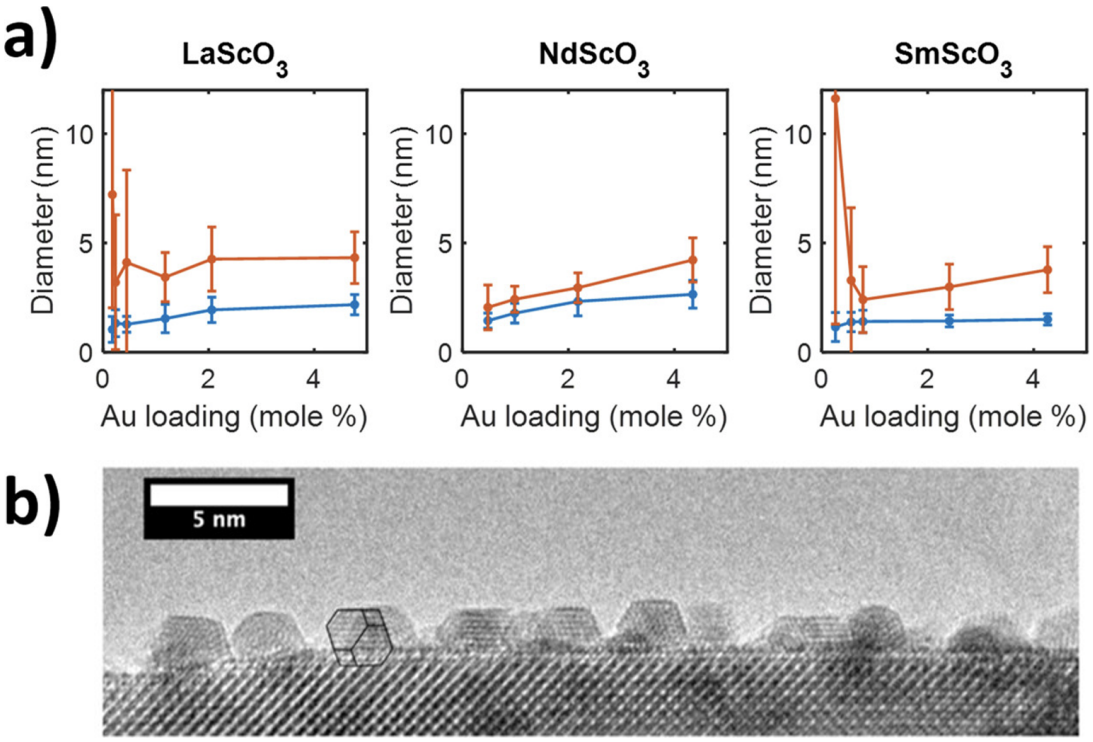

Figure 5.3. (a) Average diameters of Au nanoparticles on the various supports. As-deposited sizes are shown in blue and sizes after catalytic testing are shown in orange. Error bars show the standard deviations of each data set. (b) Aberration-corrected TEM images collected by collaborator Z. Mansley of as-deposited Au supported on a $SmScO_3$ substrate, including both multiply twinned particles and single crystals with varying orientations.

Figure 5.3(a) shows the average sizes of both as-deposited (blue) and pot-CO oxidation (orange) Au nanoparticles on each support. Because very small Au nanoparticles are more mobile and underwent runaway sintering during catalytic testing (see $LaScO_3$ and $SmScO_3$ plots in Figure 5.3(a)), the lowest Au loadings were not included in analysis of catalytic results, and these loadings were not deposited or tested on $NdScO_3$.

5.4. CO Oxidation Over Au/$LnScO_3$

The catalytic performance of each Au/$LnScO_3$ is summarized in Figure 5.4, which shows the apparent activation energies E_a (calculated from rate data between 200 and 275 °C using Arrhenius plots) and the turnover frequencies TOF of the samples at 200 °C. The TOF is normalized to the number of perimeter Au atoms at the support interface per gram of catalyst, as this reaction is frequently modeled as an interfacial reaction.[**127, 142**] The perimeter Au atoms were calculated using sizes measured after catalytic cycling. Here, the highest energy barrier consistently occured for Au/$NdScO_3$, with that barrier decreasing as the support moves to $SmScO_3$ and then $LaScO_3$. This trend exactly mirrors the trend in retained CO_2 on the support surfaces during TPD-MS measurements in the relevant temperature window. The TOF trend is less clear-cut but the reaction typically proceeded slower over Au/$NdScO_3$ at lower loadings.

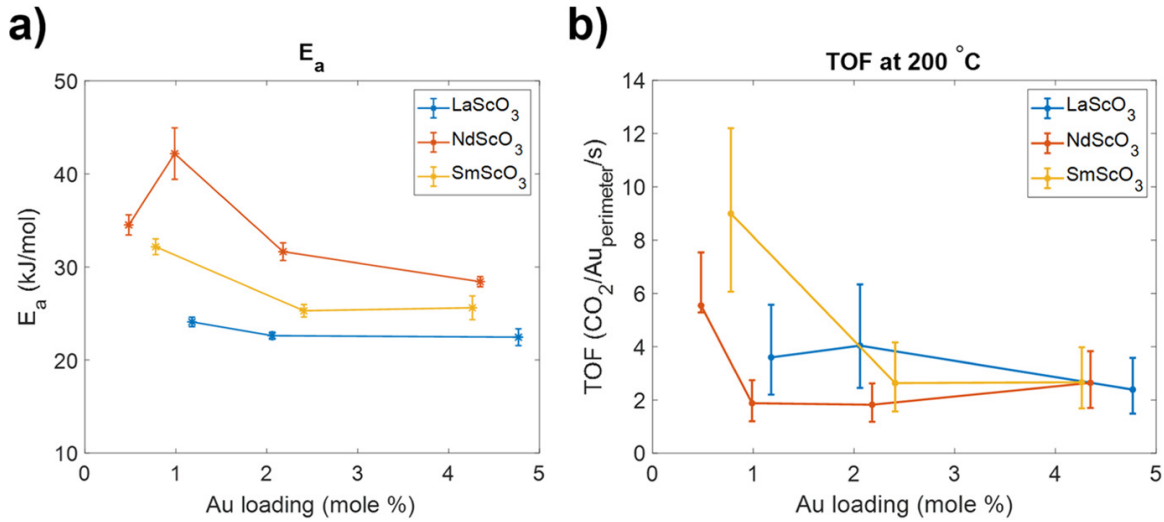

Figure 5.4. (a) Apparent activation energy of CO oxidation over Au/$LnScO_3$. Arrhenius fits and associated error bars were calculated from a linear least squares method. (b) Turnover frequencies (TOF) at 200 °C, with error bars calculated using the standard deviations of Au particle sizes.

5.5. Discussion

Owing to similarities amongst the $LnScO_3$ supports, we can eliminate many potential causes behind the observed variations in catalytic behavior. For example, since the support surfaces share a structure and Sc-rich double layer termination on the major exposed facets, the catalysis is unaffected by varied support symmetry or chemistry variations–which can be important when comparing two significantly different supports such as titania and silica. The support lattice parameter decreases monotonically from $LaScO_3$ to $NdScO_3$ then $SmScO_3$, but the observed E_a and TOF do not trend monotonically in this manner; hence, we can rule out any major epitaxial or lattice parameter effects. (In other systems, there is evidence for epitaxial contributions that appear to be directly impacted by lattice parameter.[**23, 143, 144, 145**] The role of lattice parameter in metal/$LnScO_3$ catalysis will be discussed further in Chapter 7.) This is consistent with the minimal change in interfacial free energy mentioned earlier in Section 5.3; the equilibrium truncated particle shapes do not vary significantly with the varied substrates.

The strongest correlation between catalyst properties and catalytic performance is that, within the temperature range of these experiments, $NdScO_3$ is the surface that binds CO_2 most strongly, followed by $SmScO_3$ and then $LaScO_3$. Though $NdScO_3$ has the middle lattice parameter of the three supports tested, it chemisorbs more H_2O and CO_2, and has a larger binding energy for CO_2, as demonstrated by the TPD-MS results in Figure 5.2. This trend is rationalized by the 4f electrons on the Nd sites. In Chapter 4 and previous analysis of other $LnScO_3$, it was apparent from both DFT calculations and experimental XPS data that the minority 4f electrons were close to the Fermi energy, not at deep core energies.[**59, 61, 105, 107**] They are therefore likely to be chemically active.

Furthermore, published XPS data for $NdScO_3$[**105, 109**] show a similar peak at the Fermi energy for that substrate, which correlates with the occupied portion of the bulk density of states, as shown in the previous chapter in Figure 4.9. This result is also shown in Figure 5.5, where the calculated density of states of $NdScO_3$ (three 4f electrons) can be compared directly with that of $LaScO_3$ (no 4f electrons) and $SmScO_3$ (five 4f electrons). Apparent activation energy for CO oxidation over Au/$LnScO_3$ correlates not with Ln atomic number or even number of 4f electrons, but with the chemical activity of the 4f electrons. Nd sites in $NdScO_3$ are less Lewis acidic than their La and Sm counterparts because the activity of the 4f electrons enhances the Nd sites' ability to donate electrons.

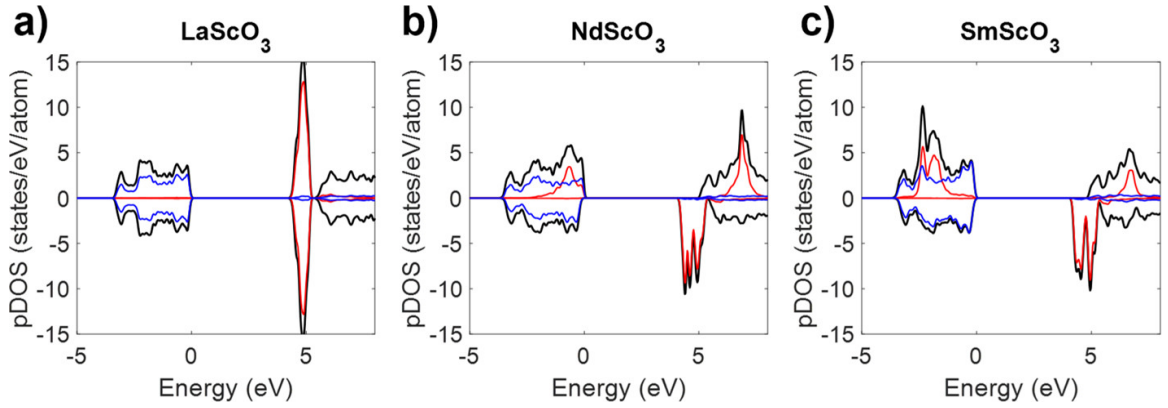

Figure 5.5. Density of states of the $LnScO_3$ materials, calculated by DFT. Black lines represent the total DOS, red lines represent the lanthanide 4f contribution, and blue represents the oxygen 2p contribution. In both (a) $LaScO_3$ and (c) $SmScO_3$, the valence band edge consists of O 2p states, while in (b) $NdScO_3$, the Nd 4f states also sit at the edge.

As a result of the $LnScO_3$ supports are scandia terminated, the effect of 4f electrons on chemisorption of electron-accepting species cannot be a result of direct electron transfer from the lanthanide. Rather, there may be an inductive effect in which the lanthanide 4f electrons affect neighboring oxygen atoms, allowing them to better donate charge. This

effect is similar to the d-band theory as described by Hammer and Nørskov,[**146**] where a higher d-band center results in stronger adsorbate interaction, though notable differences exist (e.g. d-band theory centers around the filling of antibonding states, and here, the inductive effect is instead associated with occupied states).

Turning now to the specific reaction pathway for CO oxidation, the nature and reducibility of the support generally has a large impact. For example, theoretical work by Molina and Hammer shows CO oxidation with supported Au proceeds via an Eley-Rideal (E-R) mechanism on irreducible MgO[**127**] but a Langmuir-Hinshelwood pathway on reducible TiO_2.[**147**] Additional studies report that a Mars van Krevelen pathway is possible at higher temperatures when Au is supported on a reducible support such as TiO_2[**148**] or CeO_2.[**149**] The $LnScO_3$ series once again eliminates some potential sources of variation: all are irreducible and with a basic surface like MgO, pointing towards the E-R pathway pictured in Figure 5.6. In this pathway CO binds to Au, then forms the intermediate oxidoperoxidocarbonate species[**150**] of OCOO with the assistance of electron donation from the substrate.[**127, 151, 152**] Then the intermediate decomposes before CO_2 desorbs. This process leads to an active O atom at the interface, numbered O^3 in Figure 5.6(D), which can readily react with CO. In this case the negative end of the OCOO species is above one of the metal atoms at the support surface, herein scandium.

In this pathway, the formation of the OCOO intermediate at the Au/$LnScO_3$ interface requires charge transfer to the atom labelled O^3, thus enabling the CO bound to the metal to bind with molecular O_2.[**128, 153**] Here the inductive effect of subsurface 4f electrons facilitates charge transfer to the O^3 via the Sc double layer at the $LnScO_3$ surface. The 4f electrons increase the electron activity of the system, reducing the free energy of the

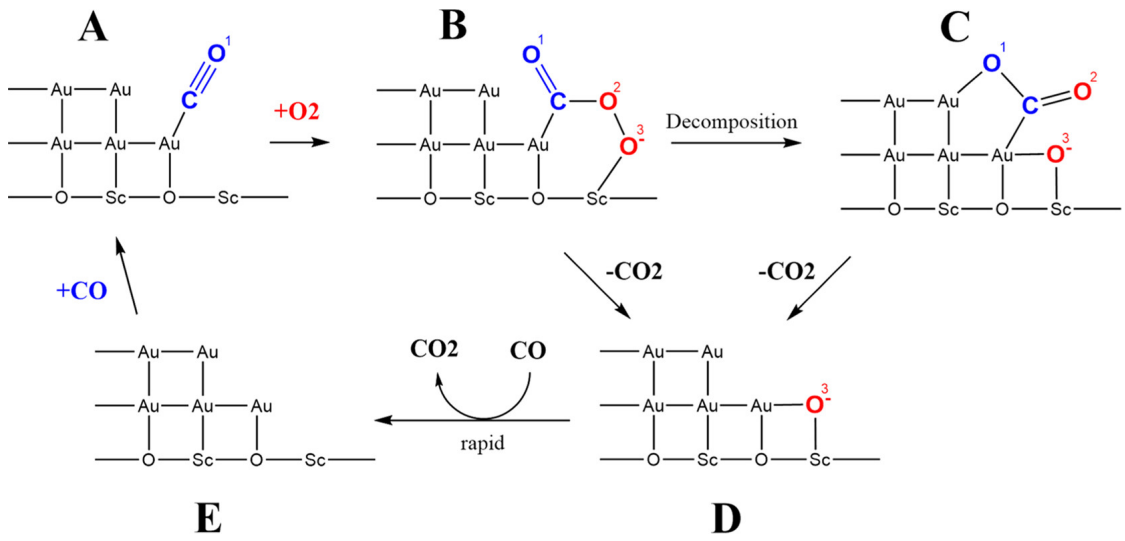

Figure 5.6. Proposed E-R reaction pathway for CO oxidation over $Au/LnScO_3$. CO bonds to Au (A) and then interacts with gaseous O_2 to form the OCOO intermediate (B), then either decomposes to (C) before desorption of CO_2 or moves directly to (D). The remaining O atom (D) readily reacts with gaseous CO to refresh the catalyst surface (E).

transition state during the formation of the intermediate. In doing so, the apparent activation energy barrier for decomposition of the intermediate is strengthened as the bond between the O^2 and O^2 atoms is strengthened. Thus, the 4f inductive effect stabilizes the intermediate species at the interface, making it easier to form the intermediate state in (B) but harder to decompose it.

In the case of $Au/LnScO_3$, the reaction is limited by these final steps of the reaction, and a stronger 4f inductive effect hinders the reaction further. The decomposed carbonate species in (C) is bonded to the metal, not the oxide, so a strong 4f inductive effect such as that of $NdScO_3$ will not lower the energy of that species. However, the inductive effect will lower the energy of (B) considerably. As a result, the energy difference between (B) and (C) is increased when the 4f inductive effect is strong, and the effective energetic

barrier for the reaction is increased. Therefore, a stronger 4f inductive effect, observed via stronger CO_2 binding in TPD-MS, corresponds to a lower rate of reaction and a larger E_a.

5.6. Conclusion

Temperature-programmed desorption has been used to characterize the CO_2 binding strength of three $LnScO_3$, which is found to correlate strongly with chemical activity of 4f electrons. Proximity of 4f electron states to the Fermi energy in both XPS and pDOS corroborate the finding that this chemical activity does not trend monotonically across the lanthanide series for the $LnScO_3$ tested herein.

The bonding of various reaction species at the Au/$LnScO_3$ interface plays a critical role; changes to the Lewis acidity of the lanthanide due to 4f electrons significantly affect charge transfer during formation and decomposition of intermediates. An in-depth understanding of $LnScO_3$ can inform interpretation of these catalytic results, enabling the prediction that CO oxidation over Au/$LnScO_3$ is limited by decomposition of an intermediate oxidoperoxidocarbonate species. A support that more readily binds this species cannot as readily decompose it to form CO_2 and recover the active site.

While the relatively strong inductive effect in $NdScO_3$ hinders CO oxidation over Au, this is not necessarily the case in all systems. The following chapter explores the system of $LnScO_3$-supported platinum, for which forming intermediates–rather than decomposing them–can become the rate-limiting step. In addition to changing the observable effect of the support on catalytic performance, Pt nanoparticles are much more likely to be single crystalline rather than multiply twinned, and Pt/$LnScO_3$ catalysts also exhibit a

cube-pseudocube epitaxy at the metal-support interface. These factors eliminate some of the complexities that arise from Au particle shapes on $LnScO_3$, as we will see in Chapter 6.

CHAPTER 6

CO Oxidation and Reverse Water-Gas Shift Over Lanthanide Scandate Supported Platinum

6.1. Introduction

The oxidation of CO over platinum has been treated as a model of catalytic action from 1922, when Langmuir measured the rate of CO oxidation over Pt wires.[**154**] Supported Pt catalysts have since been studied extensively,[**32, 130, 155, 156**] as they are model systems for working out mechanistic details of oxidation reactions[**157, 158**] and are integral to automotive emission control,[**159, 160**] fuel processing,[**161, 162**] and other applications.[**34, 163**] Platinum-based catalysts are also common in industries that make use of the water-gas shift reaction or its opposite, the reverse water-gas shift (RWGS)[**164**]:

$$CO_2 + H_2 \longleftrightarrow CO + H_2O$$

The water-gas shift and RWGS reactions affect the composition of syn-gas (CO, CO_2, and H_2), which is used to produce various hydrocarbons through the Fischer-Tropsch reaction, as well as methanol and ammonia.[**165, 166, 167, 168**] Carbon dioxide is also a component of many other catalytic reactions with commercial and environmental importance, making it a probe molecule very relevant to today's climate.[**120, 164, 169**] These reactions over Pt/$LnScO_3$ provide a good platform for studying the impacts of lanthanide on catalytic performance. While Au supported on an irreducible oxide like

$LnScO_3$ promotes the Eley-Rideal mechanism of CO oxidation depicted in Chapter 5, Pt can adsorb oxygen directly,[**155, 170**] enabling intermediate OCOO formation in which the carbon atom occupies an interfacial site, and thus will interact more directly with the support. This larger role of electron donation from the support will intensify the observable differences in catalytic performance amongst the various Pt/$LnScO_3$.

Both HREM images and DFT calculations suggest that the Pt/$LnScO_3$ metal-oxide interface is coherent; a study by Mansley et al. showed that the (110) $LnScO_3$ surface structure consists of raised O atoms that align perfectly with the corrugation of the Pt (110) surface.[**171**] Unlike the Au/$LnScO_3$ metal-oxide interface, interfaces between Pt nanoparticles and $LnScO_3$ exhibit cube-pseudo-cube epitaxial tensile strain, with the degree of strain decreasing monotonically with $LnScO_3$ pseudocubic lattice parameter. In a preliminary study of three $LnScO_3$ (Ln = La, Nd, Sm), Paull et al. found that the rates of CO oxidation and RWGS reactions over Pt/$LnScO_3$ correlated well with the CO_2 binding strength of the support, rather than with its lattice parameter.[**56**] The modifications to the hydrosauna synthesis of $LnScO_3$ in Chapter 4 enable us to replicate and expand upon this work, extending the study to more lanthanides in a (more) repeatable fashion.

In this chapter, results for both CO oxidation and RWGS reactions catalyzed by Pt supported on a series of five $LnScO_3$ (Ln = La, Pr, Nd, Sm, Gd) are described. CO_2 TPD-MS is employed to demonstrate the correlation between the support's electronic structure and reaction rates in this system. The $LnScO_3$ surface chemistry characterization and Pt/$LnScO_3$ catalysis were done in Northwestern's REACT facility with guidance from S. Alayoglu and N. Schweitzer. The Pt ALD was done in Northwestern's GIANTFab facility

with instrumentation managed by G. Han and the Notestein Group. All experiments and analyses in this chapter were done by the author and benefited greatly from discussion with Prof. Kenneth R. Poeppelmeier and Prof. Laurence D. Marks.

6.2. Methods

6.2.1. Preparation and characterization of Pt/$LnScO_3$ catalysts

Faceted $LnScO_3$ (Ln = La, Pr, Nd, Sm, Gd) supports were prepared via two-line hydrosauna synthesis (see Chapter 4).[**107**] The undecorated supports' surface CO_2 binding strength was characterized with temperature programmed desorption coupled with downstream mass spectrometry (TPD-MS) using a Micromeritics Autochem HP and a SRS Universal Gas Analyzer 100. Samples were saturated with CO_2 at 45 °C, and then ramped to 800 °C at a rate of 10°C per minute.

Platinum nanoparticles were then deposited onto the supports through a single cycle of atomic layer deposition (ALD) (see Section 2.3 for details). The weight loadings of Pt were determined with inductively coupled plasma optical emission spectrometry (ICP-OES) using a Thermo iCAP 7600 ICP-OES operated in axial mode. The Pt/$LnScO_3$ catalysts were digested in a mixture containing 2.5% HCl and 2.5% HNO_3 by volume. The total surface area of all catalysts both before and after metal deposition was determined via Brunaeuer-Emmet-Teller (BET) analysis with a Micromeritics 3Flex after a pretreatment of 6 hours at 300 °C.

To determine the size distribution of Pt nanoparticles, TEM images were taken with an JEOL ARM200CF operated at 200 kV, and ADF STEM images were taken with a Hitachi HD2300 operated at 200 kV. Both microscopes were available at Northwestern University's

EPIC facility. Particle sizes were measured with the software FIJI. A hemispherical shape was assumed for the Pt particles when calculating the number of active sites, and the number was corroborated experimentally via hydrogen pulse chemisorption operated on a Micromeritics Autochem HP instrument in Northwestern University's REACT facility. Each Pt/$LnScO_3$ was subjected to a 350 °C pretreatment of 10% H2 in N_2, then cooled to 40 °C for H_2 pulse chemisorption using N_2 as a carrier gas.

6.2.2. CO Oxidation and Reverse Water-Gas Shift Reactions

To study chemical reactions over Pt/$LnScO_3$, roughly 20 mg of Pt/$LnScO_3$ catalyst was diluted with 700 mg quartz (SiO_2) sand from Sigma-Aldrich and loaded into an Altamira BenchCAT 4000 batch reactor. The gas output of the reactor was injected into an Agilent 7890A gas chromatograph system to separate CO, CO_2, and any CH_3OH or other hydrocarbons. Each carbon oxide flow was then methanized with a Jetanizer and detected with a flame ionization detector to measure the precise relative amount of CO and CO_2 from which reaction rates were calculated.

For CO oxidation, a relatively high-oxygen environment (with an O_2 to CO ratio of 40:1) was obtained by using a premixed cylinder of 0.5% CO and 20% O_2 in He. The samples were first held at 110 °C for 6 h under 50 sccm of the gas mixture. For comparison, a relatively low-oxygen environment (with an O_2 to CO ratio of 16:1) was obtained by mixing a cylinder of 2.5% CO in He and a cylinder of 10% O_2 in He while maintaining an O_2/He flow rate four times the CO/He flow rate. These samples' stability was tested by first holding at 110 °C for 6 h under 40 sccm O_2/He and 10 sccm CO/He. After initial assessment and pretreatment in each environment, the overall flow rate was varied

from 50 – 100 sccm at 100, 90, 80, and then 70 °C, according to the example experiment profile in Figure 6.1(a) which shows the system flow rate, temperature, and CO conversion during CO oxidation over Pt/$NdScO_3$. Figure 6.1(b) shows the CO conversion plotted as a function of $(SA_{Pt})/(F * P)$, where SA_{Pt} is the active metal surface area as measured from H_2 pulse chemisorption, F is the gas flow rate, and P is the pressure. This plot was used to calculate the normalized reaction rate, which is depicted in Figure 6.1(c) in the form of the Arrhenius relationship used to calculate the apparent activation energy, E_a, as well as other parameters of catalytic performance which will be discussed in Section 6.4.

The RWGS reaction was conducted with the same general approach, using a 3:1 ratio of H_2:CO. The samples were pre-treated (Pt reduced) and assessed for catalyst stability under 50 sccm of this gas mixture. Then the overall flow rate was varied from 50 to 100 sccm at 275, 250, 235, and then 225 °C.

6.3. Catalyst Characterization

Pt/$LnScO_3$ studies were conducted using five $LnScO_3$ supports (Ln = La, Pr, Nd, Sm, and Gd) each made using the two-line hydrosauna method detailed in Chapter 4. In that chapter, it was demonstrated that this enhanced hydrosauna method produces high-purity $LnScO_3$ nanoparticles with the same *Pbnm* crystal structure and a similar crystallite shape to the particles produced via one-line hydrosauna in Chapter 3. BET surface area and TEM analyses were used to identify any significant differences between $LnScO_3$ made via one- and two-line hydrosauna synthesis.

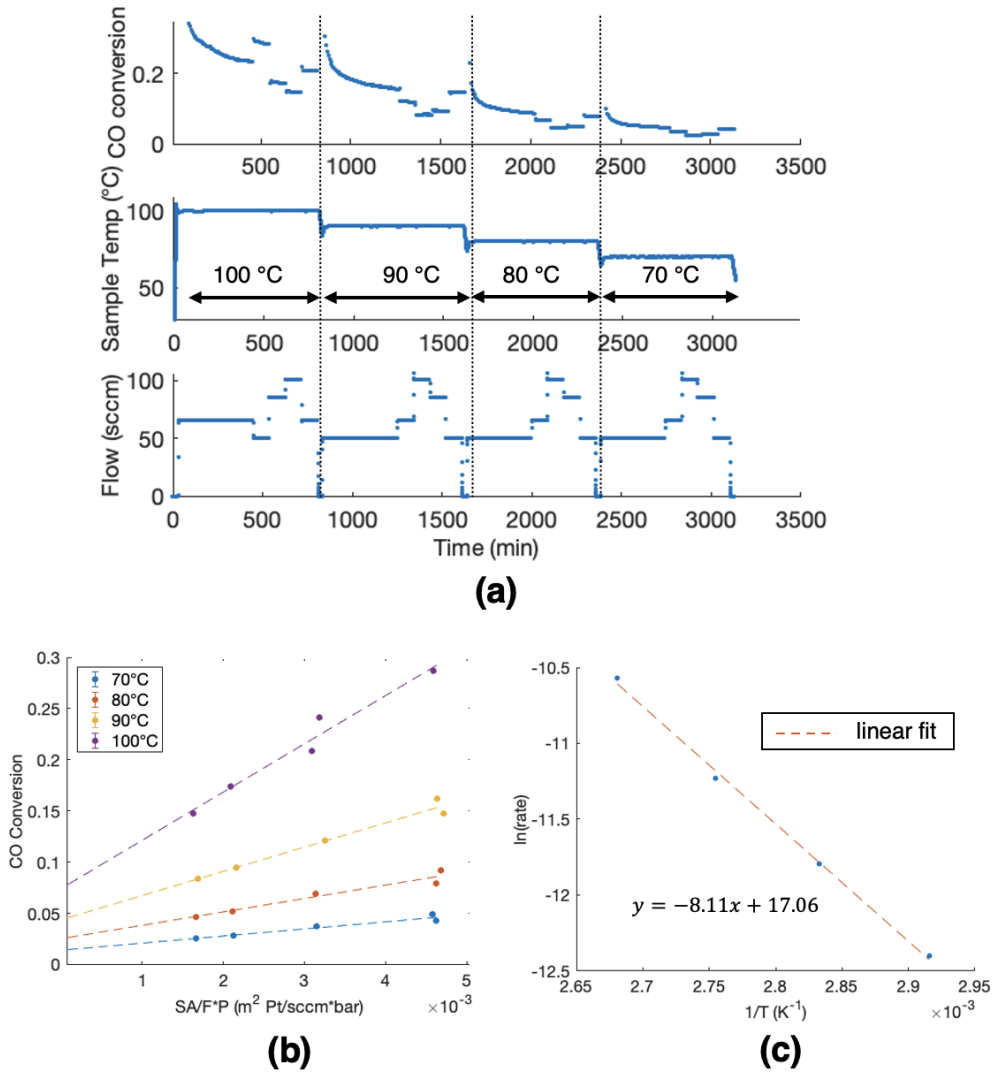

Figure 6.1. Example experiment of CO oxidation over Pt/$NdScO_3$. (a) As a function of experiment time, this plot shows the gas flow rate (bottom) and temperature (middle) measured from the BenchCAT system, and CO conversion (top) obtained from gas chromatography. (b) CO conversion plotted against $(SA_{Pt})/(F * P)$, used to calculate reaction rates. (c) Arrhenius relationship between reaction temperature and reaction rate, used to calculate apparent activation energy and other parameters defining catalytic performance.

In general, the particles prepared by two-line hydrosauna synthesis are about three times smaller than those prepared by one-line synthesis. The BET surface area of the two-line $LnScO_3$ particles ranges from roughly 25 – 35 m^2/g. TEM was used to observe that the $LnScO_3$ particles are only approximately cuboidal in shape; regardless of hydrosauna method, they have beveled corners that expose pseudo-cubic $\{110\}_{pc}$ facets,[**60**] and often the crystallites have an overall orthorhombic shape with one long axis. (See Figures 3.3 and 4.7.) Measuring across the short axis, which is always visible in 2D projection, the average width of $LnScO_3$ particles made by two-line hydrosauna ranges from about 25 nm for $LaScO_3$, to 60 nm for $GdScO_3$. Compare these findings with the 150 nm estimate for one-line $LnScO_3$ in Section 5.2—the lowered P_{H_2O} in two-line hydrosauna synthesis significantly reduces the average particle size and the size distribution, a phenomenon which will be explored further in Chapter 8.

Surface characterization of all five $LnScO_3$ was done with CO_2 TPD-MS, with results in Figure 6.2. As in the previous chapter, results indicate two main regimes of CO_2 desorption: weakly bound (physisorbed) CO_2 yields the peaks near 150 °C, while a strongly chemisorbed CO_2 regime yields the series of peaks centered near 500 °C. Though all supports made by two-line hydrosauna synthesis desorb below 60% of CO_2 in the high-temperature regime above 500 °C, $NdScO_3$ once again binds CO_2 molecules to the surface the most strongly and retains the most CO_2 on the surface in the 90 – 275 °C range (temperatures probed by the catalytic experiments in this section).

Note that while 500 °C was chosen as the boundary between "low-temperature" and "high-temperature" regimes of CO_2 desorption for simple comparison to the results in Chapter 5, it is not the only choice. In Section 5.3 it was stated that any low-high or

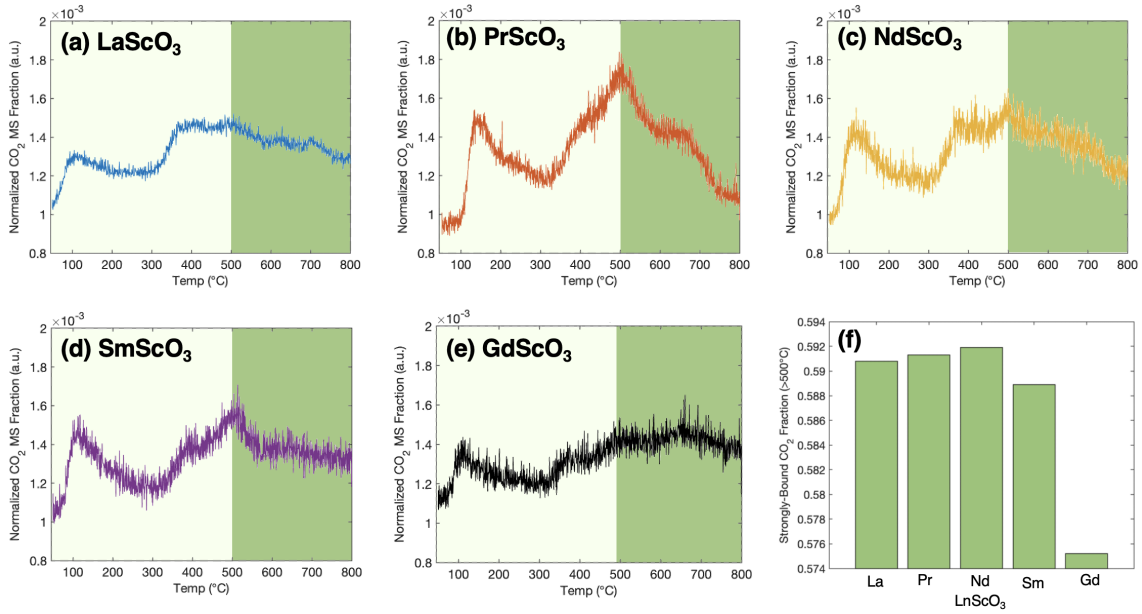

Figure 6.2. Variation of the temperature dependence of carbon dioxide desorption on five different $LnScO_3$ substrates prepared via two-line hydrosauna synthesis. Plots (a) through (e) show CO_2 TPD-MS results–normalized by integrated CO_2 desorption–for $LaScO_3$, $PrScO_3$, $NdScO_3$, $SmScO_3$, and $GdScO_3$, respectively. The plots have been divided between low- and high-temperature desorption regimes at 500 °C as a means of quantifying the CO_2 binding populations of each $LnScO_3$. Graph (f) shows the fraction of strongly bound CO_2 on each $LnScO_3$.

weak-strong demarcation above 100 °C resulted in $NdScO_3$ having the highest proportion of strongly bound CO_2. However, the inclusion of $PrScO_3$ and $GdScO_3$ allows us to observe more subtleties in CO_2 binding behavior across the $LnScO_3$ series. These can be understood from Figure 6.3, which shows not MS fraction but the raw data–normalized by $LnScO_3$ surface area–after applying a Savitzky-Golay filter for signal smoothing. In Figure 6.3(a) we can compare all five supports directly and observe that $SmScO_3$ and $GdScO_3$ are less active than the other $LnScO_3$, with peaks of lower MS signal. The integrated area under each of these curves was calculated and used to estimate the total amount of CO_2

desorbed from each support, regardless of low- or high-temperature regime. In doing so we can see that while the details of the trend across the $LnScO_3$ series will depend on our definition of "strongly-bound" CO_2, the CO_2 binding activity of $PrScO_3$ and $NdScO_3$ is definitively higher than that of the other $LnScO_3$ tested herein. The trend in amount of CO_2 adsorbed across the series is certainly not monotonic in accordance with the support lattice parameter.

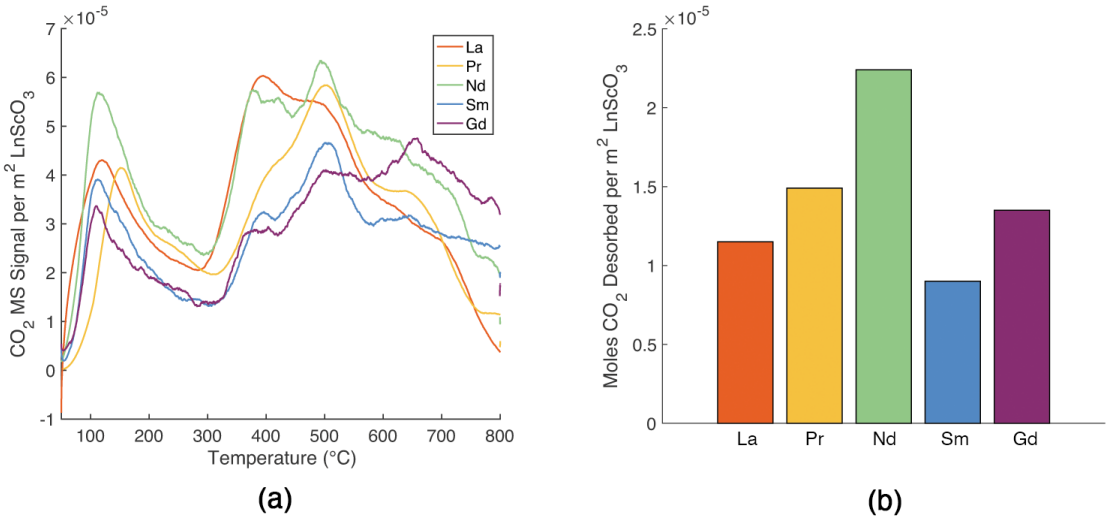

Figure 6.3. (a) Plot showing CO_2 TPD-MS results normalized by support surface area for $LaScO_3$, $PrScO_3$, $NdScO_3$, $SmScO_3$, and $GdScO_3$. (b) Total moles of CO_2 desorbed off each support, normalized by support surface area.

After characterization of the bare $LnScO_3$ support surface chemistry, platinum was deposited by ALD as outlined in Section 2.3, resulting in $Pt/LnScO_3$ catalysts with about 0.07 mol% Pt. The Pt particles were observed to be single-crystalline with a similar Winterbottom shape[**18**] on all five supports; this shape is depicted in Figure 6.4(a). Example TEM images of Pt supported on each of five $LnScO_3$ are shown in Figure 6.4(b)-(f), along with size distributions. The average Pt particle diameters were: 1.32 ± 0.30

nm on $LaScO_3$, 1.26 ± 0.25 nm on $PrScO_3$, 1.48 ± 0.28 nm on $NdScO_3$, 1.45 ± 0.26 nm on $SmScO_3$, and 1.30 ± 0.26 nm on $GdScO_3$. Analysis by H_2 pulse chemisorption yields surface areas of approximately 5 m^2 Pt per gram of Pt/$LnScO_3$ catalyst (or about 100 m^2 per gram of Pt) for all the $LnScO_3$ supports used in this section.

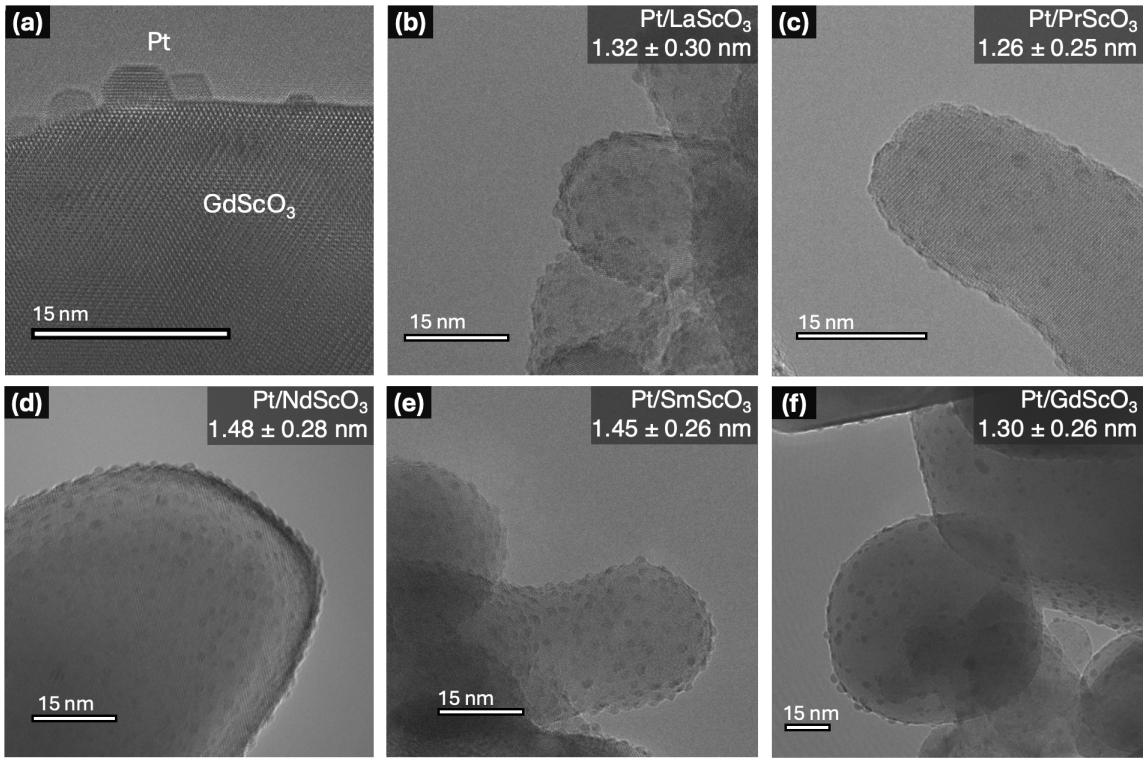

Figure 6.4. (a) TEM image depicting the shape of Pt particles supported on a $GdScO_3$ surface. Other TEM images are representative, depicting the size of Pt particles supported on larger (b) $LaScO_3$, (c) $PrScO_3$, (d) $NdScO_3$, (e) $SmScO_3$, and (f) $GdScO_3$ nanoparticles.

6.4. Catalytic Performance of Pt/$LnScO_3$

Varied catalytic conditions during CO oxidation enable us to elucidate the impact of the $LnScO_3$ support. Consider Figure 6.5, which compares the rates of CO oxidation over Pt/$LnScO_3$ at four different temperatures (70, 80, 90, and 100 °C) under two conditions:

in Figure 6.5(a), the ratio of oxygen to carbon monoxide, O_2:CO, is 40:1, while in Figure 6.5(b) O_2:CO has been reduced to 16:1. (Reaction rates were calculated using the Pt active site area measured via H_2 pulse chemisorption, assuming hemispherical particles.) Under the relatively high-oxygen environment, Pt/$LnScO_3$ yields overall faster rates of CO oxidation, while also highlighting the role of the support in catalyzing this reaction.

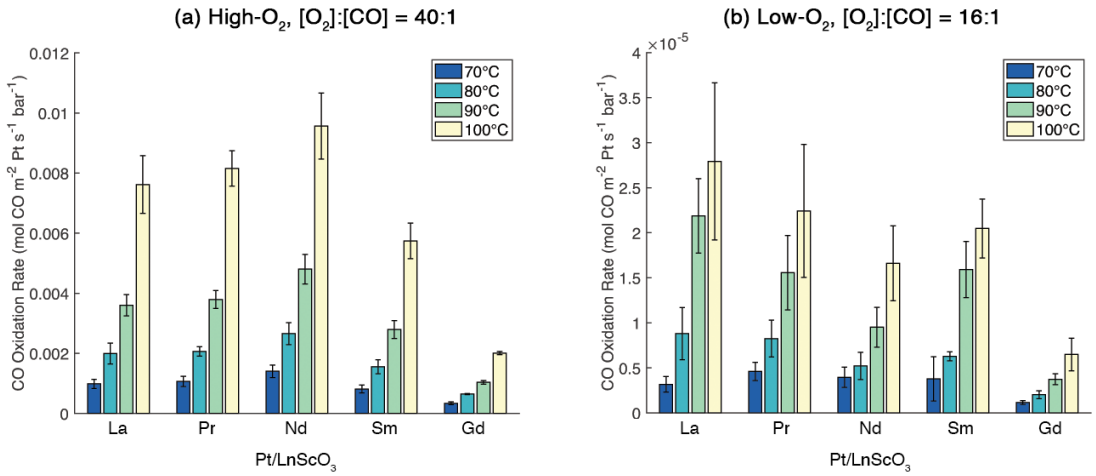

Figure 6.5. Bar graphs depicting CO oxidation rates of reaction (normalized to active Pt surface area) measured at four different temperatures (70, 80, 90, and 100 °C) for five different catalysts: Pt/$LaScO_3$, Pt/$PrScO_3$, Pt/$NdScO_3$, Pt/$SmScO_3$, and Pt/$GdScO_3$. Results are shown for two different reactant ratios: (a) O_2:CO = 40:1, and (b) O_2:CO = 16:1.

Under an oxygen rich environment, oxygen will begin to occupy interfacial sites in addition to metal sites.[**156, 163, 172**] This change in gas molecule adsorption increases the fraction of CO_2 that desorbs from an oxide site at the end of the reaction, thus increasing the importance of the role of the support. The reaction rates in Figure 6.5 illustrate this theory in action: under the more oxygen rich environment in Figure 6.5(a), differences between Pt/$LnScO_3$ are more pronounced and the rates strongly correlate with CO_2 binding strength as measured from TPD-MS. Meanwhile under the less O_2-rich

environment represented in Figure 6.5(b) the reaction rates are frequently within error of each other, obscuring any trends in $LnScO_3$ properties.

Reaction rates for the RWGS reaction over $Pt/LnScO_3$ are shown in Figure 6.6. Rates follow much the same trend across the $LnScO_3$ series as the rates of CO oxidation in Figure 6.5(a).

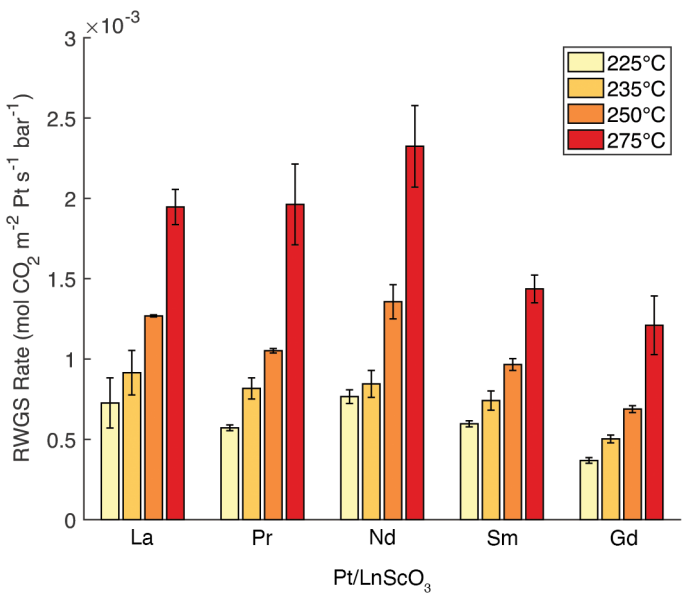

Figure 6.6. Bar graph depicting reverse water-gas shift (RWGS) reaction rates over the five $Pt/LnScO_3$ at four different temperatures (225, 235, 250, and 275 °C). Rates were calculated using active Pt surface area measured from H_2 pulse chemisorption, and $[H_2]$:$[CO_2]$ = 3:1.

The observed reaction rates, r, were plotted in the Arrhenius relationship 1/T and ln(r) (see Figure 6.7) to calculate the apparent activation energy, E_a, as well as the prefactor, A, according to transition state theory:

$$r = Ae^{-E_a/RT}$$

in which r is a reaction rate, R is the universal gas constant 8.314 $Jmol^{-1}K^{-1}$, and T is the reaction temperature.

In addition, the activation enthalpy ($\Delta H^{\ddagger}$) and activation entropy ($\Delta S^{\ddagger}$) were calculated from the reaction rates according to the Henry Eyring equation[**173, 174**]:

$$r = \frac{\kappa k_b}{h} exp(-\frac{\Delta G^{\ddagger}}{RT})$$

where k_b is Boltmann's constant, h is Planck's constant, κ is a transmission coefficient (generally assumed to be unity), and $\Delta G^{\ddagger} = \Delta H^{\ddagger} - T\Delta S^{\ddagger}$. These calculated parameters are tabulated for both CO oxidation (in the O_2-rich environment) and RWGS in Table 6.1. While κ has been shown to be less than 1 in some cases with less stable intermediates,[**175**] we have taken $\kappa = 1$ for simplicity as our focus is on the trends in values across the $LnScO_3$ series rather than the exact values themselves.

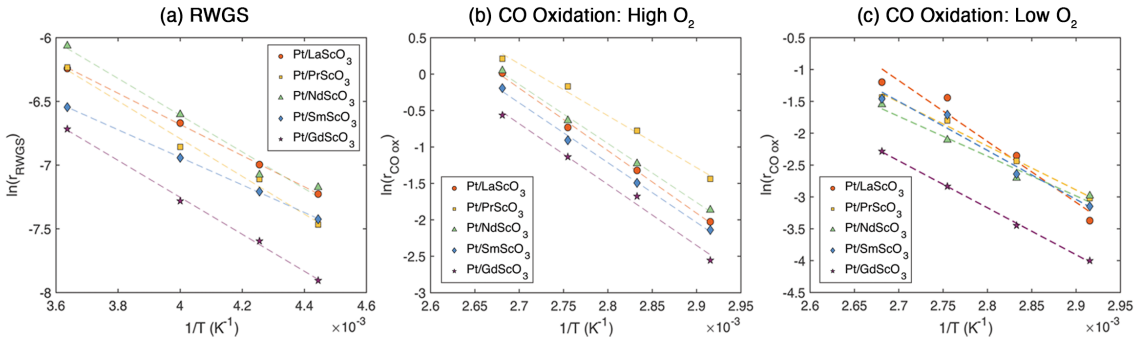

Figure 6.7. Arrhenius plots for the reactions of various Pt/$LnScO_3$-catalyzed reactions: (a) CO oxidation, $[O_2]$:[CO]= 40:1; (b) CO oxidation, $[O_2]$:[CO] = 16:1; (c) reverse water-gas shift, $[H_2]$:$[CO_2]$ = 3:1.

Table 6.1. Apparent activation energy E_a, prefactor A, enthalpy of activation $\Delta H^{\ddagger}$, and entropy of activation $\Delta S^{\ddagger}$, calculated from observed reaction rates of both CO oxidation (O_2:CO = 40:1) and RWGS (H_2:CO_2 = 3:1) over Pt/$LnScO_3$. κ is assumed to be 1.

	CO Oxidation (40:1 O2:CO)				RWGS (3:1 H_2:CO_2)			
Catalyst	E_a $(^{kJ}/_{mol})$	A $(\frac{mol\ CO}{m^2_{Pt}*s*bar})$	$\Delta H^{\ddagger}$ $(^{kJ}/_{mol})$	$\Delta S^{\ddagger}$ $(^{J}/_{mol\ K})$	E_a $(^{kJ}/_{mol})$	A $(\frac{mol\ CO}{m^2_{Pt}*s*bar})$	$\Delta H^{\ddagger}$ $(^{kJ}/_{mol})$	$\Delta S^{\ddagger}$ $(^{J}/_{mol\ K})$
Pt/$LaScO_3$	71.5 ± 2.8	7.61E7 ± 4.55E6	68.6 ± 2.8	-103.9 ± 8.2	44.7 ± 1.4	35.97 ± 1.4	40.3 ± 1.5	-228.1 ± 2.0
Pt/$PrScO_3$	59.3 ± 2.2	7.48E7 ± 5.32E6	57.0 ± 3.4	-136.4 ± 9.8	54 ± 3.8	279.3 ± 2.4	49.8 ± 3.8	-211.1 ± 5.4
Pt/$NdScO_3$	67 ± 2.2	2.56E7 ± 1.24E6	64.5 ± 2.3	-112.9 ± 6.6	52 ± 4.8	248.6 ± 3.1	48.5 ± 4.8	-212.1 ± 8.6
Pt/$SmScO_3$	68 ± 2.8	2.18E7 ± 1.30E6	65.6 ± 2.3	-114.3 ± 8.2	39.56 ± 1.0	8.55 ± 1.3	35.2 ± 1.1	-240.1 ± 4.3
Pt/$GdScO_3$	69 ± 4.8	8.63E5 ± 5.44E4	58.8 ± 3.0	-141.1 ± 8.7	53.0 ± 1.8	137.30 ± 1.5	46.7 ± 1.9	-217.0 ± 12.8

6.5. Role of Electronic Structure in Catalytic Performance

While two-line $LnScO_3$ may be smaller and more well faceted than one-line $LnScO_3$, fundamental trends in chemisorption remain the same as in Chapter 5. Consider the strength of CO_2 binding on the $LnScO_3$ surfaces. The differences between $LnScO_3$ are not as pronounced in Figure 6.2 as they are in Figure 5.2 from the previous chapter, most likely in part because of particle size. Smaller particles may expose different ratios of $\{100\}_{pc}$: $\{110\}_{pc}$ facets, resulting in different surface chemistry. The fraction of corner and edge sites of the support will change as a consequence of the smaller P_{H_2O} afforded by the two-line synthesis. Even so, among the supports tested in Chapter 5, $NdScO_3$ remains the one with the greatest fraction of strongly bound CO_2, then $LaScO_3$, then $SmScO_3$. This same trend is also reflected in the total moles of CO_2 desorbed in Figure 6.3(b).

With the addition of two new lanthanide scandates, $PrScO_3$ and $GdScO_3$, we see an extension of the theory put forth in Chapter 5: the strength of CO_2 binding to the $LnScO_3$ surface correlates with chemical activity of 4f electrons as determined by both experimental XPS and pDOS. Observe, for example, the 4f peaks in the XPS valence spectra of both PrScO and $GdScO_3$ in Figure 4.5. That of $PrScO_3$ is at the Fermi energy,[**108**] while that of $GdScO_3$ is still present in the valence band, but farther down.[**110**] The same can be said of the filled 4f states for both $PrScO_3$ and $GdScO_3$ in the calculated pDOS in Figure 4.9: one would expect the 4f electrons to be more chemically active in $PrScO_3$ than $GdScO_3$, and accordingly the inductive effect lends the surface of $PrScO_3$ more electron donating capability, such that it binds CO_2 more strongly than $GdScO_3$ does.

An exception to this rule among the $LnScO_3$ tested thus far is $LaScO_3$. Because La has no 4f electrons, one would expect its surface to chemisorb CO_2 in the weakest manner, which is counter to the behavior observed in Figures 5.2 and 6.2. However, the changes between TPD-MS results for one-line vs two-line synthesized $LnScO_3$ can give some insight into why that is. In previous sections, the $LnScO_3$ particle sizes observed from TEM were listed for both $LaScO_3$ and other $LnScO_3$, with $LaScO_3$ particles being the smallest regardless of hydrosauna synthesis method. Furthermore, based on SE STEM images which exhibit the surface topology of the nanoparticles, it is clear that $LaScO_3$ particles are also typically more rounded in shape than other $LnScO_3$, with less sharply defined corners and edges.[**60**] More detailed surface characterization, including HREM, will be needed in future to quantify this effect, observing to what extent the different morphology of $LaScO_3$ may be responsible for its chemisorption behavior. Regardless of the reason behind the observed TPD-MS, a clear correlation may be drawn between a

support's CO_2 binding strength and its ability to catalyze both CO oxidation and the RWGS reaction.

A $LnScO_3$ support's CO_2 binding strength correlates very well with both the rate of CO oxidation and the rate of RWGS reaction, regardless of synthesis method or metal catalyst. Just as the trends in CO_2 TPD-MS correlated strongly with CO oxidation rate and E_a of Au/$LnScO_3$ in Section 5.4, the CO_2 TPD-MS on two-line $LnScO_3$ shown in Figure 6.2 correlate strongly with both CO oxidation (Figure 6.5(a)) and RWGS (Figure 6.6) rates of Pt/$LnScO_3$. This finding benefits catalyst design as it suggests that intermediate binding in both CO oxidation and RWGS follows CO_2 binding. In the case of CO oxidation over Pt/$LnScO_3$, the reaction is thought to be limited by formation of the intermediate OCOO- (rather than decomposition of this species, as in the Au/$LnScO_3$ case), which is promoted by the 4f inductive effect; a stronger driving force to form and adsorb the intermediate speeds up the reaction. Analogously in RWGS over Pt/$LnScO_3$, the reaction is limited by either the adsorption of CO_2 or the formation of intermediate formates or other species. Once again, a stronger 4f inductive effect can lower the energy barrier of this limiting step, speeding up the reaction. In both cases, the adsorbates may be bound to the $LnScO_3$ or interfacial site via carbon coordination or mixed coordination,[**169**] as the effect of this 4f-aided adsorption so closely mirrors the effect of 4f-aided CO_2 adsorption.

There may be some contribution from $LnScO_3$ empty states as well as occupied states. As the strong electron donating capability of some supports will enhance a catalyst's driving force toward forming the intermediate, lower energy unoccupied states can contribute to back-bonding between the metal and CO. The case of CO binding to transition metals such as Pt is a well-known example of π-bonding between ligands and

metals.[**176, 177, 178**] In these interactions, CO acts as both a σ-donor and a π-acceptor. Analogous to the inductive effect changing the local electron donating capability of the catalyst surface, here the $LnScO_3$ unoccupied d or f states could change the Pt's ability to accept electrons, aiding in the adsorption of CO or enhancing the driving force for CO production. While the results in this work are not sufficient to claim the extent to which the inductive effect or unoccupied states contribute to the observed catalytic performance, the correlation between support CO_2 binding strength and reaction rate persists for multiple metals, reactions, and $LnScO_3$ synthesis methods, indicating a contribution from some electronic effect. Thus the 4f electrons in the $LnScO_3$ support contribute to adsorption behavior, disrupting the monotonic series across $LnScO_3$ that would be expected from Ln^{3+} cation size alone.

Less clear are the trends in other catalytic parameters in Table 6.1, including E_a and the prefactor A. These parameters do not trend well with $LnScO_3$ lattice parameter, unoccupied state energy, or 4f inductive effect alone, and are likely described by a combination of the two in addition to other factors yet unknown. In Figure 6.8, which plots the activation enthalpy as a function of activation entropy, a clear relationship is shown between entropic and enthalpic terms. Considering each parameter in Table 6.1 against the lanthanide order or even the chemical activity of 4f electrons in $LnScO_3$ does not yield any consistent trend. However, from Figure 6.8 it is clear that the entropic and enthalpic terms are related linearly in both reactions tested: regardless of Ln atomic number, a state that can become more ordered (i.e. smaller $\Delta S^{\ddagger}$ or greater $|\Delta S^{\ddagger}|$) has a lower $\Delta H^{\ddagger}$ and consequently a lower E_a and free energy of activation. A reduction in the energy difference between beginning and end states of catalysis results in a more narrow activation

barrier,[**179**] such that only a smaller number of more ordered configurations is allowed. The reduced enthalpic barrier to catalysis is thus compensated by a reduced entropy. This phenomenon has been identified many times in other series of similar reactions,[**180, 181**] and is known as the enthalpy-entropy compensation effect. A sharp activation barrier will enable only a small number of configurations, but these more ordered states correspond to smaller enthalpic barriers to catalysis.

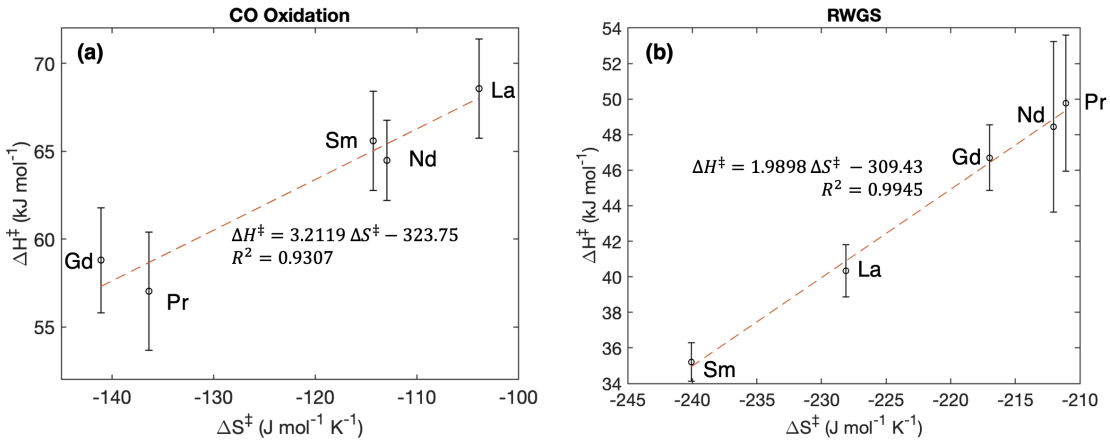

Figure 6.8. :
[CO] is 40:1) and RWGS.]Plots displaying the relationship between activation enthalpy, $\Delta H^{\ddagger}$, and activation entropy, $\Delta S^{\ddagger}$, for both (a) CO oxidation (where $[O_2]$:[CO] is 40:1) and (b) RWGS. Dashed red lines are lines of best fit whose equations are displayed along with R^2 values. Each data point is labeled with the lanthanide of its corresponding $LnScO_3$ support.

6.6. What Does the Compensation Effect Mean for Pt/$LnScO_3$?

Linear relationships between enthalpies and entropies of activation appear in dozens of fields—solvation thermodynamics,[**182, 183**] micellization,[**184**] and enantiomer separation [**185**] are only a few—and are generally observed in series of closely related reactions. In heterogeneous catalysis, this means the compensation effect is frequently observed for

a series of similar reactions over the same catalyst, or for the same reaction over a series of closely related catalysts.[**186, 187**] The Pt/$LnScO_3$ catalysts tested in this work are sufficiently similar to produce the high degree of compensation observed in Figure 6.8.

In some cases the linear $\Delta H^{\ddagger}$-$\Delta S^{\ddagger}$ relationship coincides with an isokinetic effect, i.e. a temperature β at which all reactions in the series should have the same rate constant;[**188**] however, the isokinetic and compensation effects have been identified as separate phenomena.[**181, 187**] The Pt/$LnScO_3$ series does not exhibit isokinetic behavior for any reaction conditions tested. This can be seen in Figure 6.7: there is no single point where all Arrhenius plots for one reaction intersect, and thus no single temperature for which each catalyst yields a similar rate constant. Quantitative interpretation of enthalpy-entropy compensation in the absence of an isokinetic effect is not straightforward, and is still the subject of much investigation.[**183, 186, 189, 190**]

Several reports of the enthalpy-entropy compensation effect show evidence for stronger linear correlations in cases where the series of reactions tested are more closely related.[**181, 183, 186**] For example, when in a study of Pt/γ-Al_2O_3 catalysts by Galwey et al., slight non-uniformities in the preparation of otherwise identical samples yield a very strong compensation.[**186**] This conclusion is also supported by the CO oxidation experiments in this work. From Figure 6.5 it was deduced that a more O_2-rich environment enhanced the effect of the support's electronic structure by having a greater fraction of CO_2 molecules in direct contact with the support. The more O_2-rich environment enhanced the differences between the catalysts in the Pt/$LnScO_3$ series, while the lower-O_2 environment resulted in more similar catalytic performance across the series. When the O_2:CO ratio is more than halved during CO oxidation

experiments, altering the reaction path and the observed reaction rates in Figure 6.5, the enthalpy-entropy compensation is maintained as shown in Figure 6.9, and in fact the degree of compensation is increased. The data presented in Figure 6.9 are better fit to a linear trend than the data in Figure 6.8(a).

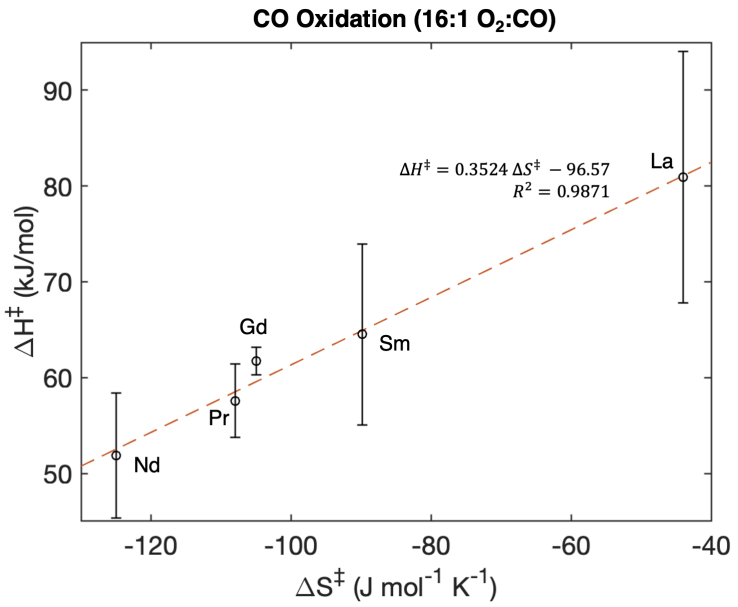

Figure 6.9. Plot displaying the relationship between activation enthalpy, $\Delta H^{\ddagger}$, and activation entropy, $\Delta S^{\ddagger}$, for Pt/$LnScO_3$-catalyzed CO oxidation in the low-O_2 environment, where [O_2]:[CO] is 16:1.

This interpretation can be extended to the RWGS experiments as well. The measured rates of RWGS over Pt/$LnScO_3$, shown in Figure 6.6, are more closely related than those of Figure 6.5(a) in which CO oxidation was conducted in a high-O_2 environment. Correspondingly, the $\Delta H^{\ddagger}$-$\Delta S^{\ddagger}$ relationship for RWGS experiments shows very little deviation from linearity in Figure 6.8(b). This could be an indication that the C of RWGS intermediates (e.g. formates, HCOO*) do not directly bind to the support. As in the low-O_2 CO

oxidation case, less frequent interactions between intermediates or CO_2 and the support will increase the observed similarity between the Pt/$LnScO_3$ catalysts.

The general conclusion put forth in Section 6.5, in which a reduced enthalpic barrier to catalysis is compensated by a reduced entropy, has thus far helped us interpret catalytic results qualitatively. However, in the absence of an isokinetic effect, there is still much development to be done in understanding any potential physical origins of the enthalpy-entropy compensation effect.[**181, 186**] For example, the general understanding described herein is not sufficient to explain a nearly exactly linear $\Delta H^{\ddagger}$-$\Delta S^{\ddagger}$ relationship, nor the order of $LnScO_3$ in Figures 6.8 and 6.9. Regarding the latter, electronic structure is not the only major factor in determining how each Pt/$LnScO_3$ catalyst responds to its environment; the roles of lattice parameter and strain will be discussed in the next chapter.

While the origins of a linear enthalpy-entropy compensation remain unclear, the Pt/$LnScO_3$ system may prove a useful tool in answering these questions more concretely. Future work may seek to use DFT to model the chemisorption of active species on $LnScO_3$ surfaces or to determine activation energies. These calculations could contribute significantly to our understanding of the physical origins of the compensation effect and why the enthalpy-entropy relationship is linear in systems of closely related reactions.

6.7. Conclusion

An expanded series of $LnScO_3$ prepared via two-line hydrosauna synthesis corroborates the findings of Chapter 5: the CO_2 binding strength of $LnScO_3$ correlates with chemical activity of 4f electrons in Pt/$LnScO_3$ supported catalysis as it did in Au/$LnScO_3$ supported catalysis. While the relatively strong inductive effect in $NdScO_3$ hindered CO

oxidation over Au, the Pt/$LnScO_3$ system is limited not by decomposition of the oxidoperoxidocarbonate intermediate but by its formation. Accordingly, the supports with the strongest electron donating capability—$PrScO_3$ and $NdScO_3$—yield the fastest CO oxidation rates in this system.

The similarities between various Pt/$LnScO_3$, and the characterization of $LnScO_3$ in earlier chapters, will provide an opportunity to study the well-known but not yet well understood enthalpy-entropy compensation effect. As the contributions to catalytic performance of various $LnScO_3$ electronic structures is understood more clearly, the similarities and differences amongst $LnScO_3$-supported metal catalysts will help us elucidate any potential mechanistic underpinnings for the compensation effect.

The electronic structure of $LnScO_3$ is not the only factor determining its behavior as a catalytic support. From trends in apparent activation energy and activation enthalpy for Pt/$LnScO_3$, we see that overall behavior is governed by at least two competing factors. The other of these is the strain at the metal-support interface, which will be discussed in the following chapter.

CHAPTER 7

CO Chemisorption on Lanthanide Scandate Supported Platinum

7.1. Introduction

The strain induced in a metal catalyst by its support is of interest in catalyst design. Introducing strain to catalyst nanoparticles is often a consequence of methods used in optimizing certain reactions, conditions, and outcomes. For example, changing the support material[**191, 192**] changes the lattice mismatch strain; alloying the catalyst metal[**193, 194, 195**] introduces atoms of differing size and chemistry into the lattice; and adjusting the nanoparticle size[**192, 196, 197, 198**] changes the surface strain leading to lattice contractions in very small nanoparticles.[**199, 200**] In all these cases, strain changes in concert with other factors that can influence the catalytic performance such as electronic effects and the orientation of the heterogeneous nanoparticles and their exposed surface.

Ideal it so minimize changes as much as possible so they are controlled. Here we achieve this using the $LnScO_3$ series, conducting an experimental study wherein the effects of changing the lanthanide are observed while many relevant properties (i.e. support surface structure, symmetry, and catalyst morphology) are held constant. As the support surface chemistry has been characterized in Chapters 5 and 6, the experiments herein allow direct correlation between lanthanide and performance.

An effective probe is the binding of carbon monoxide (CO).[**201**] In this chapter, diffuse reflectance infrared Fourier transform spectroscopy (DRIFTS) is used to study the nature of adsorbed CO on Pt/$LnScO_3$. The CO binding configuration on the Pt is found to be dependent on the $LnScO_3$ support. While the induced strain is expected to decrease monotonically in accordance with the decreasing lattice parameters across the $LnScO_3$ series, the CO binding behavior over Pt/$LnScO_3$ has both a monotonic (owing to strain) and a non-monotonic (owing to lanthanide ion) contribution. The non-monotonic contribution echoes the lanthanide 4f inductive effect described in Chapter 5 and is analyzed in more detail here using DFT.

Earlier iterations of much of the experimental work in this chapter were done in collaboration with Dr. Ryan Paull. Dr. Selim Alayoglu provided guidance on the DRIFTS experiments described in Section 7.2.2. The computational work and analysis benefitted greatly from discussions with Prof. Laurence D. Marks. Use of the Advanced Photon Source at Argonne National Laboratory was supported by the U. S. Department of Energy, Office of Science, Office of Basic Energy Sciences, under Contract No. DE-AC02-06CH11357. All DRIFTS experiments, DFT calculations, and analyses in this chapter were done by the author.

7.2. Methods

7.2.1. Preparation and Characterization of Catalysts

Five faceted $LnScO_3$ (Ln = La, Pr, Nd, Sm, Gd) were prepared via two-line hydrosauna synthesis (see Chapter 4).[**107**] Platinum nanoparticles were then deposited onto the supports through a single cycle of ALD at 200 °C, where trimethyl(methylcyclopentadienyl)–

platinum(IV) ($MeCpPtMe_3$) was used as the platinum source and ozone was used to oxidize and remove the hydrocarbon ligands (see Section 2.3 for details). The $LnScO_3$ and Pt particles were characterized using BET analysis, ICP-OES, and S/TEM as described in Section 6.2.1.

Characterization of $LnScO_3$ morphology and size, as well as of Pt particle size and distributions, was performed as described in Section 6.3. Images of the catalysts are shown in Figure 7.1 taking $Pt/NdScO_3$ as a representative example: Figure 7.1(a) shows the orthorhombic particle shape of the support, and the $Pt/NdScO_3$ catalyst is shown in more detail in Figures 7.1(b) and (c).

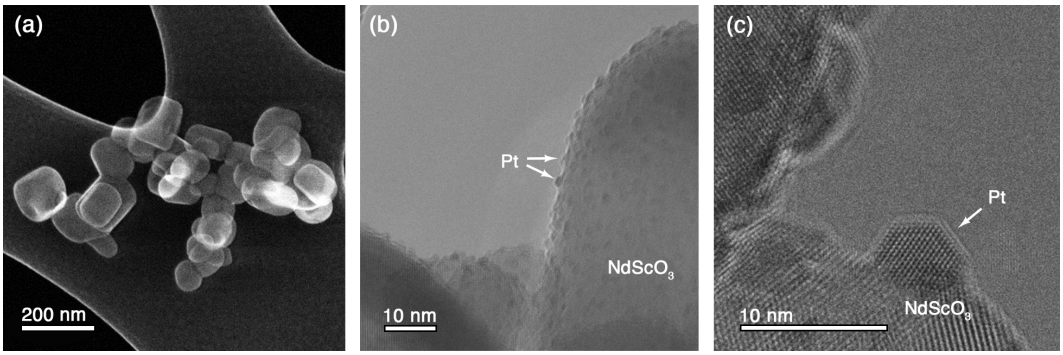

Figure 7.1. Representative images obtained to characterize $Pt/NdScO_3$. (a) Secondary electron STEM image of $NdScO_3$ nanoparticles. (b) TEM image of $NdScO_3$ particles with smaller Pt nanoparticles deposited on their surfaces. (c) High-resolution TEM image showing the shape of a Pt nanoparticle supported on $NdScO_3$.

For the analysis in this chapter, the $LnScO_3$ lattice parameters were determined with high resolution synchrotron powder diffraction data collected using beamline 11-BM at the Advanced Photon Source (APS), Argonne National Laboratory. $Pt/LnScO_3$ powders

were packed into Kapton capillaries with a 0.80 mm diameter and analyzed using an average wavelength of 0.4597 Å. Lattice parameters of $LnScO_3$ were obtained from Rietveld refinements using GSAS-II software.[**202**]

7.2.2. Diffuse Reflectance Fourier Transform IR Spectroscopy (DRIFTS)

The binding configurations of adsorbed CO on Pt metal were measured using DRIFTS. This technique utilizes the unique ways in which molecular bonds respond to IR light, determined by characteristic vibrational frequencies of the bonds. A powdered sample was tightly packed into a sample bed that then reflects incident light in all directions where it is then collected by a detector with the help of a parabolic mirror as illustrated in Figure 7.2.

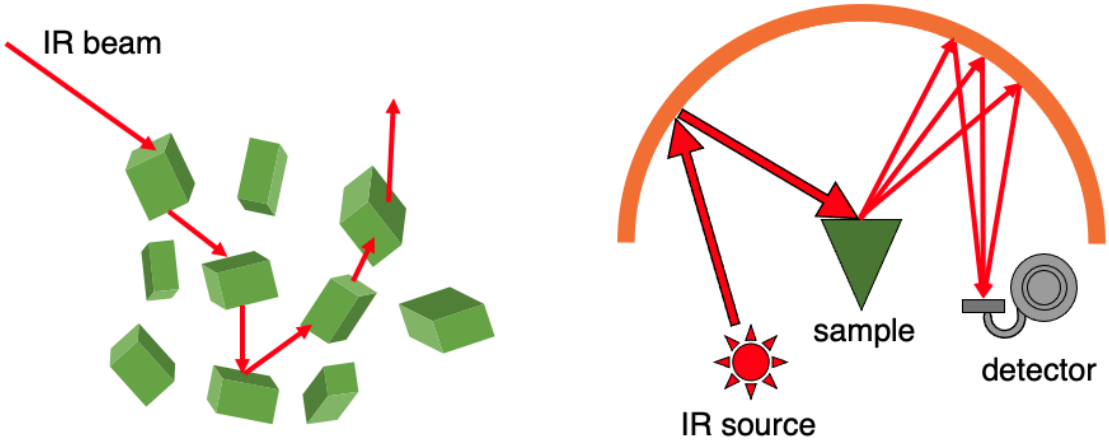

Figure 7.2. Schematic illustration of a DRIFTS experiment. The incident IR beam may either be reflected off the surface of a particle or transmitted through it, where it can either reflect off the next particle or be transmitted, etc. Scattered IR energy is collected by a parabolic mirror (orange) and focused onto the detector.

The DRIFTS experiments in this chapter were done with a Nicolet iS50 FTIR spectrometer in Northwestern's REACT facility. Each Pt/$LnScO_3$ powder was placed in a Harrick Scientific high-temperature DRIFTS chamber to enable a pretreatment: samples were heated to 300 °C in H_2 for one hour to reduce the Pt surfaces. The samples were then cooled to 40 °C in Ar for collection of a baseline DRIFTS before being exposed to 1% CO in Ar gas until saturation, with in-situ monitoring via DRIFTS collection.

7.3. Estimating Strain Induced in Pt by $LnScO_3$

Strain induced at the Pt/$LnScO_3$ interface was estimated by first determining the lattice parameters of the support for each catalyst. For the majority of supports (Ln = La, Nd, Sm, Gd), synchrotron X-ray diffraction was used to measure the values. An example in Figure 7.3(a) shows the XRD pattern for Pt/$LaScO_3$ including a Rietveld refinement on the majority phase, *Pbnm* $LaScO_3$. The pseudocubic lattice parameters measured in this manner were 4.0545(3) Å for $LaScO_3$, 4.0033(4) Å for $NdScO_3$, 3.9860(5) Å for $SmScO_3$, and 3.9761(5) Å for $GdScO_3$, each value being less than 1.5% different than the values reported for their bulk counterparts.[**50, 53, 83**] Pt/$PrScO_3$ was not measured with synchrotron XRD, and the bulk pseudocubic lattice parameter value of 4.0228(1) Å (reported by Liferovich and Mitchell[**50**]) was used for $PrScO_3$. Plotting these $LnScO_3$ pseudocubic lattice parameters against the atomic number of their respective lanthanide ions, as in Figure 7.3(b), we can see that amongst the $LnScO_3$ of the first seven lanthanides, the lattice parameter decreases monotonically, but not linearly.

Determining the lattice parameter of the Pt nanoparticles in each Pt/$LnScO_3$ is not straightforward, as Pt was not resolved in the XRD experiments described above. Such

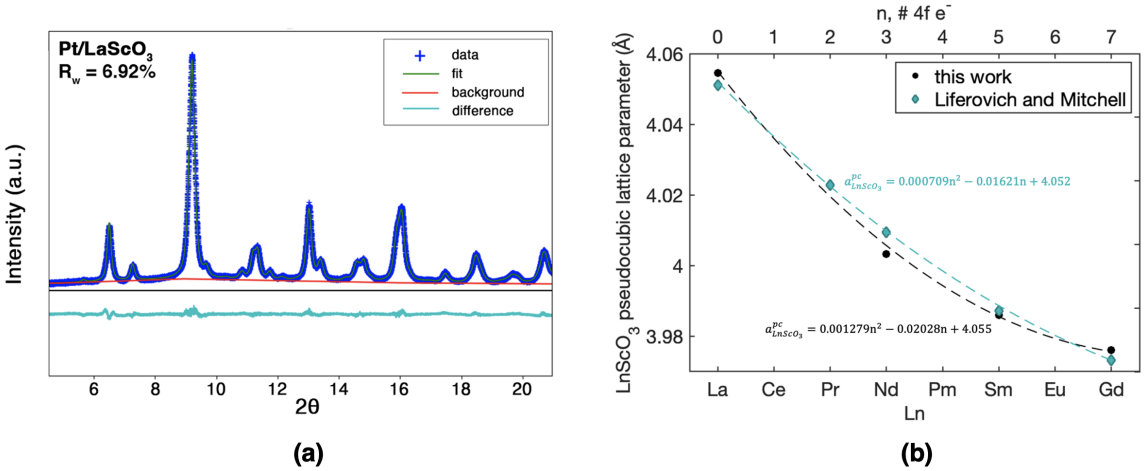

Figure 7.3. (a) Rietveld refinement on the *Pbnm* $LaScO_3$ phase of a $Pt/LaScO_3$ XRD pattern from which the lattice parameter of $LaScO_3$ was determined. The difference between the fit (green) and data (+) is shown in cyan and yields a weighted residual (R_w) of 6.92%. (b) Plot of pseudocubic $LnScO_3$ lattice parameters as a function of (bottom) the lanthanide, Ln, and (top) the number of 4f electrons in the Ln^{3+} cation, n, demonstrating a second-order polynomial relationship fit by the dashed lines. Black circles represent values from XRD measurements in this work, and blue diamonds are values reported by Liferovich and Mitchell.[**50**]

small particles lead to very low signal-to-noise ratios in XRD, and no Pt peaks are identifiable in the difference plotted in Figure 7.3(a). Furthermore, Pt accounts for only about 1% of the total sample volume and therefore only 1% of the diffracted intensity. Selected area electron diffraction in TEM has been shown to measure the lattice parameter of small metal nanoparticles to a high degree of accuracy for nanoparticles larger than 3 nm,[**203**] but below this size we have found such a measurement to be inconclusive – similar to the XRD the signal-to-noise ratio is poor. A region of sample encompassing only one or a few support $LnScO_3$ particles does not contain enough Pt particles to generate measurable diffuse polycrystalline rings in the diffraction pattern. This work instead utilizes an estimation for the Pt lattice parameter which is derived as follows.

In very small nanoparticles it is well known that the lattice parameter of Pt is usually contracted compared to the bulk lattice parameter of 3.92316(2) Å.[**204**] This has been observed experimentally[**57, 205, 206**] and it has been shown that the lattice contraction generally adheres to the theoretical interpretation put forth by Vermaak et al. in which an elastic deformation is induced by the surface stress of the small nanoparticle.[**205, 207**] In agreement with this interpretation, Leonteyv et al. have shown by XRD that a 2 nm spherical Pt particle supported on amorphous carbon will have a lattice contraction of 0.7%.[**57**] Using TEM, the size of the Pt nanoparticles on our supports was found to be around 1.3 nm on all five $LnScO_3$ supports, so we have estimated a 1.1% lattice parameter contraction ($a_{Pt} = 3.880$ Å) for Pt on all supports based on this observed Pt size and the trends predicted by other experimental work.[**57, 205**]

In addition to the effect of the surface stress, we must also consider the effect of the $LnScO_3$ supports on the Pt lattice parameter. An XRD pattern, if the scan were adjusted such that Pt could be resolved, would not simply yield the lattice parameter of the strained Pt interface as predicted by particle size. Instead, XRD will always measure an average over a large beam area, encompassing not only many particles but also the strain occurring within each particle. Models generated by techniques such as finite element[**208**] and Green's function[**209**] have modelled how strain changes throughout a single pinched hemisphere or supported nanoparticle. Here I present a simple model for estimating the overall strain in a supported Pt nanoparticle by averaging the lattice contraction of the particle surface and the lattice matching at the Pt/$LnScO_3$ interface.

Consider a Pt nanoparticle of thickness t supported on a $LnScO_3$ substrate, depicted schematically in Figure 7.4. At the top of the Pt nanoparticle (where $z = 0$), it has

the strained surface lattice parameter a_{Pt}^{surf}, the 1.1% contraction from the bulk based on elastic deformation models for the observed Pt nanoparticle size and shape. At the location $z = t$, where we can expect epitaxy at a coherent interface between Pt and $LnScO_3$,[**171**] the Pt will experience tensile strain as its lattice parameter matches that of the $LnScO_3$ substrate, i.e., $a_{Pt}(z = t) = a_{LnScO_3}$. The observed Pt lattice parameter a_{Pt}^{avg} will then be an integral average over the thickness of the particle between these two boundary conditions. For simplicity we have approximated a linear change:

$$a_{Pt}^{avg} = \frac{1}{2}(a_{Pt}^{surf} + a_{LnScO_3})$$

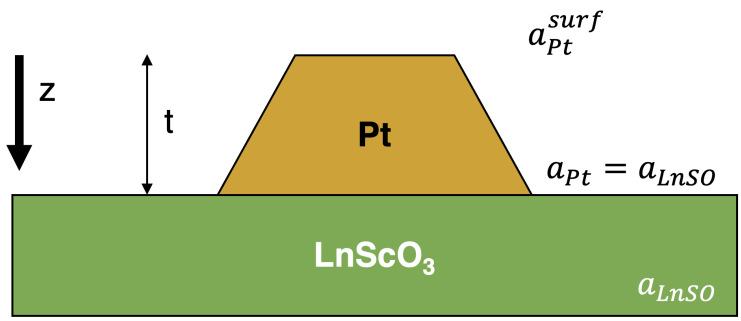

Figure 7.4. Schematic representation of the strain experienced by a single Pt particle of thickness t supported on a larger $LnScO_3$ substrate with lattice parameter a_{LnSO}. At $z = 0$, the top surface of the Pt particle, its lattice parameter is a_{Pt}^{surf}, the lattice parameter predicted by elastic deformation models. At $z = t$, the location of the Pt/$LnScO_3$ interface, the Pt lattice parameter is equal to that of the $LnScO_3$.

The results are summarized in Table 7.1, which contains the estimated strain of Pt on various $LnScO_3$. Here strain in Pt, ε_{Pt}, is referenced to the $LnScO_3$ pseudocubic lattice parameter, $a_{LnScO_3}^{pc}$, such that

$$\varepsilon_{Pt} = \frac{a_{Pt}^{avg} - a_{Pt}^{surf}}{a_{Pt}^{surf}}$$

where a_{Pt}^{avg} is the average lattice parameter of the Pt nanoparticle that would be measured experimentally (estimated from a_{Pt}^{surf} and $a_{LnScO_3}^{pc}$).

Table 7.1. Tabulated pseudocubic lattice parameters for various $LnScO_3$, $a_{LnScO_3}^{pc}$, estimations of the resulting a_{Pt}^{avg}, and strain in the supported Pt nanoparticles ε_{Pt}. The lattice parameter of bulk Pt is taken to be 3.92316(2) Å[**204**] and a 1% lattice contraction is assumed for supported 1.3 nm nanoparticles. Pseudocubic $LnScO_3$ lattice parameters are those measured from XRD in this work except where a different reference is indicated.

$LnScO_3$	$a_{LnScO_3}^{pc}$ **(Å)**	a_{Pt}^{avg} **(Å)**	ε_{Pt} **(%)**
$LaScO_3$	4.0545(3)	3.9673(3)	2.249(1)
$PrScO_3$	4.0228(1)[**50**]	3.9514(1)	1.8389(4)
$NdScO_3$	4.0033(4)	3.9417(4)	1.588(2)
$SmScO_3$	3.9860(5)	3.9330(5)	1.365(2)
$GdScO_3$	3.9761(5)	3.9281(5)	1.238(2)
$TbScO_3$	3.95850(1)[**50**]	3.91870(2)	1.0110(1)
$DyScO_3$	3.9566(1)[**50**]	3.9161(1)	0.9865(5)

This model predicts that, owing to epitaxy at the metal-oxide interface, Pt nanoparticles on all of the $LnScO_3$ tested in this work (i.e. lanthanides before terbium, Tb in the Ln series) will have an average lattice parameter greater than that of bulk Pt. The $LnScO_3$ tested here all still have pseudocubic lattice parameters that are larger than the cubic lattice parameter of Pt; the Pt nanoparticles are under tension exerted by the support in each case. $TbScO_3$ and $DyScO_3$ are not included in the $LnScO_3$ series thus far, but provide a target of interest: these are the first supports for which our model predicts an a_{Pt}^{avg} that is lower than the bulk Pt lattice parameter. (See Chapter 8for discussion of synthesis of these two supports and their potential incorporation into studies across the $LnScO_3$ series.)

It is important to note that the numerical value of the tensile strain in Table 7.1 is an estimate. The model depends on Pt particle size, which dictates the degree of surface stress at the $z = 0$ end of the Pt particle. There will also be other factors determining the lattice parameter of $LnScO_3$-supported Pt beyond the strain induced by lattice mismatch. While higher strain in the Pt nanoparticles increases the interfacial free-energy, changing the degree of wetting and thus the area of contact between metal and support, the composition of the interface and its bonding interactions will also contribute.[**23**] In the Pt/$LnScO_3$ system these effects should be minimized, but as we have already seen, the electronic structures of the lanthanide scandates do not trend monotonically across the lanthanide series as their lattice parameters do.

7.4. CO Binding Configurations on Pt/$LnScO_3$

We turn now to the effects of that strain on CO adsorption. When adsorbed on Pt metal nanoparticles, CO generally adopts one of two configurations: a more typical linear configuration atop a single Pt atom[**210**] as in Figure 7.5(a) or a bridged configuration in which binding is shared between multiple Pt atoms as in Figure 7.5(b) (in this case, two Pt atoms). $LnScO_3$-supported Pt was measured via DRIFTS for which spectra are shown in Figure 7.5(c). The large peaks in DRIFTS from roughly 2100 to 1900 cm^{-1} can be attributed to CO bound linearly atop a single Pt atom.[**211, 212**] Bridged CO appears in peaks at smaller wavenumbers, with CO bound between two Pt atoms absorbing near 1900 to 1700 cm^{-1}, or between three or four Pt atoms near 1700 to 1500 cm^{-1}.[**211, 212**] This bridge site signal is plotted on a smaller scale in the inset in Figure 7.5(d) for clarity.

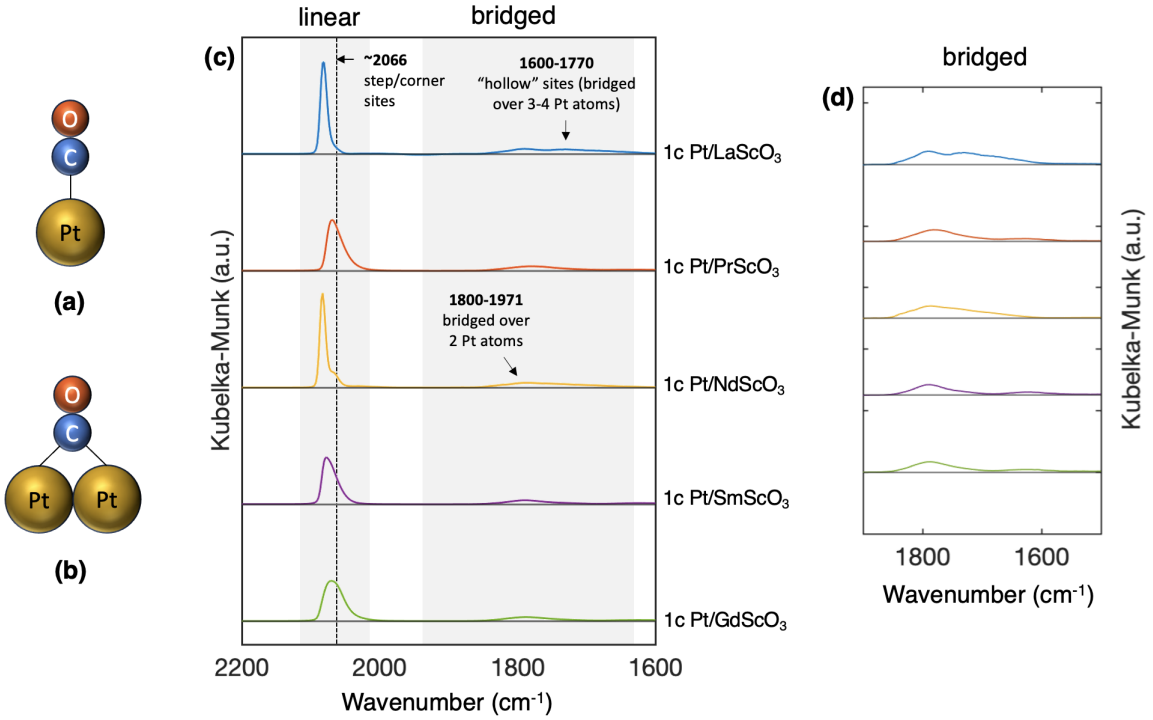

Figure 7.5. (a) Schematic of a CO molecule bound linearly atop a single Pt atom. (b) Schematic of a CO molecule bound in a bridged configuration between two Pt atoms. (c) DRIFTS for each of the five Pt/$LnScO_3$ catalysts. Large peaks highlighted at higher wavenumbers (2100 to 1900 cm^{-1}) represent CO bound linearly atop single Pt atoms, with the dashed line at 2066 cm^{-1} indicating the location of a shoulder associated with linear CO bound at step or corner sites. Peaks highlighted at lower wavenumbers are attributed to bridged CO shared between either two (1971 – 1800 cm^{-1}) or three to four (1600 – 1770 cm^{-1}) Pt atoms. (d) Inset of plot (c) showing bridged site signal on a smaller scale for clarity.

Integrating the area under each of these bands gives a proxy for how much CO is bound in each configuration. These results are summarized in Figure 7.6, where the fraction of CO bound in a bridged configuration is plotted against estimated Pt/$LnScO_3$ strain. While the tensile strain decreases monotonically with decreasing $LnScO_3$ lattice parameter, the percentage of CO bound in the bridged configuration does not. Pt/$PrScO_3$ has the highest percentage of CO bound on bridged sites (39.4%), while the percentage

decreased monotonically with decreasing lanthanide ion size for the other Pt/$LnScO_3$ (33.5%, 31.1%, 22.0%, and 20.2% for Pt on $LaScO_3$, $NdScO_3$, $SmScO_3$, and $GdScO_3$, respectively). The DRIFTS results are compared against the trend in Pt/$LnScO_3$ strain estimated from pseudocubic $LnScO_3$ lattice parameters measured by XRD in Figure 7.6(a) while in Figure 7.6(b) the Pt/$LnScO_3$ strain is estimated from the pseudocubic $LnScO_3$ lattice parameters reported in Reference [**50**]. Note that DRIFTS results were found to be highly dependent on Pt particle size and shape, so consistent Pt deposition and pre-treatment in the DRIFTS chamber was required to enable meaningful comparisons across the Pt/$LnScO_3$ series (see Appendix B for details). While the Pt morphology was found to be relatively constant on this support series, we note two different peak shapes and positions—observe the shape and wavenumber shift of the Pt/$LaScO_3$ and Pt/$NdScO_3$ spectra as compared to the other three—whose origins could be explored in future studies.

The non-monotonic CO binding behavior observed in Figure 7.6 is perhaps surprising considering that there exist theories which suggest the fraction of multi-bonded CO on Pt should increase with decreasing strain in the Pt. From an atom-atom distance perspective, Pt nanoparticles with less tensile strain provide more opportunities for bound CO to be shared amongst more than one atom in the Pt nanoparticle. However, this theory glosses over complexities such as bond angle, which depends on strength of CO-metal binding.[**213**] Moving on to electronic and chemical effects, the general d-band theory for late transition metals predicts that strain impacts the chemical properties of metal surfaces: the d-band center ϵ_d increases as the metal coordination number decreases, so increasing tensile strain raises ϵ_d, causing adsorbates such as CO to prefer bridged sites and to adsorb with a lower binding strength.[**146, 214, 215, 216**] These predictions are

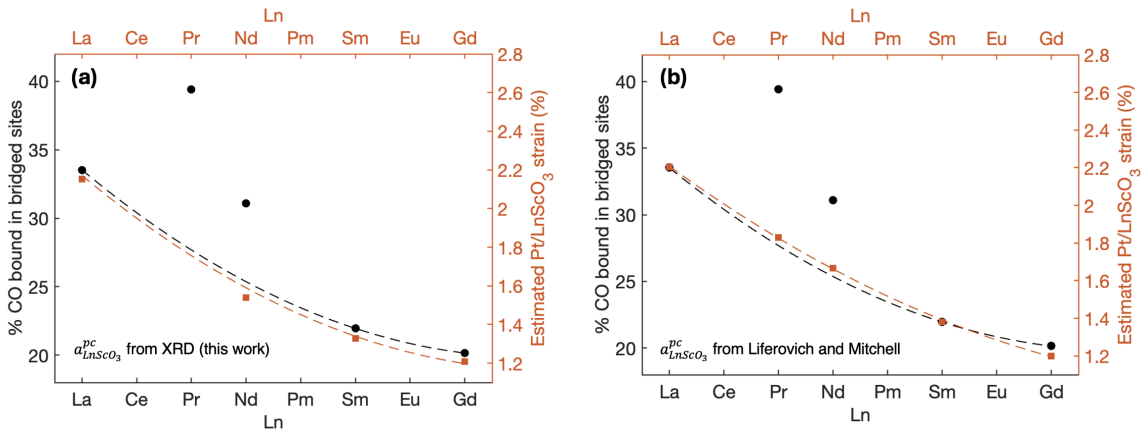

Figure 7.6. Plots showing percentage of CO bound to Pt/$LnScO_3$ in a bridged configuration (left axes, black circles) and estimated Pt/$LnScO_3$ tensile strain (right, orange squares) as a function of lanthanide, Ln. In (a) the strain is estimated from the pseudocubic $LnScO_3$ lattice parameters measured by XRD in this work, while in (b) the strain is estimated from the pseudocubic $LnScO_3$ lattice parameters reported in Reference [**50**]. The dashed lines indicate the trends expected based on $LnScO_3$ lattice parameter to highlight how Pt/$PrScO_3$ and Pt/$NdScO_3$ deviate from the expected trend.

in agreement with theoretical studies of the present system in which CO over strained Pt binds more strongly at linear or "atop" sites which occur in greater numbers when the Pt surface has less tensile strain.[**217, 218**] However, the systematic use of the series of $LnScO_3$ demonstrates that strain is not the only source of electronic effects which may alter CO adsorption to a supported metal.

The unexpectedly high fraction of CO bound in the bridged configuration on Pt/$PrScO_3$ and Pt/$NdScO_3$ can be explained in the context of the lanthanide 4f effect introduced in Chapters 5 and 6. Those chapters showed how Ln 4f electrons can contribute to the electron donating capability of various $LnScO_3$ surfaces, with $PrScO_3$ and $NdScO_3$ showing the greatest electron donating capability. Using DFT, we can understand how

electronic factors of the support may affect CO binding to $LnScO_3$-supported platinum surfaces. This is done using Bader charge analysis in the next section.

7.5. Incorporating Non-Monotonic $LnScO_3$ Behavior: Bader Analysis

The Bader charge is a good metric of the electronic charge associated with an atom in a molecule.[**219, 220**] Determining this charge requires setting the boundaries of each atom, within which is contained its associated charge density. One method for determining these boundaries originates from Richard Bader's Quantum Theory of Atoms in Molecules (QTAIM).[**219, 221**] His theory defines an "atomic basin"—the volume associated with only one atomic nucleus—purely based on the topology of a molecule's electron density. This topology, called the Bader surface, is defined as the surface through which a gradient vector of electron density has no flux. In other words, the charge density is at a local minimum along the Bader surface. Precisely, the Bader surface is defined by:

$$\nabla\rho(\mathbf{r_s}) \cdot \hat{n}(\mathbf{r_s}) = 0$$

for all points r_s on the surface, where ρ is the charge density and $\hat{n}$ the surface normal unit vector.

Consider the diagram in Figure 7.7 which depicts this topology for a simple H_2 molecule. The maximum of the charge density surface indicates the positions of atomic nuclei, while the minimum of the surface of charge density indicates the point between the atoms, thus defining where the volume of one atom ends and the next begins. This topology thus defines the volume and position of each atomic basin, or the boundaries within which lie that atom's charge density.

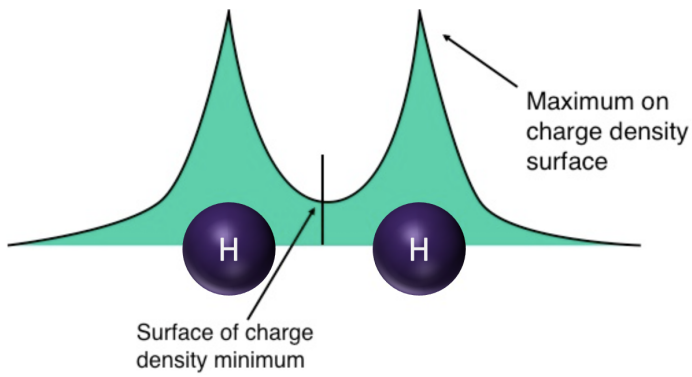

Figure 7.7. Diagram illustrating how the charge density surface is used to define the volume associated with each atom in a material. The charge density maxima indicate the positions of the atoms' centers, while the minimum indicates the boundary between two atoms. Figure adapted from [**222**].

Herein I calculated the Bader surface of $LnScO_3$, determining the Bader charge of each lanthanide as well as the charge density along the Ln–O bond in each structure. The AIM (Atoms in Molecules) program in WIEN2k[**73**] was used to analyze the topology of the electron density of all five bulk $LnScO_3$ structures. Provided a well-converged charge density (calculated according to the methods in Section 2.4), this program calculates the gradient at each point both within the interstitial regions and within the muffin-tin spheres, searches for critical points (CP's) on the surface, and then integrates the charge density within an atomic basin. Figure 7.8 shows a $LnScO_3$ structure highlighting the locations of the "bond critical points" between Ln and O atoms. (Note bond critical points are those with (3,-1) character that indicate two neighboring atoms with a bond between them. This notation indicates that in a three-dimensional system, the electron density falls down in two perpendicular directions (-2) and rises in one (+1), i.e. this

critical point looks like a saddle point with a maximum in two spatial directions and a minimum in the third.)

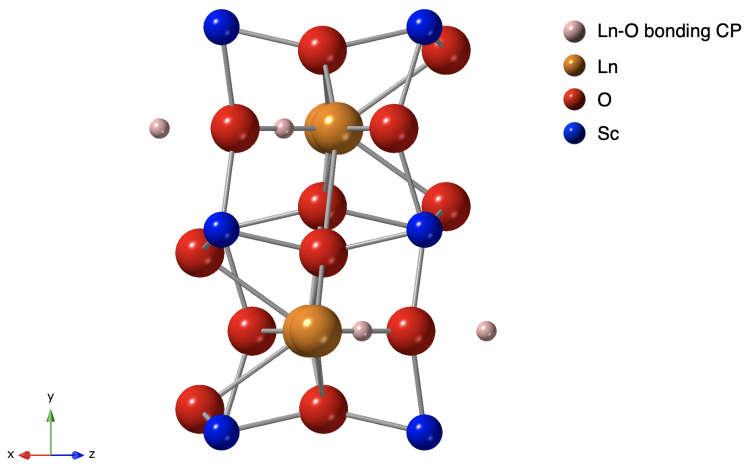

Figure 7.8. $LnScO_3$ *Pbnm* structure, viewed along [110], with the locations of each critical point (CP) in the charge density along Ln-O bonds indicated by the position of a pink sphere.

The electron density was calculated at the highlighted critical point in each $LnScO_3$ structure, designated ρ_{CP}, along with the Bader charge Q associated with each lanthanide atom. The Pr-O bond in $PrScO_3$ had the lowest critical point electron density at 0.380 $e/\text{Å}^3$, followed next by Nd-O in $NdScO_3$ (0.433 $e/\text{Å}^3$) and then the other lanthanides. The Nd atom in $NdScO_3$ had the lowest Bader charge at 2.122 e, followed next by Pr in $PrScO_3$ (2.123 e) and then the other lanthanides once again. The results are summarized in Table 7.2.

To lend some context to these results, ρ_{CP} was also calculated for the metal-oxygen bonds in three well-known metal oxides: MgO, CuO, and Cu_2O. The structures of these oxides are shown in Figure 7.9. At the critical point in the ionic Mg-O bond in MgO, the electron density was 0.259 $e/\text{Å}^3$. For the more covalent Cu_2O, the Cu–O bond ρ_{CP} was

Table 7.2. The electron density at the Ln-O bonding critical point, ρ_{CP}, and the Bader charge Q of the Ln atom for each $LnScO_3$ bulk structure.

$\mathbf{LnScO_3}$	$\rho_{\mathbf{CP}}(\mathbf{e/Å^3})$	$\mathbf{Q(e)}$
$LaScO_3$	0.473	2.218
$PrScO_3$	0.380	2.123
$NdScO_3$	0.433	2.122
$SmScO_3$	0.435	2.129
$GdScO_3$	0.472	2.147

0.780 $e/Å^3$, and CuO presented an intermediate case for which the Cu–O bond ρ_{CP} was 0.672 $e/Å^3$.

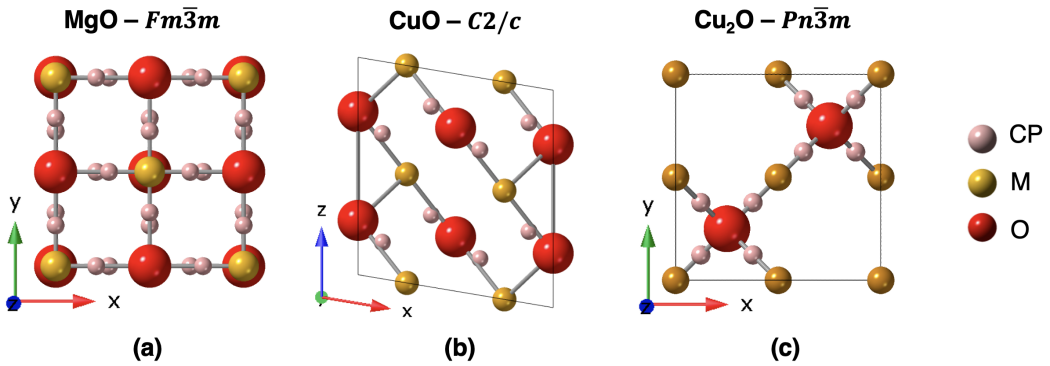

Figure 7.9. Structures of three different metal oxides: (a) MgO viewed along [001], (b) CuO viewed along [0$\bar{1}$0], and (c) Cu_2O viewed along [001]. The locations of the metal-oxygen bonding critical points (CP) are highlighted in pink.

Assuming a greater electron density at the M–O bond critical point indicates a more covalent bond, we can now order the $LnScO_3$ supports according to the ionicity of their Ln–O bonds. This arrangement is displayed in Figure 7.10, where the Ln–O bonding in $PrScO_3$ and $NdScO_3$ is more ionic than in the other three $LnScO_3$. These results echo

the trend in Figure 7.6 in which monotonic CO adsorption across the $LnScO_3$ series is disrupted by $PrScO_3$ and $NdScO_3$, likely owing to their electronic structures. The Ln 4f electron contributions to the top of the valence band in these two $LnScO_3$ may also affect the Ln-O bonds such that these phenomena are all connected, and all give rise to the previously noted inductive effect.

Density (e/Å³) at metal – O bond critical point

Oxide	MgO	$PrScO_3$	$NdScO_3$	$SmScO_3$	$GdScO_3$	$LaScO_3$	CuO	Cu_2O
ρ_{CP} (e/Å³)	0.259	0.380	0.433	0.435	0.472	0.473	0.627	0.780

decreasing ionicity

Figure 7.10. All five $LnScO_3$ and the binary oxides MgO, CuO, and Cu_2O arranged in order of increasing ρ_{CP} or decreasing ionicity.

Those $LnScO_3$ with more ionic bonding enhance the supported Pt metal's ability to donate electrons for bond formation via the inductive effect: the O in these structures is more able to donate charge, affecting neighboring Ln-O bonds, eventually altering the local electronic environment at the Pt/$LnScO_3$ interface and in the Pt itself. Thus, the multiply bound configurations of CO are more favored on Pt/$PrScO_3$ and Pt/$NdScO_3$ than would be expected from strain alone, accounting for the deviation from monotonic behavior that was observed in Figure 7.6. In the study of CO oxidation over Au/$LnScO_3$ in Chapter 5, the electronic structure of $NdScO_3$ made that support better able to donate electrons for CO_2 chemisorption as compared to $LaScO_3$ or $SmScO_3$.[**59**] The present study indicates that this effect also extends to the supported metal.

By fitting the DRIFTS data to a linear combination of $a^{pc}_{LnScO_3}$ and ρ_{CP}, we can estimate the relative contributions of each. Consider the representation of DRIFTS results in Figure 7.11 which again plots, as a function of lanthanide, the fraction of CO bound to

Pt/$LnScO_3$ in a bridged configuration. The data is well matched to the linear combination (blue diamonds in Figure 7.11):

$$\text{bridged CO fraction} \approx 1.9688 a^{pc}_{LnScO_3} - 1.1790 \rho_{CP} - 7.0711$$

Thus $a^{pc}_{LnScO_3}$ and ρ_{CP} have opposing contributions to CO adsorption: a support with a larger $a^{pc}_{LnScO_3}$ yields a greater fraction of bridged CO, but a support with a larger ρ_{CP} at the Ln-O bond critical points yields a smaller fraction of bridged CO. In the Pt/$LnScO_3$ system–and with $a^{pc}_{LnScO_3}$ in Å and ρ_{CP} in e/Å^3–the fraction of bridged CO is approximately proportional to twice the lattice parameter minus the electron density at the Ln-O bond critical point. This approximation provides a target for computational work which may seek to model the chemisorption of CO on Pt/$LnScO_3$ in detail and provides some guidance regarding how the Pt/$LnScO_3$ series may be useful in metal-support interaction studies.

Bridged CO sites on Pt have been identified as more active in several different catalytic reactions, including CO oxidation or the water-gas shift reaction;[**158, 223, 224**] in this way, strain engineering of catalysts could be used to promote a higher percentage of more active sites. This connection between bridged CO binding and greater activity agrees with the results of Chapter 6, in which Pt/$PrScO_3$ and Pt/$NdScO_3$ catalysts yielded faster reaction rates for both CO oxidation and RWGS, with Pt/$GdScO_3$ always yielding the slowest rate (see Figures 6.5 and 6.6).

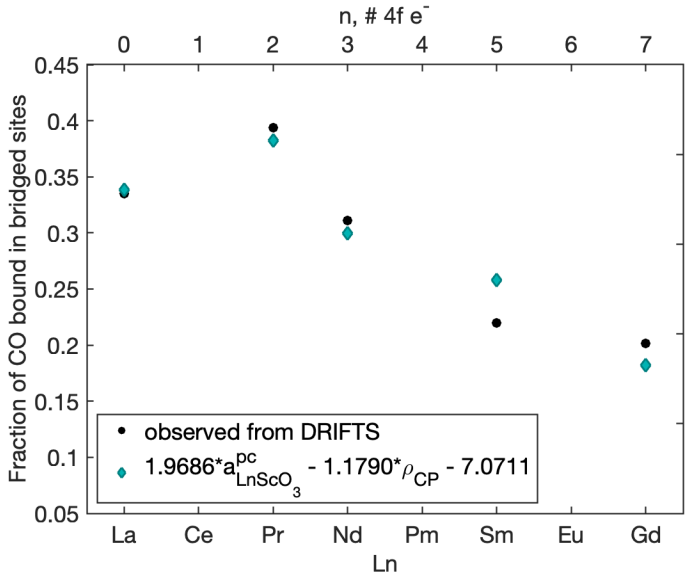

Figure 7.11. Quantitative estimation of the role of the pseudocubic lattice parameter of the $LnScO_3$ ($a^{pc}_{LnScO_3}$, Å) and the electron density at the Ln-O critical point (ρ_{CP}, e/Å^3) in CO adsorption. Black circles mark the fraction of CO bound to Pt/$LnScO_3$ at bridged sites as observed from DRIFTS; blue diamonds mark a linear combination of $a^{pc}_{LnScO_3}$ and ρ_{CP} minimized to closely approximate the experimental data.

7.6. Conclusions

The configuration of CO bound to $LnScO_3$-supported Pt has been characterized via DRIFTS. Strain induced in Pt by the support decreases monotonically with increasing lanthanide atomic number; however, both Pt/$PrScO_3$ and Pt/$NdScO_3$ yield more bridged CO sites than would be expected from strain alone. While the d-band theory of transition metals would predict that a greater tensile strain in Pt yields a greater fraction of CO binding linearly atop a single Pt atom, DRIFTS results indicate that strain is not the only factor determining whether CO binds to Pt in a linear or bridged configuration.

Instead, CO binding on Pt/$LnScO_3$ is found to be governed by a combination of strain and Ln–O bonding within the support. More ionic bonding between the lanthanide and oxygen in $LnScO_3$ enhances the electron donation capability of oxygen, inducing an effect where nearby oxygen atoms and the supported Pt metal have an enhanced ability to donate electrons for bond formation. Both $PrScO_3$ and $NdScO_3$ are found to have more ionic Ln–O bonds than the other $LnScO_3$ tested, accounting for their deviation from the monotonic trend that was previously expected from strain alone: Pr-O bonding is most ionic, then Nd-O, explaining why Pt/$PrScO_3$ and then Pt/$NdScO_3$ deviate the most from the expected trend. These results are also in agreement with those of Chapter 6, where the CO_2 binding strength was found to be greater in Pt/$PrScO_3$ and Pt/$NdScO_3$, resulting in faster rates of CO oxidation and RWGS over these two catalysts.

The lanthanide scandates share many properties, but electronic effects and strain induced in supported metals show different trends as the lanthanide is changed. These differences serve to isolate the two effects in observations across the support series, enabling us to elucidate that strain is not the only source of electronic effects of a support to impact CO chemisorption to the supported metal. With the combined impacts of strain and Ln 4f characterized for this system, the five Pt/$LnScO_3$ achieve the goal of providing a series of catalysts whose performance can be understood without many confounding variables. Trends in catalytic performance across this series can indicate the most important design parameters for catalyzing a reaction: linear trends will indicate the dominance of strain effects, while a non-monotonic trend that correlates with Ln–O bond ionicity (or proximity of Ln 4f states to the valence band edge) will indicate the dominance of the

Ln 4f inductive effect or electron donation capability of the catalyst surfaces. The lanthanide scandate series is thus demonstrated as an effective tool for monitoring isolated metal-support interactions.

CHAPTER 8

Summary and Future Directions

8.1. Conclusions

This dissertation has explored a two-line hydrosauna approach to synthesizing a series of lanthanide scandate nanoparticles which have been characterized in the context of heterogeneous catalysis. The hydrosauna method was developed by combining experimental and theoretical techniques to optimize the partial pressure of water vapor in an open environment. Such precise humidity control enabled generation of faceted high-purity (>96 mol%) $LnScO_3$ nanoparticles for multiple lanthanides (Ln = La, Pr, Nd, Sm, and Gd). Characterization of these particles revealed that while they all maintain the same *Pbnm* crystal structure and their lattice parameters decrease monotonically as the atomic number of the lanthanide increases, their chemical behavior does not change monotonically. Instead, they follow trends in properties governed by electronic structure such as CO_2 binding strength or metal-oxygen bond ionicity. Through a combination of experiment and computation, these trends can be predicted and utilized in interpreting behavior of catalysts supported on $LnScO_3$.

After deposition of noble metals Au and Pt on several $LnScO_3$ supports, the series of catalysts were characterized and tested in CO oxidation and the reverse water-gas shift reaction. Non-monotonic trends in catalytic behavior across the support series were found, indicating the importance of two competing factors: strain induced at the metal/support

interface by the different lattice parameter of each $LnScO_3$ support, which trends monotonically with increasing lanthanide atomic number; and electronic structure of each $LnScO_3$ support, which does not. Across the series tested herein, the non-monotonic activity of Ln 4f electrons from the support was found to be the dominant descriptor of metal/$LnScO_3$ catalytic performance. The thoroughly characterized similarities and differences among the $LnScO_3$ series enable us to use catalytic results to determine the dominant role of the support in each reaction, thus giving an indication of where to focus catalytic design.

8.2. Future Directions

The remainder of this chapter is dedicated to preliminary results and future work that I propose will further our understanding of hydrosauna synthesis, lanthanide scandates, and their potential as tools for catalyst design.

8.2.1. Using Water Vapor for $LnScO_3$ Morphological Control

While Chapter 4 establishes an optimal partial pressure of water vapor for hydrosauna synthesis of high-purity $LnScO_3$, the two-line reactor introduces another useful synthetic knob to turn: carrier gas flow rate. According to the results of Chapter 4, the optimal partial pressure of water vapor not only mitigates generation of unwanted hydroxide-containing phases, but also contributes to particle growth and faceting. The size and exposed facets of a catalyst or support significantly impact catalytic behavior, and are therefore important to control.[**7**] While the factor defining our upper limit of water concentration is the thermodynamically favored formation of LnOOH and $Ln(OH)_3$, our

lower limit is defined by crystallization of well-faceted $LnScO_3$ particles above a size we consider X-ray amorphous (see Figure 4.2). The precise water pressure tunability granted by the two-line hydrosauna will enable the elucidation of what really controls this lower limit. Because one can control the flow rate through both the water-saturated and bypass lines, there is not one unique means of obtaining the water vapor partial pressure that calculation tells us is optimal. Rather, the same partial pressure of water can be achieved by proportionally increasing or decreasing the flow rate to both lines simultaneously.

This reactor therefore enables the ability to control the overall flow rate while maintaining the optimal water vapor partial pressure—a feature that could improve our ability to further control $LnScO_3$ particle size and faceting. Consider for example the SE STEM images of $GdScO_3$ nanoparticles in Figure 8.1. Each sample was synthesized using the two-line hydrosauna method, and each synthesis was done under the same partial pressure of water vapor: 1.5 torr, the optimal value determined in Chapter 4. In Figure 8.1(a), this P_{H_2O} was obtained at a total gas flow rate (combination of dry and saturated Ar) of roughly 225 mL/min, resulting in $GdScO_3$ particles similar in shape and size to those produced in Chapter 4, averaging 40 nm wide across their shortest axis. In Figure 8.1(b), the same P_{H_2O} is achieved at 1.5 times the flow rate, nearly 340 mL/min. This higher-flow rate synthesis resulted in particles that appear much rounder and smaller, averaging only 7 nm across. Note that in both images, material that is backed by the TEM grid's lacy carbon shows more topographical contrast than areas of material backed by vacuum; this phenomenon indicates that crystalline $GdScO_3$ may be present in each case (see Chapter 3).

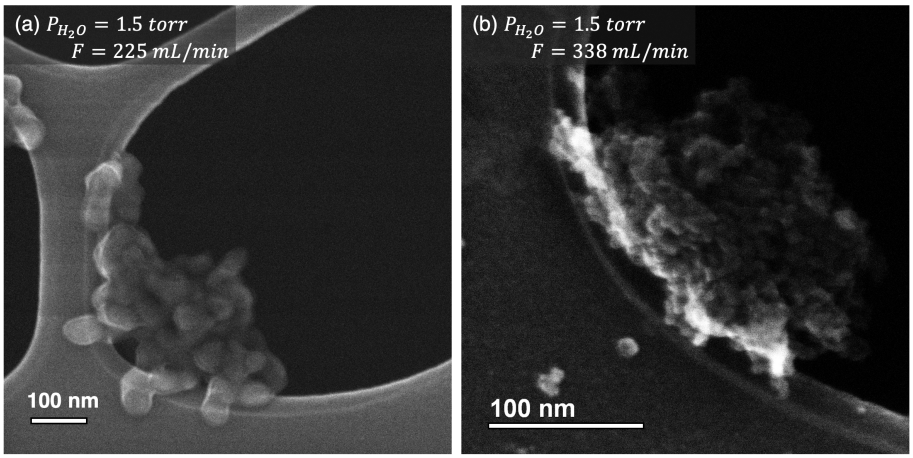

Figure 8.1. SE STEM images of $GdScO_3$ nanoparticles prepared via hydrosauna synthesis under the P_{H_2O} = 1.5 torr condition, obtained using two different carrier gas flow rates: (a) F = 225 mL/min and (b) F = 338 mL/min.

The same flow rate-based phenomenon was observed in the synthesis of $SmScO_3$, for which the calculated optimal P_{H_2O} is a higher 8.0 torr. For this experiment, PXRD was also used to confirm that the smaller, more rounded particles still had the $SmScO_3$ crystalline phase. These PXRD patterns are shown in Figure 8.2. Like the $GdScO_3$ syntheses represented in Figure 8.1, the powders depicted here were both obtained via two-line hydrosauna synthesis with the same P_{H_2O} = 8.0 torr obtained at two different overall flow rates. For the pattern in Figure 8.2(a), the usual 225 mL/min rate was used; for that in Figure 8.2(b), the flow rate was increased to 338 mL/min. Both syntheses yielded highly phase pure $SmScO_3$, with the faster flow rate yielding no hydroxide-containing phases at all despite having the same P_{H_2O}. There is noticeably more peak broadening present in Figure 8.2(b) than in (a)—a sign of crystallites that are smaller, though still the desired phase. To quantify this effect, the full width at half maximum (FWHM) of the tallest peak was measured at 0.35 for the slower-flow rate synthesis, and 0.52 for

the faster-flow rate synthesis. According to the Scherrer equation, which relates peak broadening to average crystalline domain size,[**63**] these FWHM values correspond to average crystallite sizes, τ, of 26.4 nm and 17.6 nm, respectively.

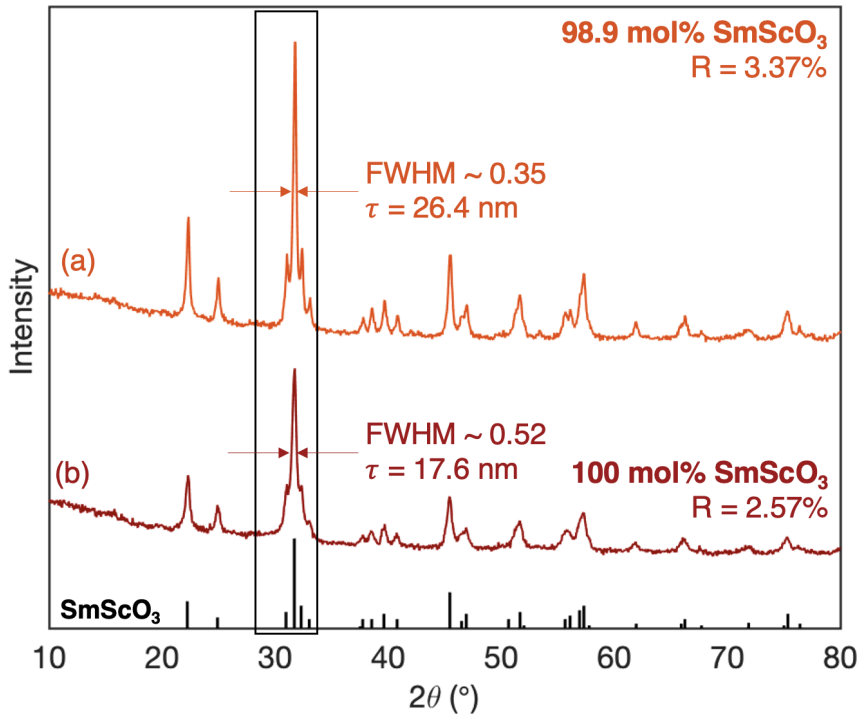

Figure 8.2. PXRD patterns of $SmScO_3$ nanoparticles prepared via hydrosauna synthesis under the P_{H_2O} = 8.0 torr condition obtained using two different carrier gas flow rates: (a) F = 225 mL/min and (b) F = 338 mL/min. The FWHM of the largest peak ($2\Theta = 32°$) of each diffraction pattern is labeled along with the corresponding average crystallite size, τ, which has been calculated according to the Scherrer equation.[**63**]

Because the $LnScO_3$ precursor gel itself contains water that contributes to the hydrosauna environment (see Chapters 3 and 4), the rate of change of the P_{H_2O} immediately surrounding the gel's surface seems to impact the crystal growth process. Like the wind chill factor that makes the air near one's skin feel colder than the true temperature on a

windy day, I hypothesize that a faster flow rate more quickly changes the local environment around the precursor gel. The gas closest to the gel's surface will spend less time in a saturated state if the carrier gas flow is more rapid. This effect may be studied in more detail by conducting hydrosauna synthesis of some $LnScO_3$ at its calculated optimal P_{H_2O} that is obtained via an array of different overall flow rates. While STEM and PXRD allow quick observation of approximate shape and particle size, higher-resolution (S)TEM, HREM, and diffraction should be used to characterize the particles' exposed facets.

These preliminary results point to a promising direction for future study by introducing another knob that can be turned in hydrosauna synthesis: one can potentially control particle morphology without compromising phase purity by maintaining an optimal P_{H_2O} while changing the overall gas flow rate. However, an understanding of how exactly the gel's environmental humidity affects $LnScO_3$ crystal nucleation and growth processes will require in-situ observation.

8.2.2. In-situ X-ray study of hydrosauna synthesis from $\mathbf{LnSc(OH)_6 \cdot xH_2O}$ precursor gel

Chapter 3 of this dissertation follows the process of discovering the importance of water vapor concentration in hydrosauna synthesis of $LnScO_3$, but while the effects of water vapor are understood, predicted, and utilized throughout this work, the exact role of water in $LnScO_3$ crystal nucleation and growth has not yet been determined. This understanding will require an in-situ hydrosauna study.

Thus far, two in-situ experiments have been conducted: Raman spectroscopy and XRD. The in-situ Raman spectroscopy experiment in Chapter 3 establish the ability to

detect water, hydroxides, and $LnScO_3$ via -OH and Ln-O bonds, serving to illustrate well a critical consideration in designing in-situ experiments for the $LnSc(OH)_6 \cdot xH_2O$ gel.

While further complicating factors of in-situ XRD hydrosauna experiments are highlighted in Appendix A, modifications of that experiment can be made to obtain meaningful information. XRD geometries that require transmittance through a capillary or reflectance from a stationary holder will not maintain the sample position as the $LnSc(OH)_6 \cdot xH_2O$ gel dehydrates and changes shape. A geometry that allows for a much larger sample bed, or more favorably a fluidized bed, could circumvent this issue. A fluidized bed would also help broaden the scope of in-situ Raman spectroscopy experiments; to reliably observe $LnScO_3$ crystallization from the gel via this method, one only needs to ensure the sample remains homogenous.

In addition, simply switching to a synchrotron source and using longer scans could help us glean some information from XRD. We have seen in Section 8.2.1 how even so-called X-ray amorphous material resulting from hydrosauna synthesis is still crystalline $LnScO_3$. However, with particles often smaller than a few nanometers, the peak broadening associated with nano-scale crystalline ordering causes a loss of information that is especially pronounced in Appendix A, where an Cu lab source is insufficient to resolve any XRD peaks in the gel. By using very high-energy X-rays (or neutrons[**225**]) one can achieve sufficient signal and resolution to calculate an atomic pair distribution function (PDF) to quantify interatomic distances in the material as it crystallizes.[**226**] The atomic PDF can be used to more quantitatively assess local nano-scale structure, including crystallinity and the presence of certain bonds (e.g. Ln-OH, Ln-O, Sc-O) or phases as a function of time throughout synthesis.

Beyond X-ray techniques, other in-situ methods are well suited to characterization of an amorphous gel as it crystallizes and will enable discovery beyond just the time-resolved presence of certain crystalline phases throughout synthesis. For example, while gel structure and diffusion processes inherently complicate the detection of nucleation events and growth mechanisms in a gel,[**227**] techniques such as holographic interferometry may be employed to gain a first-pass understanding of the properties of $LnSc(OH)_6 \cdot xH_2O$. This technique measures optical pathlength changes that occur in a variety of processes has long been used to measure diffusion patterns and growth rates in gels.[**228, 229**] However, because the crystals being produced are nanoscale, one would have to combine electron holography and interferometry[**230, 231**] with a suitable in-situ TEM holder to conduct this experiment in a hydrosauna environment. The environment would also have to be adjusted, increasing humidity to account for the small amount of material present; less gel provides less water on heating, and exposes a greater fraction of surface area to its surroundings. Obtaining meaningful results from such an experiment would be undoubtedly tricky, but very illuminating.

8.2.3. Extending the Lanthanide Scandate Series

The surface chemistry and catalytic trends demonstrated in this thesis would be further corroborated by the incorporation of more lanthanide scandates, extending the predicted trends to the rest of the lanthanide series. The lanthanides utilized thus far in $LnScO_3$ syntheses (La, Pr, Nd, Sm, and Gd) were chosen for simplicity. Each of these lanthanide cations is primarily stable in the 3+ oxidation state or can be purchased as a Ln^{3+} sesquioxide to use as starting material. There are a few lanthanides that can readily access

2+ or 4+ oxidation states, complicating the chemistry required to generate $LnScO_3$. For example, both europium (Eu) and ytterbium (Yb) exist in the 2+ state, as evidenced from their third ionization energies.[**232**] The Eu(II) and Yb(II) cations are stabilized by half-filled ($4f^7$) and filled ($4f^{14}$) orbitals, respectively. Meanwhile the fourth ionization energies of some lanthanides also indicate the presence of Ln(IV) cations. In particular cerium (Ce), terbium (Tb), and to a lesser extent praseodymium (Pr) frequently show the 4+ oxidation state, often presenting as LnO_2 or with a mix of Ln(III) and Ln(IV) as Ln_4O_7.[**232**] In the case of $PrScO_3$ synthesis in Chapter 4, this challenge was overcome by calcining the starting lanthanide oxide under hydrogen instead of argon or air. This approach enabled the synthesis of high-purity $PrScO_3$ whose PXRD pattern is depicted in Figure 4.7. Note the PrScO synthesis was the only one to present LnO_2 as an undesired phase, though less than 2 mol% PrO_2 was found in the sample.

Beyond oxidation state, one must also consider the stability of $LnScO_3$ given various sizes of A-site cation in the perovskite structure. This consideration is often summarized by use of the Goldschmidt tolerance factor, a perovskite formability factor that indicates the stability and distortion of perovskite crystal structures.[**233**] In the perovskite ABX_3, the Goldschmidt tolerance factor t is defined as:

$$t = \frac{r_A + r_X}{\sqrt{2}(r_B + r_X)}$$

where r_A, r_B, and r_X are the radii of the A, B, and X ions, respectively. For an undistorted cubic perovskite like STO, $t \sim 1$.[**234**] While there is some variation in the exact Goldschmidt tolerance factor values that cut off distinct perovskite regimes,[**235**] it is generally accepted that $t > 1$ yields a hexagonal structure, $0.8 < t < 0.9$ an orthorhombic

perovskite structure such as $LnScO_3$, and $t < 0.8$ some other structure, for example the trigonal ilmenite ($FeTiO_3$).[**236, 237, 238**] One study by Bartel et al. experimentally characterized various ABX_3 solids to determine that the parameter t predicts perovskite formability with about 75% accuracy.[**235**] This work is one of several to develop extended and more accurate perovskite formability tolerance factors based on the Goldschmidt factor, e.g. for halides,[**235**] hybrid organic-inorganic perovskites,[**239**] and two-dimensional Ruddlesden-Popper perovskites.[**240**]

Thus, while the predictive power of such parameters is not exact, the Goldschmidt tolerance factor is a useful starting tool for gauging approximate formability of an orthorhombic perovskite. The Goldschmidt tolerance factors for each $LnScO_3$, calculated from the Shannon radii,[**241**] are displayed in Table 8.1.

Estimating $t = 0.8$ as the lower bound for stability of the orthorhombic $LnScO_3$ phase, it becomes clear that $LnScO_3$ are less stable for Ln = Dy and smaller lanthanides. However, single crystals of many of these $LnScO_3$ have been made experimentally, including $DyScO_3$ and $TbScO_3$.[**242, 53**] Others including $HoScO_3$, $ErScO_3$, and $TmScO_3$ have been synthesized at high pressure, forming perovskite after an hour-long treatment at 20 kbar and 1000 °C.[**243**] The smallest lanthanide, Lu, can form $LuScO_3$ when stabilized via epitaxial growth on a substrate.[**244**] These perovskite scandates of the smaller lanthanides exist, but one requires more extreme conditions to stabilize them. This finding is succinctly summarized in a 2006 study by Christensen et al. in which the crystallization temperature of $LnScO_3$ was found to increase monotonically with increasing lanthanide atomic number and decreasing Goldschmidt tolerance factor of the perovskite.[**77**]

Table 8.1. Calculated Goldschmidt tolerance factors for all lanthanide scandate orthorhombic perovskites (except $PmScO_3$). Radii were taken from Shannon.[**241**] Values of $Sc^{3+}_{VI} = 0.885$ Å and $O^{2-} = 1.24$ Å were used.

	Goldschmidt tolerance factor	**Shannon ionic radius** Ln^{3+}_{VIII}[**241**]
$LaScO_3$	0.845	1.300
$PrScO_3$	0.834	1.266
$NdScO_3$	0.828	1.249
$SmScO_3$	0.818	1.219
$EuScO_3$	0.814	1.206
$GdScO_3$	0.810	1.193
$TbScO_3$	0.785	1.118
$DyScO_3$	0.801	1.167
$HoScO_3$	0.797	1.155
$ErScO_3$	0.793	1.144
$TmScO_3$	0.790	1.134
$YbScO_3$	0.787	1.125
$LuScO_3$	0.784	1.117

Challenges arise in extrapolating these results to hydrosauna synthesis. Since $LnScO_3$ of smaller lanthanides require higher temperatures, we must alter our approach to predicting the appropriate hydrosauna condition. Consider for example the case of dysprosium scandate, $DyScO_3$. In Section 4.4.2, DFT calculation predicted that 5 torr is optimal for hydrosauna synthesis of high-purity $DyScO_3$. Under that condition, following the established two-step procedure detailed in Chapter 4, only 45.2 mol% $DyScO_3$ was formed. As shown by the top pattern in Figure 8.3, most of the crystalline material resulting from this synthesis was simply the starting material Dy_2O_3. To produce high-purity $DyScO3_3$

the calcining temperature needed to be increased in accordance with predictions based on the Goldschmidt factor and literature reports. The control afforded by the two-line hydrosauna reactor enabled maintaining the optimal water vapor concentration while increasing the reaction temperature. The bottom diffraction pattern in Figure 8.3 shows a sample containing 98.4 mol% $DyScO_3$, which was obtained by increasing the first calcining step (T_1, referred to in Chapter 3 as the "nucleation step") of the synthesis from 450 °C to 515 °C. Small amounts of Dy_2O_3 and DyOOH make up the remaining 1.6 mol% of crystalline material identified in this sample.

The synthesis of $TbScO_3$ requires this adjustment for temperature while also introducing the lanthanide's accessibility to the 4+ oxidation state. In Chapter 4, Figure 4.6 illustrates that $TbScO_3$ synthesis is optimized under $P_{H_2O} = 8.5$ torr. PXRD results of the $TbScO_3$ synthesis conducted at this condition, shown here in Figure 8.4, indicate that this P_{H_2O} minimizes $Tb(OH)_3$ or TbOOH production, but the condition is not sufficient for phase pure material. Even storing and measuring Tb_2O_3 starting material in a glove box does not adequately prevent oxidation of Tb during synthesis. Because Tb readily exists in the 4+ state, there are many higher terbium oxide stoichiometries and structures,[**46, 100**] two of which make up the majority of material resulting from this first-pass $TbScO_3$ synthesis. These results can be seen in Figure 8.4, showing 98.9 mol% TbO_2 and 1.1 mol% Tb_4O_7.

Neither these higher lanthanide oxides nor smaller lanthanide cations should necessarily eliminate a lanthanide from consideration in our $LnScO_3$ nanoparticle series, however. I propose that smaller lanthanides such as Ho and Er can form $LnScO_3$ via the hydrosauna method if temperature is increased, so long as water concentration is maintained at the

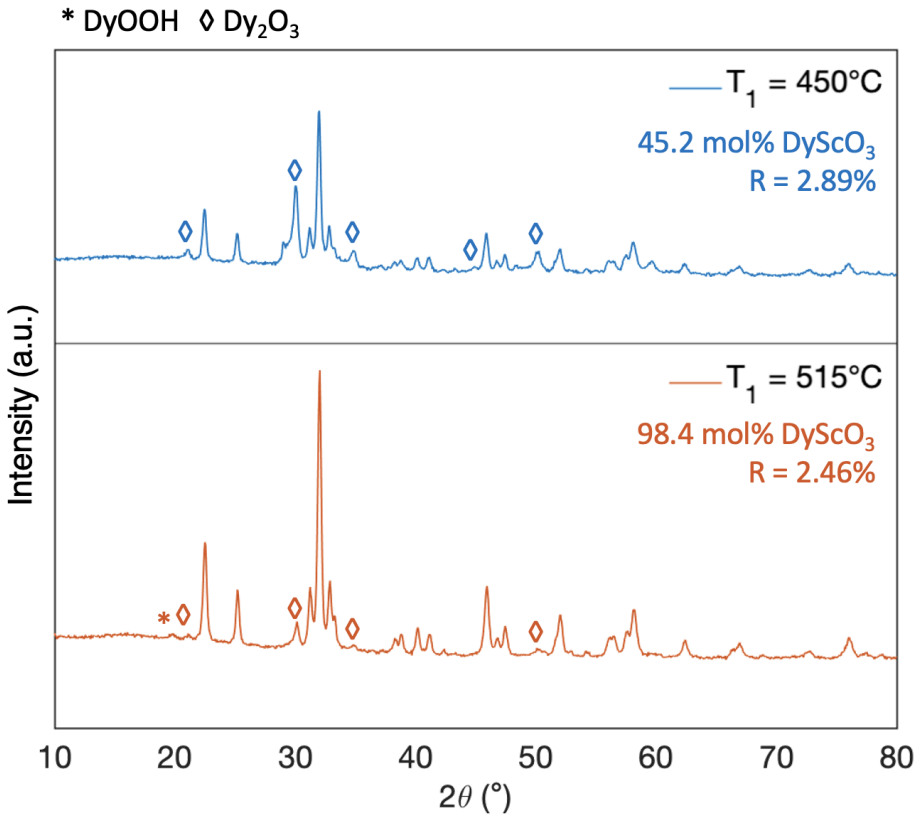

Figure 8.3. PXRD patterns showing results of hydrosauna $DyScO_3$ synthesis under $P_{H_2O} = 5$ torr utilizing two different nucleation temperatures: T_1 = 450°C (top, blue) and T_1 = 515 °C (bottom, red). Peaks contributed by minority phases are indicated with a symbol: DyOOH is indicated by an asterisk (*) and Dy_2O_3 is indicated by a diamond (◊).

new temperature as in the case of $DyScO_3$ synthesis. The lanthanides Ce and Tb, which access the 4+ oxidation state, may form $LnScO_3$ via hydrosauna synthesis if conducted in a reducing environment, e.g. using 5% H_2 in Ar as a carrier gas instead of pure Ar. The hydrosauna synthesis and characterization of additional $LnScO_3$ nanoparticles will allow us to broaden the series of $LnScO_3$. The patterns established thus far from the five lanthanides utilized in this dissertation (Ln = La, Pr, Nd, Sm, and Gd) can then be applied further, expanding the series and enabling corroboration of our predictions of

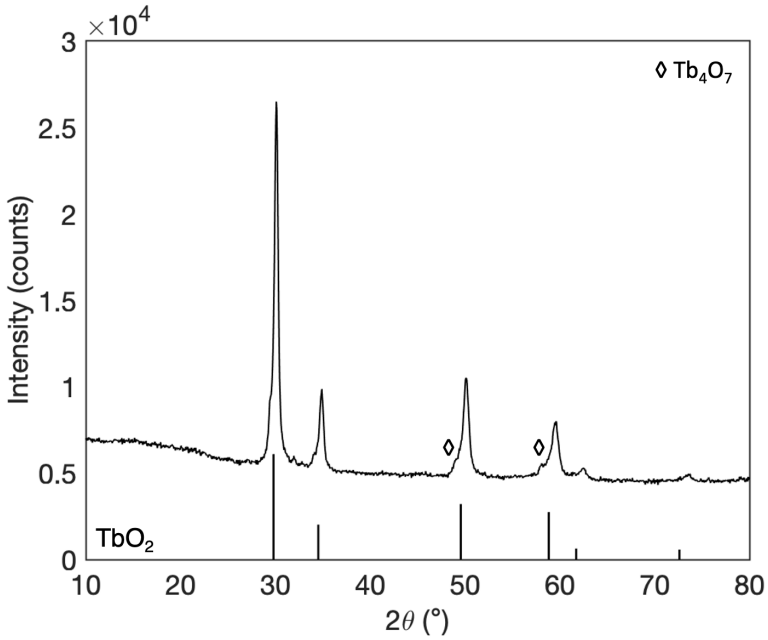

Figure 8.4. PXRD pattern of powder resulting from attempted $TbScO_3$ synthesis using predicted hydrosauna conditions. The pattern taken from Gruen et al.[**245**] at the bottom shows that the majority phase is not $TbScO_3$ but the higher terbium oxide, TbO_2. Peaks from Tb_4O_7 are indicated by diamonds (◊).

catalytic behavior based on calculation and characterization of the electronic structure of these additional $LnScO_3$ nanoparticles.

8.2.4. Using Lanthanide Scandates to Design Catalysts for Other Reactions

Throughout this dissertation, CO and CO_2 have been used as probe molecules. The desorption of CO_2 was used to quantify its binding strength to various $LnScO_3$ in Chapters 5 and 6, and the adsorption configuration of CO on strained Pt supported on $LnScO_3$ was observed in Chapter 7. Both results were interpreted in the context of $LnScO_3$-supported metal catalytic behavior for two reactions—CO oxidation and the RWGS reaction—that rely on CO_2, carbonate, or formate bonding. By choosing a different probe molecule,

one can gain more insight into other reactions that depend on different adsorbates. For example, methanol as a probe molecule can measure all types of active sites, rather than just those sites that donate electrons to bind a molecule like CO_2.

To date, many methods for measuring the number of surface active sites on a material are indirect; they rely on mechanisms that are complicated or not completely understood. For example, the number of surface active sites may need to be determined from a probe molecule different than the actual reactant being studied, or the type of site (Brønsted acid, base, or redox sites) may get confused. Using methanol chemisorption, one can directly gain a quantitative observation of the number of active sites, because methanol chemisorption re- quires a dissociative adsorption process that forms identifiable reactive surface intermediates depending on the adsorption site.[**246**]

Methanol oxidation reactions provide a direct approach to probing these active sites further, because the distribution of possible products is indicative of the type of active site required for its formation: basic sites will yield CO_2, acidic sites will yield dimethyl ether (owing to dehydration of the oxidized carbon species), and at redox sites, methanol will be dehydrogenated to form formaldehyde. This knowledge of active sites obtained from methanol chemisorption and oxidation will pave the way for broadening the scope of Pt/$LnScO_3$ to catalyze other reactions by allowing one to specify the number of active sites conducive to a certain type of adsorbate.

A good candidate for such a reaction is ethanol oxidation, which has a well-studied reaction mechanism.[**247, 248, 249**] Ethanol oxidation has applications in fuel cell and energy technologies[**250**] as well as in the production of the important chemical product acrolein.[**249**] In many of these reactions, as well as other alcohol oxidation reactions,

both acidic and basic sites play an important role,[**251, 252**] and so quantifying these characteristics on the support is necessary to design catalysts for these processes. As with CO_2 adsorption and CO oxidation, $LnScO_3$ and Pt/$LnScO_3$ can be studied in the context of ethanol oxidation. If the same trends in activation energy and rate of conversion are observed in ethanol oxidation as in CO oxidation, it may be inferred that surface basicity and the inductive effect are the dominant metal-support interaction forces in that context as well. This information will be useful in designing more efficient catalysts for ethanol oxidation and similar reactions in future.

8.2.5. Applying the Hydrosauna Method to Other Material Systems

The two-line hydrosauna reactor detailed in Chapter 4 was designed and calibrated for the needs of high-purity LnScO synthesis, but this humidity-controlled system may have other applications as well. Chapter 3 of this dissertation discusses how switching from a sealed autoclave-type hydrothermal synthesis to an open system hydrosauna synthesis enabled us to operate well below water's gas liquidus line. This switch allowed $LnScO_3$ synthesis to occur at atmospheric pressure and at significantly lower temperatures than are required by other methods.[**50**] I propose that for other complex oxides, the hydrosauna method (when combined with thermodynamic calculations) can provide a lower-temperature route to consistently phase-pure synthesis.

Beyond nanoparticle synthesis, the hydrosauna reactor can also be a route to altering the morphology or structure of prepared samples. The environment generated inside the reactor is similar to that used in the technique known as steaming, in which water vapor pressure is used to stabilize certain compounds like aluminosilicate zeolites.[**253**] Because

the crystalline frameworks of these materials are stable when exposed to water vapor but vulnerable to destruction at very high water pressures, the precise control afforded by the two-line hydrosauna reactor can provide an ideal environment for conducting zeolite research. One could also therefore finely tune the water vapor concentration in a steaming environment to, for example, suppress cation inversion in complex oxides.

In certain spinel AB_2O_4 structures, cation inversion or the presence of "anti-sites" (in which A and B atoms are interchanged) is thermodynamically stable.[**254**] This cation inversion has been shown to influence electronic structure, conductivity, and magnetic and optical properties of spinels.[**255, 256**] However, detailed studies of the nature of these impacts, particularly their dependence on the degree of inversion, λ, require synthetic control over λ. Through collaboration with inorganic chemist and collaborator R. Uppuluri, the one-line hydrosauna reactor approach has been used to synthesize $MgCrMnO_4$, a candidate cathode for high voltage Mg-ion batteries.[**257**] Figure 8.5 shows the PXRD pattern resulting from such a synthesis, in which a precursor gel is precipitated and then calcined in the hydrosauna environment at 450 °C for 24 hours. The result was high-purity $MgCrMnO_4$ with a relatively low degree of cationic inversion ($\lambda = 12.5\%$) compared to other hydrothermal methods such as urea co-precipitation. Further experimentation can elucidate how the P_{H_2O} and flow rate alter the parameter λ, and how this parameter affects electrochemical or other properties in a range of spinel applications.

Lastly, the hydrosauna reactor design may be applied to control precise small concentrations of a solvent other than water. For example, nanoparticles of the well-studied $SrTiO_3$ and $BaTiO_3$ have been shown to expose different facets when treated with different alcohol-based surfactant molecules.[**36**] A "solvosauna" reactor may be a scalable

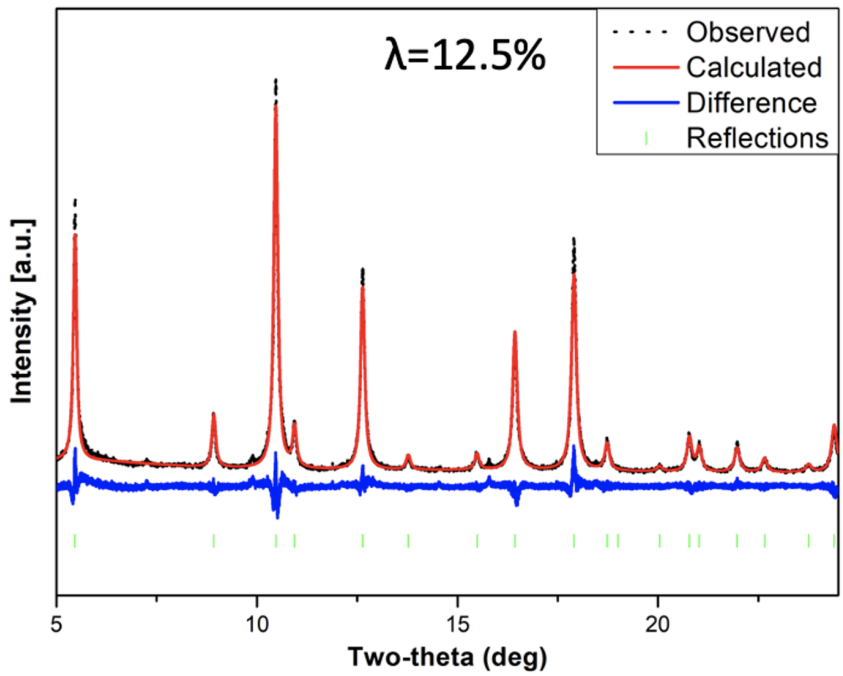

Figure 8.5. PXRD pattern and Rietveld refinement of high-purity $MgCrMnO_4$ made via hydrosauna synthesis. The degree of cationic inversion $\lambda = 12.5\%$ is lowered relative to $MgCrMnO_4$ synthesis via other methods. Synthesis and PXRD were done by R. Uppuluri using the hydrosauna reactor described in Section 3.2.

route to employing morphology-controlling treatments to nanoparticles near atmospheric pressure.

References

[1] J. A. Dumesic, G. W. Huber, and M. Boudart, *Handbook of Heterogeneous Catalysis*. Wiley-VCH Verlag GmbH & Co. KGaA, 2008.

[2] J. N. Armor, "A history of industrial catalysis," *Catalysis Today*, vol. 163, no. 1, pp. 3–9, 2011.

[3] M. A. Cook, D. H. Pack, and A. G. Oblad, "Structural model of low pressure "physical" adsorption," *The Journal of Chemical Physics*, vol. 19, no. 3, pp. 367–376, 1951.

[4] S. J. Tauster, S. C. Fung, and R. L. Garten, "Strong metal-support interactions. Group 8 noble metals supported on titanium dioxide," *Journal of the American Chemical Society*, vol. 100, no. 1, pp. 170–175, 1978.

[5] G. C. Bond, "Supported metal catalysts: some unsolved problems," *Chemical Society Reviews*, vol. 20, no. 4, p. 441, 1991.

[6] G. C. Bond, "Strategy of research on supported metal catalysts. problems of structure-sensitive reactions in the gas phase," *Accounts of Chemical Research*, vol. 26, no. 9, pp. 490–495, 1993.

[7] M. Che and C. O. Bennett, "The influence of particle size on the catalytic properties of supported metals," *Advances in Catalysis*, vol. 36, pp. 55–172, 1989.

[8] K. Hayek, R. Kramer, and Z. Paal, "Metal-support boundary sites in catalysis," *Applied Catalysis*, vol. 162, pp. 1–15, 1997.

[9] M. Cargnello, V. V. T. Doan-Nguyen, T. R. Gordon, R. E. Diaz, E. A. Stach, R. J. Gorte, P. Fornasiero, and C. B. Murray, "Control of metal nanocrystal size reveals metal-support interface role for ceria catalysts," *Science*, vol. 341, no. 6147, pp. 771–773, 2013.

[10] N. Masoud, L. Delannoy, H. Schaink, A. Van Der Eerden, J. W. De Rijk, T. A. G. Silva, D. Banerjee, J. D. Meeldijk, K. P. De Jong, C. Louis, and P. E. De Jongh,

"Superior stability of Au/SiO_2 compared to Au/TiO_2 catalysts for the selective hydrogenation of butadiene," *ACS Catalysis*, vol. 7, no. 9, pp. 5594–5603, 2017.

[11] D. B. Williams and C. B. Carter, *Transmission Electron Microscopy: A Textbook for Materials Science*. New York: Springer, 2nd ed., 2009.

[12] J. Weitkamp, "Zeolites and catalysis," *Solid State Ionics*, vol. 131, pp. 175–188, 2000.

[13] H. Xu and P. Wu, "Two-dimensional zeolites in catalysis: current state-of-the-art and perspectives," *Catalysis Reviews*, vol. 63, pp. 234–301, 2021.

[14] A. Taguchi and F. Schüth, "Ordered mesoporous materials in catalysis," *Microporous and Mesoporous Materials*, vol. 77, pp. 1–45, 2005.

[15] P. L. J. Gunter and J. W. H. Niemantsverdriet, "Surface science approach to modeling supported catalysts," *Catalysis Reviews*, vol. 39, pp. 77–168, 1997.

[16] J. A. Enterkin, K. R. Poeppelmeier, and L. D. Marks, "Oriented catalytic platinum nanoparticles on high surface area strontium titanate nanocuboids," *Nano Lett*, vol. 11, no. 3, pp. 993–7, 2011.

[17] G. Z. Wulff, "XXV. Zur Frage der Geschwindigkeit des Wachsthums und der Auflösung der Krystallflächen," *Krystallogr. Mineral.*, vol. 34, pp. 449–530, 1901.

[18] W. L. Winterbottom, "Equilibrium shape of a small particle in contact with a foreign substrate," *Acta Metallurgica*, vol. 15, no. 2, pp. 303–310, 1967.

[19] L. D. Marks and D. J. Smith, "Direct surface imaging in small metal particles," *Nature*, vol. 303, pp. 316–217, 1983.

[20] L. D. Marks, "Surface structure and energetics of multiply twinned particles," *Philosophical Magazine A*, vol. 49, no. 1, pp. 81–93, 1984.

[21] M. Sankar, Q. He, R. V. Engel, M. A. Sainna, A. J. Logsdail, A. Roldan, D. J. Willock, N. Agarwal, C. J. Kiely, and G. J. Hutchings, "Role of the support in gold-containing nanoparticles as heterogeneous catalysts," *Chem Rev*, vol. 120, no. 8, pp. 3890–3938, 2020.

[22] Z. Zhang and J. John T. Yates, "Band bending in semiconductors: Chemical and physical consequences at surfaces and interfaces," *Chem Rev*, vol. 112, no. 10, pp. 5520–5551, 2012.

[23] J. A. Enterkin, R. M. Kennedy, J. Lu, J. W. Elam, R. E. Cook, L. D. Marks, P. C. Stair, C. L. Marshall, and K. R. Poeppelmeier, "Epitaxial stabilization of face selective catalysts," *Topics in Catalysis*, vol. 56, no. 18-20, pp. 1829–1834, 2013.

[24] K. Fujiwara, K. Okuyama, and S. E. Pratsinis, "Metal–support interactions in catalysts for environmental remediation," *Environmental Science: Nano*, vol. 4, pp. 2076–2092, 2017.

[25] T. W. Van Deelen, C. Hernández Mejía, and K. P. De Jong, "Control of metal-support interactions in heterogeneous catalysts to enhance activity and selectivity," *Nature Catalysis*, vol. 2, pp. 955–970, 2019.

[26] Y. Lou, J. Xu, Y. Zhang, C. Pan, Y. Dong, and Y. Zhu, "Metal-support interaction for heterogeneous catalysis: from nanoparticles to single atoms," *Materials Today Nano*, vol. 12, p. 100093, 2020.

[27] Y. Li, Y. Zhang, K. Qian, and W. Huang, "Metal–support interactions in metal/oxide catalysts and oxide–metal interactions in oxide/metal inverse catalysts.," *ACS Catalysis*, vol. 12, pp. 1268–1287, 2022.

[28] K. Yan, T. A. Maark, A. Khorshidi, V. A. Sethuraman, A. A. Peterson, and P. R. Guduru, "The influence of elastic strain on catalytic activity in the hydrogen evolution reaction," *Angew Chem Int Ed Engl*, vol. 55, no. 21, pp. 6175–81, 2016.

[29] N. Lu, X. Wang, Z. Suo, and J. Vlassak, "Failure by simultaneous grain growth, strain localization, and interface debonding in metal films on polymer substrates," *Journal of Materials Research*, vol. 24, pp. 379–385, 2009.

[30] A. Schlapka, M. Lischka, A. Gross, U. Kasberger, and P. Jakob, "Surface strain versus substrate interaction in heteroepitaxial metal layers: Pt on Ru(0001)," *Phys Rev Lett*, vol. 91, no. 1, p. 016101, 2003.

[31] B.-R. Chen, L. A. Crosby, C. George, R. M. Kennedy, N. M. Schweitzer, J. Wen, R. P. Van Duyne, P. C. Stair, K. R. Poeppelmeier, L. D. Marks, and M. J. Bedzyk, "Morphology and CO oxidation activity of Pd nanoparticles on $SrTiO_3$ nanopolyhedra," *ACS Catalysis*, vol. 8, no. 6, pp. 4751–4760, 2018.

[32] J. A. Enterkin, W. Setthapun, J. W. Elam, S. T. Christensen, F. A. Rabuffetti, L. D. Marks, P. C. Stair, K. R. Poeppelmeier, and C. L. Marshall, "Propane oxidation over Pt/$SrTiO_3$ nanocuboids," *ACS Catalysis*, vol. 1, pp. 629–635, 2011.

[33] G. Celik, R. M. Kennedy, R. A. Hackler, M. Ferrandon, A. Tennakoon, S. Patnaik, A. M. LaPointe, S. C. Ammal, A. Heyden, F. A. Perras, M. Pruski, S. L. Scott, K. R.

Poeppelmeier, A. D. Sadow, and M. Delferro, "Upcycling single-use polyethylene into high-quality liquid products," *ACS Cent Sci*, vol. 5, no. 11, pp. 1795–1803, 2019.

[34] I. L. Peczak, R. M. Kennedy, R. A. Hackler, B. Lee, M. Meirow, E. Luijten, K. R. Poeppelmeier, and M. Delferro, "Treasuring trash: Pt/$SrTiO_3$ catalysts process plastic waste into high-value materials," *Matter*, pp. 1–26, 2023.

[35] N. Erdman, K. R. Poeppelmeier, M. Asta, O. Warschkow, D. E. Ellis, and L. D. Marks, "The structure and chemistry of the TiO2-rich surface of SrTiO3 (001)," *Nature*, vol. 419, pp. 55–58, 2002.

[36] L. Dong, H. Shi, K. Cheng, Q. Wang, W. Weng, and W. Han, "Shape-controlled growth of SrTiO3 polyhedral submicro/nanocrystals," *Nano Research*, vol. 7, no. 9, pp. 1311–1318, 2014.

[37] G. S. Foo, Z. D. Hood, and Z. L. Wu, "Shape effect undermined by surface reconstruction: Ethanol dehydrogenation over shape-controlled SrTiO3 nanocrystals," *ACS Catalysis*, vol. 8, no. 1, pp. 555–565, 2018.

[38] N. Erdman and L. D. Marks, "$SrTiO_3$(001) surface structures under oxidizing conditions," *Surface Science*, vol. 526, pp. 107–114, 2003.

[39] J. B. Goodenough, "Electronic and ionic transport propertiesand other physical aspects of perovskites," *Rep. Prog. Phys.*, vol. 67, pp. 1915–1993, 2004.

[40] T. Shi, Y. Chen, and X. Guo, "Defect chemistry of alkaline earth metal (Sr/Ba) titanates," *Progress in Materials Science*, vol. 80, pp. 77–132, 2016.

[41] J. N. Baker, P. C. Bowes, J. S. Harris, and D. L. Irving, "Mechanisms governing metal vacancy formation in $BaTiO_3$ and $SrTiO_3$," *Journal of Applied Physics*, vol. 124, no. 11, 2018.

[42] K. Uchino, E. Sadanaga, and T. Hirose, "Dependence of the crystal structure on particle size in barium titanate," *Journal of the American Ceramic Society*, vol. 72, no. 8, pp. 1555–1558, 1989.

[43] H. D. Lutz, W. Eckers, G. Schneider, and H. Hauseler, "Raman and infrared spectra of barium and strontium hydroxides and hydroxide hydrates," *Spectrochimica Acta*, vol. 37A, no. 7, pp. 561–567, 1981.

[44] M. M. Vijatovic, J. D. Bobic, and B. D. Stojanovic, "History and challenges of barium titanate: Part I," *Science of Sintering*, vol. 40, no. 2, pp. 155–165, 2008.

[45] M. Mostafa, Z. A. Alrowaili, M. A. Shehri, M. Mobarak, and A. M. Abbas, "Structural and optical properties of calcium titanate prepared from gypsum," *Journal of Nanotechnology*, vol. 2022, 2022.

[46] W. H. Wells, Jr. and V. L. Wells, *The Lanthanides, Rare Earth Elements*, pp. 817–840. John Wiley & Sons, Inc., sixth ed., 2012.

[47] G. Tessitore, G. A. Mandl, S. L. Maurizio, M. Kaur, and J. A. Capobianco, "The role of lanthanide luminescence in advancing technology," *RSC Adv*, vol. 13, no. 26, pp. 17787–17811, 2023.

[48] M. J. Polinski, D. J. Grant, S. Wang, E. V. Alekseev, J. N. Cross, E. M. Villa, W. Depmeier, L. Gagliardi, and T. E. Albrecht-Schmitt, "Differentiating between trivalent lanthanides and actinides," *J Am Chem Soc*, vol. 134, no. 25, pp. 10682–92, 2012.

[49] X. Yin, Y. Wang, X. Bai, Y. Wang, L. Chen, C. Xiao, J. Diwu, S. Du, Z. Chai, T. E. Albrecht-Schmitt, and S. Wang, "Rare earth separations by selective borate crystallization," *Nat Commun*, vol. 8, p. 14438, 2017.

[50] R. P. Liferovich and R. H. Mitchell, "A structural study of ternary lanthanide orthoscandate perovskites," *Journal of Solid State Chemistry*, vol. 177, no. 6, pp. 2188–2197, 2004.

[51] G. B. Jin, E. S. Choi, and T. E. Albrecht-Schmitt, "Syntheses, structures, magnetism, and optical properties of gadolinium scandium chalcogenides," *Journal of Solid State Chemistry*, vol. 182, no. 5, pp. 1075–1081, 2009.

[52] Z. R. Mansley, C. A. Mizzi, P. Koirala, J. Wen, and L. D. Marks, "Structure of the (110) $LnScO_3$ (Ln = Gd, Tb, Dy) surfaces," *Physical Review Materials*, vol. 4, p. 045003, 2020.

[53] R. Uecker, B. Velickov, D. Klimm, R. Bertram, M. Bernhagen, M. Rabe, M. Albrecht, R. Fornari, and D. G. Schlom, "Properties of rare-earth scandate single crystals (Re=Nd-Dy)," *Journal of Crystal Growth*, vol. 310, no. 10, pp. 2649–2658, 2008.

[54] M. Raekers, K. Kuepper, S. Bartkowski, M. Prinz, A. V. Postnikov, K. Potzger, S. Zhou, A. Arulraj, N. Stüßer, R. Uecker, W. L. Yang, and M. Neumann, "Electronic and magnetic structure of $RScO_3$(R=Sm,Gd,Dy) from X-ray spectroscopies and first-principles calculations," *Physical Review B*, vol. 79, no. 12, 2009.

[55] D. G. Schlom and J. H. Haeni, "A thermodynamic approach to selecting alternative gate dielectrics," *MRS Bulletin*, vol. 27, no. 3, pp. 198–204, 2002.

[56] R. J. Paull, *Lanthanide Scandate Supported Noble Metal Nanoparticle Catalysis*. Thesis, Northwestern University, 2020.

[57] I. N. Leontyev, A. B. Kuriganova, N. G. Leontyev, L. Hennet, A. Rakhmatullin, N. V. Smirnova, and V. Dmitriev, "Size dependence of the lattice parameters of carbon supported platinum nanoparticles: X-ray diffraction analysis and theoretical considerations," *RSC Adv*, vol. 4, pp. 35959–25965, 2014.

[58] Z. R. Mansley, R. J. Paull, E. P. Greenstein, J. G. Wen, K. R. Poeppelmeier, and L. D. Marks, "ScO_x-rich surface terminations on lanthanide scandate nanoparticles," *Physical Review Materials*, vol. 5, no. 12, 2021.

[59] Z. R. Mansley, R. J. Paull, L. Savereide, S. Tatro, E. P. Greenstein, A. Gosavi, E. Cheng, J. Wen, K. R. Poeppelmeier, J. M. Notestein, and L. D. Marks, "Identifying support effects in Au-catalyzed CO oxidation," *ACS Catalysis*, vol. 11, no. 19, pp. 11921–11928, 2021.

[60] R. J. Paull, T. Ly, Z. R. Mansley, K. R. Poeppelmeier, and L. D. Marks, "Controlled two-step formation of faceted perovskite rare-earth scandate nanoparticles," *Crystals*, vol. 9, no. 4, 2019.

[61] C. A. Mizzi, P. Koirala, and L. D. Marks, "Electronic structure of lanthanide scandates," *Physical Review Materials*, vol. 2, no. 2, 2018.

[62] H. M. Rietveld, "A profile refinement method for nuclear and magnetic structures," *Journal of Applied Crystallography*, vol. 2, pp. 65–71, 1969.

[63] J. I. Langford and J. C. Wilson, "Scherrer after Sixty Years: A Survey and Some New Results in the Determination of Crystallite Size," *J. Appl. Cryst.*, vol. 11, pp. 102–113, 1978.

[64] "MDI Jade." Materials Data: Livermore, CA, 2019.

[65] H. Seiler, "Secondary electron emission in the scanning electron microscope," *Journal of Applied Physics*, vol. 54, no. 11, pp. R1–R18, 1983.

[66] L. D. M. Voyles and P. M., "When is Z-contrast D-contrast?," *Microscopy Today*, vol. 22, no. 1, p. 65, 2014.

[67] J. M. Cowley and A. F. Moodie, "The scattering of electrons by atoms and crystals. I. A new theoretical approach," *Acta Crystallogr*, vol. 10, pp. 609–619, 1957.

[68] T. Suntola and J. Hyvarinen, "Atomic layer epitaxy," *Annu. Rev. Mater. Sci.*, vol. 15, pp. 177–195, 1985.

[69] J. W. Elam, A. V. V. Zinovev, M. J. Pellin, D. J. Comstock, and M. C. Hersam, "Nucleation and growth of noble metals on oxide surfaces using atomic layer deposition," *ECS Transactions*, vol. 3, pp. 271–278, 2007.

[70] C. Wang, L. Hu, Y. Lin, K. Poeppelmeier, P. Stair, and L. Marks, "Controllable ALD synthesis of platinum nanoparticles by tuning different synthesis parameters," *Journal of Physics D: Applied Physics*, vol. 50, no. 41, 2017.

[71] W. Kohn and P. Hohenberg, "Inhomogenous electron gas," *Physical Review B*, vol. 136, pp. 864–871, 1964.

[72] W. Kohn and L. J. Sham, "Self-consistent equations including exchange and correlation," *Physical Review*, vol. 140, pp. A1133–A1138, 1965.

[73] P. Blaha, K. Schwarz, F. Tran, R. Laskowski, G. K. H. Madsen, and L. D. Marks, "WIEN2k: An APW+lo program for calculating the properties of solids," *Journal of Chemical Physics*, vol. 157, no. 7, p. 74101CODEN: JCPSA6, 2020.

[74] J. P. Perdew, A. Ruzsinszky, G. I. Csonka, O. A. Vydrov, G. E. Scuseria, L. A. Constantin, X. Zhou, and K. Burke, "Restoring the density-gradient expansion for exchange in solids and surfaces," *Phys Rev Lett*, vol. 100, no. 13, p. 136406, 2008.

[75] P. Novák, J. Kuneš, L. Chaput, and W. E. Pickett, "Exact exchange for correlated electrons," *physica status solidi (b)*, vol. 243, no. 3, pp. 563–572, 2006.

[76] P. Myllymäki, M. Roeckerath, J. M. Lopes, J. Schubert, K. Mizohata, M. Putkonen, and L. Niinistö, "Rare earth scandate thin films by atomic layer deposition: effect of the rare earth cation size," *Journal of Materials Chemistry*, vol. 20, no. 20, 2010.

[77] H. M. Christen, G. E. Jellison Jr., I. Ohkubo, S. Huang, M. E. Reeves, E. Cicerrella, J. L. Freeouf, Y. Jia, and D. G. Schlom, "Dielectric and optical properties of epitaxial rare-earth scandate films and their crystallization behavior," *Applied Physics Letters*, vol. 88, p. 262906, 2006.

[78] R. J. Paull, Z. R. Mansley, T. Ly, L. D. Marks, and K. R. Poeppelmeier, "Synthesis of gadolinium scandate from a hydroxide hydrogel," *Inorg Chem*, vol. 57, no. 7, pp. 4104–4108, 2018.

[79] J. Bourassa, A. Ramm, J. Q. Feng, and M. J. Renn, "Water vapor-assisted sintering of silver nanoparticle inks for printed electronics," *SN Applied Sciences*, vol. 1, 2019.

[80] T. Kozawa, K. Yanagisawa, and Y. Suzuki, "Water vapor-assisted solid-state reaction for the synthesis of nanocrystalline $BaZrO_3$ powder," *Journal of the American Ceramic Society of Japan*, vol. 121, no. 3, pp. 308–312, 2013.

[81] P. Wang, T. Xie, L. Peng, H. Li, T. Wu, S. Pang, and D. Wang, "Water-assisted synthesis of anatase TiO2 nanocrystals: Mechanism and sensing properties to oxygen at room temperature," *J. Phys. Chem. C*, vol. 112, pp. 6648–6652, 2008.

[82] T. Ly, J. Wen, and L. D. Marks, "Kinetic growth regimes of hydrothermally synthesized potassium tantalate nanoparticles," *Nano Lett*, vol. 18, no. 8, pp. 5186–5191, 2018.

[83] B. Veličkov, V. Kahlenberg, R. Bertram, and M. Bernhagen, "Crystal chemistry of $GdScO_3$, $DyScO_3$, $SmScO_3$ and $NdScO_3$," *Zeitschrift für Kristallographie*, vol. 222, no. 9, pp. 466–473, 2007.

[84] M. Hada and J. Matsuo, "Ultrafast X-ray sources for time-resolved measurements," *X-Ray Spectrometry*, vol. 41, no. 4, pp. 188–194, 2012.

[85] J. E. Jørgensen, T. R. Jensen, and J. C. Hanson, "Hydrothermal synthesis of nanocrystalline ZnSe: An in situ synchrotron radiation X-ray powder diffraction study," *Journal of Solid State Chemistry*, vol. 181, no. 8, pp. 1925–1929, 2008.

[86] W.-C. Ko, Y.-H. Hsu, S.-C. Weng, C.-K. Chang, M.-T. Lee, W.-T. Chuang, H.-C. Thong, M. Ali, and E. W. Huang, "Using in-situ synchrotron x-ray diffraction to investigate phase transformation and lattice relaxation of a three-way piezophototronic soft material," *Semiconductor Science and Technology*, vol. 32, no. 7, 2017.

[87] S. Zhang, J. Hwang, K. Matsumoto, and R. Hagiwara, "In situ orthorhombic to amorphous phase transition of Nb_2O_5 and its temperature effect on pseudocapacitive behavior," *ACS Appl Mater Interfaces*, vol. 14, no. 17, pp. 19426–19436, 2022.

[88] A. K. Cheetham and C. F. Mellot, "In situ studies of the sol-gel synthesis of materials," *Chem. Mater.*, vol. 9, pp. 2269–2279, 1997.

[89] E. Stampler, W. Sheets, W. Prellier, T. Marks, and K. Poeppelmeier, "Hydrothermal synthesis of $LnMnO_3$ (Ln = Ho–Lu and Y): exploiting amphoterism in late rare-earth oxides," *Journal of Materials Chemistry*, vol. 19, p. 4375, 2009.

[90] J. Kreisel, S. Pignard, H. Vincent, J. P. Sénateur, and G. Lucazeau, "Raman study of $BaFe_{12}O_{19}$ thin films," *Applied Physics Letters*, vol. 73, no. 9, pp. 1194–1196, 1998.

[91] O. Chaix-Pluchery and J. Kreisel, "Raman scattering of perovskite $DyScO_3$ and $GdScO_3$ single crystals," *J Phys Condens Matter*, vol. 21, no. 17, p. 175901, 2009.

[92] O. Chaix-Pluchery and J. Kreisel, "Raman scattering of perovskite SmScO3 and NdScO3 single crystals," *Phase Transitions*, vol. 84, pp. 542–554, 2011.

[93] J. A. Darr, J. Zhang, N. M. Makwana, and X. Weng, "Continuous hydrothermal synthesis of inorganic nanoparticles: Applications and future directions," *Chem Rev*, vol. 117, no. 17, pp. 11125–11238, 2017.

[94] G. Canu and V. Buscaglia, "Hydrothermal synthesis of strontium titanate: thermodynamic considerations, morphology control and crystallisation mechanisms," *CrystEngComm*, vol. 19, no. 28, pp. 3867–3891, 2017.

[95] F. A. Rabuffetti, H.-S. Kim, J. A. Enterkin, Y. Wang, C. H. Lanier, L. D. Marks, K. R. Poeppelmeier, and P. C. Stair, "Synthesis-Dependent First-Order Raman Scattering in $SrTiO_3$ Nanocubes at Room Temperature," *Chemistry of Materials*, vol. 20, no. 17, p. 5628– 5635, 2008.

[96] L. N. Walters, E. L. Wang, and J. M. Rondinelli, "Thermodynamic descriptors to predict oxide formation in aqueous solutions," *J Phys Chem Lett*, vol. 13, no. 26, pp. 6236–6243, 2022.

[97] M. M. Lencka and R. E. Riman, "Thermodynamic modeling of hydrothermal synthesis of ceramic powders," *Chemistry of Materials*, vol. 5, no. 1, pp. 61–70, 1993.

[98] A. Talapatra, B. P. Uberuaga, C. R. Stanek, and G. Pilania, "A machine learning approach for the prediction of formability and thermodynamic stability of single and double perovskite oxides," *Chemistry of Materials*, vol. 33, no. 3, pp. 845–858, 2021.

[99] P. Raccuglia, K. C. Elbert, P. D. Adler, C. Falk, M. B. Wenny, A. Mollo, M. Zeller, S. A. Friedler, J. Schrier, and A. J. Norquist, "Machine-learning-assisted materials discovery using failed experiments," *Nature*, vol. 533, no. 7601, pp. 73–6, 2016.

[100] G. Adachi, N. Imanaka, and Z. C. Kang, eds., *Binary Rare Earth Oxides*. Dordrecht: Kluwer Academic, 2004.

[101] K. P. Marshall, A. B. Blichfeld, S. L. Skjaervo, O. G. Grendal, W. van Beek, S. M. Selbach, T. Grande, and M. A. Einarsrud, "A Fast, Low-Temperature Synthesis Method for Hexagonal $YMnO_3$: Kinetics, Purity, Size and Shape as Studied by In Situ X-ray Diffraction," *Chemistry*, vol. 26, no. 42, pp. 9330–9337, 2020.

[102] M. W. Shafer and R. Roy, "Rare-earth polymorphism and phase equilibria in rare-earth oxide-water systems," *Journal of the American Ceramic Society*, vol. 42, pp. 563–570, 1959.

[103] N. C. Jeong, J. S. Lee, E. L. Tae, Y. J. Lee, and K. B. Yoon, "Acidity scale for metal oxides and Sanderson's electronegativities of lanthanide elements," *Angew Chem Int Ed Engl*, vol. 47, no. 52, pp. 10128–32, 2008.

[104] O. C. Gagne and F. C. Hawthorne, "Empirical Lewis acid strengths for 135 cations bonded to oxygen," *Acta Crystallogr B Struct Sci Cryst Eng Mater*, vol. 73, no. Pt 5, pp. 956–961, 2017.

[105] R. T. Haasch, E. Breckenfeld, and L. W. Martin, "An introduction to single crystal perovskites and single crystal rare-earth scandate perovskites analyzed using X-ray photoelectron spectroscopy," *Surface Science Spectra*, vol. 21, no. 1, pp. 84–86, 2014.

[106] Y. Zhang, "Electronegativities of elements in valence states and their applications. 1. electronegativities of elements in valence states," *Inorg Chem*, vol. 21, no. 11, pp. 3886–3889, 1982.

[107] E. P. Greenstein, K. R. Poeppelmeier, and L. D. Marks, "Wet to dry controls lanthanide scandate synthesis," *Inorg Chem*, vol. 62, no. 12, pp. 4853–4860, 2023.

[108] R. T. Haasch, L. W. Martin, and E. Breckenfeld, "Single crystal rare-earth scandate perovskites analyzed using X-ray photoelectron spectroscopy: 1. PrScO3(110)," *Surface Science Spectra*, vol. 21, no. 1, pp. 131–139, 2014.

[109] R. T. Haasch, L. W. Martin, and E. Breckenfeld, "Single crystal rare-earth scandate perovskites analyzed using X-ray photoelectron spectroscopy: 2. NdScO3(110)," *Surface Science Spectra*, vol. 21, no. 1, pp. 140–148, 2014.

[110] R. T. Haasch, L. W. Martin, and E. Breckenfeld, "Single crystal rare-earth scandate perovskites analyzed using X-ray photoelectron spectroscopy: 3. GdScO3(110)," *Surface Science Spectra*, vol. 21, no. 1, pp. 149–156, 2014.

[111] F. A. Stevie and C. L. Donley, "Introduction to X-ray photoelectron spectroscopy," *Journal of Vacuum Science & Technology A*, vol. 38, no. 6, 2020.

[112] R. T. Haasch, L. W. Martin, and E. Breckenfeld, "Single crystal rare-earth scandate perovskites analyzed using X-ray photoelectron spectroscopy: 4. TbScO3(110)," *Surface Science Spectra*, vol. 21, no. 1, pp. 157–164, 2014.

[113] F. A. Stevie and C. L. Donley, "Introduction to x-ray photoelectron spectroscopy," *Journal of Vacuum Science & Technology A*, vol. 38, no. 6, 2020.

[114] J. J. Yeh and I. Lindau, "Atomic subshell photoionization cross sections and asymmetry parameters: $1 < Z < 103$," *Atomic Data and Nuclear Data Tables*, vol. 32, pp. 1–155, 1985.

[115] A. Saiki, N. Ishizawa, M. Nobuyasu, and M. Kato, "Structural change of C-rare earth sesquioxides Yb2O3 and Er2O3 as a function of temperature," *Yogyo Kyokai-Shi*, vol. 93, no. 10, pp. 649–654, 1985.

[116] T. Schleid and G. Meyer, "Single crystals of rare earth oxides from reducing halide melts," *Journal of the Less Common Metals*, vol. 149, pp. 73–80, 1989.

[117] C. Artini, M. Pani, J. R. Plaisier, and G. A. Costa, "Structural study of nd oxidation by means of in-situ synchrotron x-ray diffraction (400≤t≤700°c)," *Solid State Ionics*, vol. 257, pp. 38–41, 2014.

[118] M. Zinkevich, "Thermodynamics of rare earth sesquioxides," *Progress in Materials Science*, vol. 52, no. 4, pp. 597–647, 2007.

[119] K. Zeng and D. Zhang, "Recent progress in alkaline water electrolysis for hydrogen production and applications," *Progress in Energy and Combustion Science*, vol. 36, no. 3, pp. 307–326, 2010.

[120] A. Alvarez, A. Bansode, A. Urakawa, A. V. Bavykina, T. A. Wezendonk, M. Makkee, J. Gascon, and F. Kapteijn, "Challenges in the Greener Production of Formates/Formic Acid, Methanol, and DME by Heterogeneously Catalyzed CO_2 Hydrogenation Processes," *Chem Rev*, vol. 117, no. 14, pp. 9804–9838, 2017.

[121] M. E. Dry and G. J. Oosthuizen, "The correlation between catalyst surface basicity and hydrocarbon selectivity in the fischer-tropsch synthesis," *Journal of Catalysis*, vol. 11, no. 1, pp. 18–24, 1968.

[122] D. S. Kim and I. E. Wachs, "Surface chemistry of supported chromium oxide catalysts," *Journal of Catalysis*, vol. 142, pp. 166–171, 1993.

[123] A. Zecchina, C. Lamberti, and S. Bordiga, "Surface acidity and basicity: General concepts," *Catalysis Today*, vol. 41, pp. 169–177, 1998.

[124] M. Haruta, T. Kobayashi, H. Sano, and N. Yamada, "Novel Gold Catalysts for the Oxidation of Carbon Monoxide at a Temperature far Below 0 °C," *Chemistry Letters*, vol. 16, no. 2, pp. 405–408, 1987.

[125] P. R. Norton and R. L. Tapping, "Photoelectron spectroscopic studies of the adsorption of CO and CO_2 on nickel, platinum, and copper," *Chemical Physics Letters*, vol. 38, no. 207-212, 1976.

[126] W. T. Wallace and R. L. Whetten, "Coadsorption of CO and O_2 on Selected Gold Clusters: Evidence for Efficient Room-Temperature CO_2 Generation," *J Am Chem Soc*, vol. 124, pp. 7499–7505, 2002.

[127] L. M. Molina and B. Hammer, "Active Role of Oxide Support during CO Oxidation at Au/MgO," *Physical Review Letters*, vol. 90, no. 20, p. 206102, 2003.

[128] H. Falsig, B. Hvolboek, I. S. Kristensen, T. Jiang, T. Bligaard, C. H. Christensen, and J. K. Noerskov, "Trends in the catalytic CO oxidation activity of nanoparticles," *Angew Chem Int Ed*, vol. 47, no. 26, pp. 4835–4839, 2008.

[129] H. J. Freund, G. Meijer, M. Scheffler, R. Schlogl, and M. Wolf, "CO oxidation as a prototypical reaction for heterogeneous processes," *Angew Chem Int Ed Engl*, vol. 50, no. 43, pp. 10064–94, 2011.

[130] M. A. van Spronsen, J. W. M. Frenken, and I. M. N. Groot, "Surface science under reaction conditions: CO oxidation on Pt and Pd model catalysts," *Chem Soc Rev*, vol. 46, no. 14, pp. 4347–4374, 2017.

[131] N. K. Soliman, "Factors affecting CO oxidation reaction over nanosized materials: A review," *Journal of Materials Research and Technology*, vol. 8, no. 2, pp. 2395–2407, 2019.

[132] R. Zanella, S. Giorgio, C.-H. Shin, C. R. Henry, and C. Louis, "Characterization and reactivity in CO oxidation of gold nanoparticles supported on TiO_2 prepared by deposition-precipitation with NaOH and urea," *Journal of Catalysis*, vol. 222, pp. 357–367, 2004.

[133] R. Dirsyte, J. Schwarzkopf, G. Wagner, R. Fornari, J. Lienemann, M. Busch, and H. Winter, "Thermal-induced change in surface termination of DyScO3(110)," *Surface Science*, vol. 604, pp. 21–22, 2010.

[134] J. E. Kleibeuker, G. Koster, W. Siemons, D. Dubbink, B. Kuiper, J. L. Blok, C.-H. Yang, J. Ravichandran, R. Ramesh, J. E. ten Elshof, D. H. A. Blank, and

G. Rijnders, "Atomically defined rare-earth scandate crystal surfaces," *Advanced Functional Materials*, vol. 20, pp. 3490–3496, 2010.

[135] A. Biswas, C.-H. Yang, R. Ramesh, and Y. H. Jeong, "Atomically flat single terminated oxide substrate surfaces," *Progress in Surface Science*, vol. 92, no. 2, pp. 117–141, 2017.

[136] P. Koirala, C. A. Mizzi, and L. D. Marks, "Direct Observation of Large Flexoelectric Bending at the Nanoscale in Lanthanide Scandates," *Nano Letters*, vol. 18, no. 6, pp. 3850–3856, 2018.

[137] C. A. Mizzi, P. Koirala, A. Gulec, and L. D. Marks, "Charging ain't all bad: Complex physics in $DyScO_3$," *Ultramicroscopy*, vol. 203, pp. 119–124, 2019.

[138] L. D. Marks and D. J. Smith, "High resolution studies of small particles of gold and silver. I. Multiply-twinned particles," *Journal of Crystal Growth*, vol. 54, no. 3, pp. 425–432, 1981.

[139] D. J. Smith and L. D. Marks, "High resolution studies of small particles of gold and silver. II. Single crystals, lamellar twins and polyparticles," *Journal of Crystal Growth*, vol. 54, no. 3, pp. 433–438, 1981.

[140] L. D. Marks and L. Peng, "Nanoparticle shape, thermodynamics and kinetics," *Journal of Physics: Condensed Matter*, vol. 28, no. 5, p. 053001, 2016.

[141] Z. R. Mansley and L. D. Marks, "Modified Winterbottom Construction Including Boundaries," *Journal of Physical Chemistry C*, vol. 124, no. 51, pp. 28038–28043, 2020.

[142] R. Meyer, C. Lemire, S. K. Shaikhutdinov, and H.-J. Freund, "Surface chemistry of catalysis by gold," *Gold Bulletin (London, United Kingdom)*, vol. 37, no. 1-2, pp. 72–124, 2004.

[143] E. Kampshoff, E. Haln, and K. kern, "Correlation between surface stress and the vibrational shift of CO chemisorbed on Cu surfaces," *Physical Review Letters*, vol. 73, no. 5, pp. 704–707, 1994.

[144] M. Gsell, P. Jakob, and D. Menzel, "Effect of substrate strain on adsorption," *Science*, vol. 280, no. 5364, p. 5364, 1998.

[145] M. Escudero-Escribano, P. Malacrida, M. H. Hansen, U. G. Vej-Hansen, A. Velazquez-Palenzuela, V. Tripkovic, J. Schiotz, J. Rossmeisl, I. E. L. Stephens,

and I. Chorkendorff, "Tuning the activity of Pt alloy electrocatalysts by means of the lanthanide contraction," *Science*, vol. 352, no. 6281, pp. 73–76, 2016.

[146] B. Hammer and J. K. Norskov, "Why gold is the noblest of all the metals," *Nature*, vol. 376, no. 6537, pp. 238–240, 1995.

[147] L. M. Molina, M. D. Rasmussen, and B. Hammer, "Adsorption of O2 and oxidation of CO at Au nanoparticles supported by TiO_2(110)," *Journal of Chemical Physics*, vol. 120, no. 16, pp. 7673–7680, 2004.

[148] P. Schlexer, D. Widmann, R. J. Behm, and G. Pacchioni, "CO Oxidation on a Au/TiO_2 Nanoparticle Catalyst via the Au-Assisted Mars-van Krevelen Mechanism," *ACS Catalysis*, vol. 8, no. 7, pp. 6513–6525, 2018.

[149] H. Y. Kim and G. Lee, Hyuck MoHenkelman, "CO Oxidation Mechanism on CeO_2-Supported Au Nanoparticles," *Journal of the American Chemical Society*, vol. 134, no. 3, pp. 1560–1570, 2012.

[150] P. C. S. f. C. 5460578, "Oxidoperoxidocarbonate(.1-).," *National Center for Biotechnology Information*, 2021.

[151] H. Huber, D. McIntosh, and G. A. Ozin, "A metal atom model for the oxidation of carbon monoxide to carbon dioxide. The gold atom-carbon monoxide-dioxygen reaction and the gold atom-carbon dioxide reaction," *Inorganic Chemistry*, vol. 16, no. 5, pp. 975–979, 1977.

[152] J. Hagen, L. D. Socaciu, M. Elijazyfer, U. Heiz, T. M. Bernhardt, and L. Wöste, "Coadsorption of CO and O_2 on small free gold cluster anions at cryogenic temperatures: Model complexes for catalytic CO oxidation," *Physical Chemistry Chemical Physics*, vol. 4, no. 10, pp. 1707–1709, 2002.

[153] B. Hammer, "Special Sites at Noble and Late Transition Metal Catalysts," *Topics in Catalysis*, vol. 37, no. 1, pp. 3–16, 2006.

[154] I. Langmuir, "The mechanism of the catalytic action of platinum in the reactions $2CO + 0_2 = 2C0_2$ and $2H_2 + 02 = 2H_2O$," *Trans. Faraday Soc.*, vol. 17, pp. 621–654, 1922.

[155] J. L. Gland, "The adsorption of oxygen on a stepped platinum single crystal surface," *Surface Science*, vol. 75, pp. 733–750, 1978.

[156] D. Y. Wei, M. F. Yue, S. N. Qin, S. Zhang, Y. F. Wu, G. Y. Xu, H. Zhang, Z. Q. Tian, and J. F. Li, "In Situ Raman Observation of Oxygen Activation and

Reaction at Platinum-Ceria Interfaces during CO Oxidation," *J Am Chem Soc*, vol. 143, no. 38, pp. 15635–15643, 2021.

[157] A. D. Allian, K. Takanabe, K. L. Fujdala, X. Hao, T. J. Truex, J. Cai, C. Buda, M. Neurock, and E. Iglesia, "Chemisorption of CO and mechanism of CO oxidation on supported platinum nanoclusters," *J Am Chem Soc*, vol. 133, no. 12, pp. 4498–517, 2011.

[158] K. Ding, A. Gulec, A. M. Johnson, N. M. Schweitzer, G. D. Stucky, L. D. Marks, and P. C. Stair, "Identification of active sites in CO oxidation and water-gas shift over supported Pt catalysts," *Science*, vol. 350, no. 6257, pp. 189–192, 2015.

[159] J. T. Kummer, "Catalysts for automobile emission control," *Progress in Energy and Combustion Science*, vol. 6, no. 2, pp. 177–199, 1980.

[160] J. Kašpar, P. Fornasiero, and N. Hickey, "Automotive catalytic converters: Current status and some perspectives," *Catalysis Today*, vol. 77, pp. 419–449, 2003.

[161] O. Korotkikh and R. Farrauto, "Selective catalytic oxidation of CO in H_2: fuel cell applications," *Catalysis Today*, vol. 62, pp. 249–254, 2000.

[162] R. Farrauto, S. Hwang, L. Shore, W. Ruettinger, J. Lampert, T. Giroux, Y. Liu, and O. Ilinich, "New material needs for hydrocarbon fuel processing: Generating hydrogen for the PEM fuel cell," *Annual Review of Materials Research*, vol. 33, pp. 1–27, 2003.

[163] S. Wang, E. Zhu, Y. Huang, and H. Heinz, "Direct correlation of oxygen adsorption on platinum-electrolyte interfaces with the activity in the oxygen reduction reaction," *Science Advances*, vol. 7, no. 24, p. eabb1435, 2021.

[164] S. Saeidi, N. A. S. Amin, and M. R. Rahimpour, "Hydrogenation of CO_2 to value-added products—A review and potential future developments," *Journal of CO2 Utilization*, vol. 5, pp. 66–81, 2014.

[165] D. B. Bukur, B. Todic, and N. Elbashir, "Role of water-gas-shift reaction in fischer–tropsch synthesis on iron catalysts: A review," *Catalysis Today*, vol. 275, pp. 66–75, 2016.

[166] P. Panagiotopoulou, "Hydrogenation of CO_2 over supported noble metal catalysts," *Applied Catalysis A: General*, vol. 542, pp. 63–70, 2017.

[167] S. Saeidi, F. Fazlollahi, S. Najari, D. Iranshahi, J. J. Klemeš, and L. L. Baxter, "Hydrogen production: Perspectives, separation with special emphasis on kinetics

of WGS reaction: A state-of-the-art review," *Journal of Industrial and Engineering Chemistry*, vol. 49, pp. 1–25, 2017.

[168] S. R. Janbarari and A. Taheri Najafabadi, "Simulation and optimization of water gas shift process in ammonia plant: Maximizing CO conversion and controlling methanol byproduct," *International Journal of Hydrogen Energy*, vol. 48, no. 64, pp. 25158–25170, 2023.

[169] M. Gattrell, N. Gupta, and A. Co., "A review of the aqueous electrochemical reduction of CO_2 to hydrocarbons at copper," *Journal of Electroanalytical Chemistry*, vol. 594, no. 1, pp. 1–19, 2006.

[170] P. R. Norton, "An investigation of the adsorption of oxygen and oxygen containing species on platinum by photoelectron spectroscopy," *Surface Science*, vol. 47, no. 1, pp. 98–114, 1975.

[171] Z. R. Mansley, *Identifying Support Effects in Nanoparticle Catalysis*. Thesis, Northwestern University, 2021.

[172] G. Chen, C. Xu, X. Huang, J. Ye, L. Gu, G. Li, Z. Tang, B. Wu, H. Yang, Z. Zhao, Z. Zhou, G. Fu, and N. Zheng, "Interfacial electronic effects control the reaction selectivity of platinum catalysts," *Nat Mater*, vol. 15, no. 5, pp. 564–9, 2016.

[173] H. Eyring and M. Polanyi, "On Simple Gas Reactions," *Zeitschrift für Physikalische Chemie*, vol. 227, no. 11, pp. 1221–1246, 1931.

[174] M. Evans and P. M, "Some applications of the transition state method to the calculation of reaction velocities, especially in solution," *Trans. Faraday Soc.*, vol. 31, pp. 875–894, 1935.

[175] B. Peters, N. E. R. Zimmermann, G. T. Beckham, J. W. Tester, and B. L. Trout, "Path Sampling Calculation of Methane Diffusivity in Natural Gas Hydrates from a Water-Vacancy Assisted Mechanism," *Journal of the American Chemical Society*, vol. 130, no. 51, pp. 17342–17350, 2008.

[176] R. S. Mulliken, "Molecular compounds and their spectra. ii," *J. Phys. Chem.*, vol. 74, pp. 811–824, 1952.

[177] R. S. Mulliken, "Molecular Compounds and their Spectra. III. The Interaction of Electron Donors and Acceptors," *J. Phys. Chem.*, vol. 56, no. 7, pp. 801–822, 1952.

[178] D. Koch, Y. Chen, P. Golub, and S. Manzhos, "Revisiting pi backbonding: the influence of d orbitals on metal-CO bonds and ligand red shifts," *Phys Chem Chem Phys*, vol. 21, no. 37, pp. 20814–20821, 2019.

[179] J. Wm. Curtis Conner, "A General Explanation for the Compensation Effect: The Relationship between $\Delta S^{\ddagger}$ and Activation Energy," *Journal of Catalysis*, vol. 78, pp. 238–246, 1982.

[180] R. C. Peterson, "The Linear Relationship between Enthalpy and Entropy of Activation," *The Journal of Organic Chemistry*, vol. 29, no. 11, pp. 3133–3135, 1964.

[181] L. Liu and Q.-X. Guo, "Isokinetic relationship, isoequilibrium relationship, and enthalpy-entropy compensation," *Chem Rev*, vol. 101, pp. 673–695, 2001.

[182] J. C. Phillips, "Enthalpy/Entropy and Volume/Entropy Activation Ratios and Solute-Solvent Interactions," *The Journal of Physical Chemistry*, vol. 89, pp. 3060–3066, 1985.

[183] A. Pan, T. Biswas, A. K. Rakshit, and S. P. Moulik, "Enthalpy-Entropy Compensation (EEC) Effect: A Revisit," *J Phys Chem B*, vol. 119, no. 52, pp. 15876–84, 2015.

[184] L.-J. Chen, "Effect of Hydrophobic Chain Length of Surfactants on Enthalpy-Entropy Compensation of Micellization," *J Phys Chem B*, vol. 102, pp. 4350–4356, 1998.

[185] M. Y. Nie, L. M. Zhou, X. L. Liu, Q. H. Wang, and D. Q. Zhu, "Separation of the Enantiomers of 2-Phenylcyclopropane- carboxylate Esters by Capillary Gas Chromatography on Derivatized Cyclodextrin Stationary Phases," *Chromatographia*, vol. 51, pp. 450–454, 2000.

[186] A. K. Galwey, D. G. Bettany, and M. Mortimer, "Kinetic compensation effects observed during oxidation of carbon monoxide on γ-alumina supported palladium, platinum, and rhodium metal catalysts: Toward a mechanistic explanation," *International Journal of Chemical Kinetics*, vol. 38, no. 11, pp. 689–702, 2006.

[187] A. Balla, C. Marcu, and J.-Z. Szücs-Balázs, "Compensation Effect in Catalytic Oxidation of Carbon Monoxide," *Chemical Engineering I& Technology*, vol. 46, no. 2, pp. 410–414, 2022.

[188] R. E. Lyon, "Isokinetics," *J Phys Chem A*, vol. 123, no. 12, pp. 2462–2469, 2019.

[189] H. J. Kreuzer and N. H. March, "Origin and information content of the compensation effect," *Theoretica Chimica Acta*, vol. 74, pp. 339–348, 1988.

[190] A. K. Galwey and M. Mortimer, "Compensation effects and compensation defects in kinetic and mechanistic interpretations of heterogeneous chemical reactions," *International Journal of Chemical Kinetics*, vol. 38, no. 7, pp. 464–473, 2006.

[191] S. Bessel, "Support effects in cobalt-based Fischer-Tropsch catalysis," *Applied Catalysis A: General*, vol. 96, pp. 253–268, 1993.

[192] M. Shekhar, J. Wang, W. S. Lee, W. D. Williams, S. M. Kim, E. A. Stach, J. T. Miller, W. N. Delgass, and F. H. Ribeiro, "Size and support effects for the water-gas shift catalysis over gold nanoparticles supported on model Al2O3 and TiO2," *J Am Chem Soc*, vol. 134, no. 10, pp. 4700–8, 2012.

[193] N. M. Markovic, T. J. Schmidt, V. Stamenkovic, and P. N. Ross, "Oxygen Reduction Reaction on Pt and Pt Bimetallic Surfaces: A Selective Review," *Fuel Cells*, vol. 1, no. 2, pp. 105–116, 2001.

[194] D. Mott, J. Luo, P. N. Njoki, Y. Lin, L. Y. Wang, and C. J. Zhong, "Synergistic activity of gold-platinum alloy nanoparticle catalysts," *Catalysis Today*, vol. 122, pp. 378–385, 2007.

[195] A. K. Singh and Q. Xu, "Synergistic catalysis over bimetallic alloy nanoparticles," *ChemCatChem*, vol. 5, no. 3, pp. 652–676, 2013.

[196] M. A. Aramendia, J. A. Benitez, V. Borau, C. Jimenez, J. M. Marinas, and A. Moreno, "Dehydrogenation of cyclohexane over Pt/SiO_2-$AlPO_4$ catalysts .1. Influence of the catalyst particle size," *React Kinet Catal L*, vol. 62, no. 1, pp. 23–31, 1997.

[197] C. T. Campbell, S. C. Parker, and D. E. Starr, "The effect of size-dependent nanoparticle energetics on catalyst sintering," *Science*, vol. 298, pp. 811–814, 2002.

[198] H. L. Ye, S. X. Liu, C. Zhang, Y. Q. Cai, and Y. F. Shi, "Dehydrogenation of methylcyclohexane over Pt-based catalysts supported on functional granular activated carbon," *RSC Adv*, vol. 11, no. 47, pp. 29287–29297, 2021.

[199] W. H. Qi, M. P. Wang, and Y. C. Su, "Size effect on the lattice parameters of nanoparticles," *Journal of Materials Science Letters*, vol. 21, pp. 877–878, 2002.

[200] W. H. Qi and M. P. Wang, "Size and shape dependent lattice parameters of metallic nanoparticles," *Journal of Nanoparticle Research*, vol. 7, no. 1, pp. 51–57, 2005.

[201] K. I. Hadjiivanov and G. N. Vayssilov, "Characterization of Oxide Surfaces and Zeolites by Carbon Monoxide as an IR Probe Molecule," *Adv Catal*, vol. 47, pp. 307–511, 2002.

[202] B. H. Toby and R. B. V. Dreele, "GSAS-II: the genesis of a modern open-source all purpose crystallography software package," *Journal of Applied Crystallography*, vol. 46, pp. 544–549, 2013.

[203] C. T. Schamp and W. A. Jesser, "On the measurement of lattice parameters in a collection of nanoparticles by transmission electron diffraction," *Ultramicroscopy*, vol. 103, no. 2, pp. 165–72, 2005.

[204] K. H. Hong, G. M. McNally, M. Coduri, and J. P. Attfield, "Synthesis, crystal structure, and magnetic properties of $MnFe_3O_5$," *Zeitschrift fuer Anorganische und Allgemeine Chemie*, vol. 642, no. 23, pp. 1355–1358, 2016.

[205] H. J. Wasserman and J. S. Vermaak, "On the determination of the surface stress of copper and platinum," *Surface Science*, vol. 32, pp. 168–174, 1972.

[206] J. R. Gallagher, T. Li, H. Zhao, J. Liu, Y. Lei, X. Zhang, Y. Ren, J. W. Elam, R. J. Meyer, R. E. Winans, and J. T. Miller, "In situ diffraction of highly dispersed supported platinum nanoparticles," *Catal. Sci. Technol.*, vol. 4, no. 9, pp. 3053–3063, 2014.

[207] J. S. Vermaak, C. W. Mays, and D. Kuhlmann-Wilsdorf, "On surface stress and surface tension i. theoretical considerations," *Surface Science*, vol. 12, pp. 128–133, 1968.

[208] L. Greco, M. Cuomo, and L. Contrafatto, "A reconstructed local $\bar{B}$ formulation for isogeometric Kirchhoff–Love shells," *Computer Methods in Applied Mechanics and Engineering*, vol. 332, pp. 462–487, 2018.

[209] A. D. Andreev, J. R. Downes, D. A. Faux, and E. P. O'Reilly, "Strain distributions in quantum dots of arbitrary shape," *Journal of Applied Physics*, vol. 86, no. 1, pp. 297–305, 1999.

[210] I. J. McPherson, P. A. Ash, L. Jones, A. Varambhia, R. M. J. Jacobs, and K. A. Vincent, "Electrochemical CO Oxidation at Platinum on Carbon Studied through Analysis of Anomalous in Situ IR Spectra," *J Phys Chem C Nanomater Interfaces*, vol. 121, no. 32, pp. 17176–17187, 2017.

[211] P. B. Wells, "Characterization of the standard platinum/silica catalyst europt-1.5. chemisorption of carbon monoxide and of oxygen," *Applied Catalysis*, vol. 18, pp. 259–272, 1985.

[212] C. Lentz, S. P. Jand, J. Melke, C. Roth, and P. Kaghazchi, "DRIFTS study of CO adsorption on Pt nanoparticles supported by DFT calculations," *Journal of Molecular Catalysis A: Chemical*, vol. 426, pp. 1–9, 2017.

[213] M. Favaro, H. Xiao, T. Cheng, r. Goddard, W. A., J. Yano, and E. J. Crumlin, "Subsurface oxide plays a critical role in CO_2 activation by Cu(111) surfaces to form chemisorbed CO_2, the first step in reduction of CO_2," *Proc Natl Acad Sci U S A*, vol. 114, no. 26, pp. 6706–6711, 2017.

[214] B. Hammer, Y. Morikawa, and J. K. Nørskov, "CO Chemisorption at Metal Surfaces and Overlayers," *Physical Review Letters*, vol. 76, pp. 2141–2144, 1996.

[215] M. Mavrikakis, B. Hammer, and J. K. Nørskov, "Effect of strain on the reactivity of metal surfaces," *Physical Review Letters*, vol. 81, no. 13, pp. 2819–2822, 1998.

[216] M. T. Gorzkowski and A. Lewera, "Probing the Limits of d-Band Center Theory: Electronic and Electrocatalytic Properties of Pd-Shell–Pt-Core Nanoparticles," *The Journal of Physical Chemistry C*, vol. 119, no. 32, pp. 18389–18395, 2015.

[217] L. Grabow, Y. Xu, and M. Mavrikakis, "Lattice strain effects on CO oxidation on Pt(111)," *Phys Chem Chem Phys*, vol. 8, no. 29, pp. 3369–74, 2006.

[218] F. Liu, C. Wu, G. Yang, and S. Yang, "CO Oxidation over Strained Pt(100) Surface: A DFT Study," *The Journal of Physical Chemistry C*, vol. 119, no. 27, pp. 15500–15505, 2015.

[219] R. F. W. Bader, "A Quantum Theory of Molecular Structure and Its Applications," *Chem Rev*, vol. 91, pp. 893–928, 1991.

[220] R. F. W. Bader, "The Quantum Mechanical Basis of Conceptual Chemistry," *Monatshefte für Chemie - Chemical Monthly*, vol. 136, no. 6, pp. 819–854, 2005.

[221] R. F. W. Bader, *Atoms in Molecules - A quantum theory*. New York: Oxford University Press, 1990.

[222] HenkelmanGroup, "Bader charge analysis."

[223] V. J. Cybulskis, J. Wang, J. H. Pazmiño, F. H. Ribeiro, and W. N. Delgass, "Isotopic transient studies of sodium promotion of Pt/Al_2O_3 for the water–gas shift reaction," *Journal of Catalysis*, vol. 339, pp. 163–172, 2016.

[224] L. J. Santos, F. L. Bobadilla, A. M. Centeno, and A. J. Odriozola, "Operando DRIFTS-MS Study of WGS and rWGS Reaction on Biochar-Based Pt Catalysts: The Promotional Effect of Na.," *C — Journal of Carbon Research*, vol. 4, p. 47, 2018.

[225] M. T. Dove, M. G. Tucker, and D. A. Keen, "Neutron total scattering method: a simultaneous determination of long-range and short-range order in disordered materials," *Eur. J. Mineral*, vol. 14, pp. 331–348, 2004.

[226] S. J. L. Billinge, "The rise of the X-ray atomic pair distribution function method: a series of fortunate events," *Phil. Trans. R. Soc. A.*, vol. 377, p. 20180413, 2019.

[227] E. Asenath-Smith, H. Li, E. C. Keene, Z. W. Seh, and L. A. Estroff, "Crystal growth of calcium carbonate in hydrogels as a model of biomineralization," *Advanced Functional Materials*, vol. 22, p. 2891–2914, 2012.

[228] M. C. Robert and F. Lefaucheux, "Crystal growth in gels: Principle and applications," *Journal of Crystal Growth*, vol. 90, pp. 358–367, 1988.

[229] H. K. Henisch, *Crystals in Gels and Liesegang Rings*. Cambrige CB2 1BP: Cambridge University Press, 1988.

[230] M. Hÿtch, F. Houdellier, F. Hüe, and E. Snoeck, "Nanoscale holographic interferometry for strain measurements in electronic devices," *Nature*, vol. 453, p. 1086–1089, 2008.

[231] K. Harada, "Interference and interferometry in electron holography," *Microscopy*, vol. 70, pp. 3–16, 2021.

[232] P. F. Long and B. C. Smith, "Ionization energies of lanthanides," *Journal of Chemical Education*, vol. 87, pp. 875–881, 2010.

[233] V. M. Goldschmidt, "Die gesetze der krystallochemie," *Die Naturwissenschaften*, vol. 14, p. 477–485, 1926.

[234] C. M. Culbertson, A. T. Flak, M. Yatskin, P. H.-Y. Cheong, D. P. Cann, and M. R. Dolgos, "Neutron total scattering studies of group II titanates (ATiO3, A2+ = Mg, Ca, Sr, Ba)," *Scientific Reports*, vol. 10, no. 1, pp. 1–10, 2020.

[235] C. J. Bartel, C. Sutton, B. R. Goldsmith, R. Ouyang, C. B. Musgrave, L. M. Ghiringhelli, and M. Scheffler, "New tolerance factor to predict the stability of perovskite oxides and halides," *Science Advances*, vol. 5, no. 2, p. eaav069, 2019.

[236] B. Morosin, R. Baughman, D. Ginley, and M. Butler, "The influence of crystal structure on the photoresponse of iron-titanium oxide electrodes," *Journal of Applied Crystallography*, vol. 11, pp. 121–124, 1978.

[237] J. A. Linton, Y. Fei, and A. Navrotsky, "The $MgTiO_3$-$FeTiO_3$ join at high pressure and temperature," *American Mineralogist*, vol. 84, no. 10, pp. 1595–1603, 1999.

[238] W. D. Nesse, *Introduction to mineralogy*. New York: Oxford University Press, 2000.

[239] S. Burger, M. G. Ehrenreich, and G. Kieslich, "Tolerance factors of hybrid organic-inorganic perovskites: recent improvements and current state of research," *J. Mater. Chem.*, vol. 6, pp. 21785–21793, 2018.

[240] M. Liang, W. Lin, Z. Lan, J. Meng, Q. Zhao, X. Zou, I. E. Castelli, T. Pullerits, S. E. Canton, and K. Zheng, "Electronic Structure and Trap States of Two-Dimensional Ruddlesden–Popper Perovskites with the Relaxed Goldschmidt Tolerance Factor," *ACS Appl Electron Mater*, vol. 2, pp. 1402–1412, 2020.

[241] R. D. Shannon, "Revised effective ionic radii and systematic studies of interatomic distances in halides and chalcogenides," *Acta Crystallographica*, vol. A32, pp. 751–767, 1976.

[242] R. Uecker, H. Wilke, D. G. Schlom, B. Velickov, P. Reiche, A. Polity, M. Bernhagen, and M. Rossberg, "Spiral formation during Czochralski growth of rare-earth scandates," *Journal of Crystal Growth*, vol. 295, pp. 84–91, 2006.

[243] J. B. Clark, P. W. Richter, and L. D. Toit, "High-pressure synthesis of $YScO_3$, $HoScO_3$, $ErScO_3$, and $TmScO_3$, and a reevaluation of the lattice constants of the rare earth scandates," *Journal of Solid State Chemistry*, vol. 23, pp. 129–134, 1978.

[244] T. Heeg, M. Roeckerath, J. Schubert, W. Zander, C. Buchal, H. Y. Chen, C. L. Jia, Y. Jia, C. Adamo, and D. G. Schlom, "Epitaxially stabilized growth of $LuScO_3$ orthorhombic thin films," *Applied Physics Letters*, vol. 90, p. 192901, 2007.

[245] D. Gruen, W. Koehler, and J. Katz, "Higher Oxides of the Lanthanide Elements. Terbium Dioxide," *Journal of the American Chemical Society*, vol. 73, pp. 1475–1479, 1951.

[246] M. Badlani and I. E. Wachs, "Methanol: a "smart" chemical probe molecule," *Catalysis Letters*, vol. 75, no. 3-4, 2001.

[247] G. A. Camara and T. Iwasita, "Parallel pathways of ethanol oxidation: The effect of ethanol concentration," *Journal of Electroanalytical Chemistry*, vol. 578, no. 2, pp. 315–321, 2005.

[248] F. Ksar, L. Ramos, B. Keita, L. Nadjo, P. Beaunier, and H. Remita, "Bimetallic Palladium-Gold Nanostructures: Application in Ethanol Oxidation," *Chemistry of Materials*, vol. 21, no. 15, pp. 3677–3683, 2009.

[249] A. Lilić, T. Wei, S. Bennici, J.-F. Devaux, J.-L. Dubois, and A. Auroux, "A Comparative Study of Basic, Amphoteric, and Acidic Catalysts in the Oxidative Coupling of Methanol and Ethanol for Acrolein Production," *ChemSusChem*, vol. 10, no. 17, pp. 3459–3472, 2017.

[250] L. Mattos and F. Noronha, "Hydrogen production for fuel cell applications by ethanol partial oxidation on Pt/CeO_2 catalysts: the effect of the reaction conditions and reaction mechanism," *Journal of Catalysis*, vol. 233, no. 2, pp. 453–463, 2005.

[251] L. J. Burcham, L. E. Briand, and I. E. Wachs, "Quantification of Active Sites for the Determination of Methanol Oxidation Turn-over Frequencies Using Methanol Chemisorption and in Situ Infrared Techniques. 1. Supported Metal Oxide Catalysts," *Langmuir*, vol. 17, no. 20, 2001.

[252] V. V. Torbina, A. A. Vodyankin, S. Ten, G. V. Mamontov, M. A. Salaev, V. I. Sobolev, and O. V. Vodyankina, "Ag-based catalysts in heterogeneous selective oxidation of alcohols: A review," *Catalysts*, vol. 8, no. 10, 2018.

[253] C. J. Heard, L. Grajciar, F. Uhlík, M. Shamzhy, M. Opanasenko, J. Čejka, and P. Nachtigall, "Zeolite (in)stability under aqueous or steaming conditions," *Advanced Materials*, vol. 32, p. 2003264, 2020.

[254] M. K. Rasmussen, A. S. Foster, B. Hinnemann, F. F. Canova, S. Helveg, K. Meinander, N. M. Martin, J. Knudsen, A. Vlad, E. Lundgren, A. Stierle, F. Besenbacher, and J. V. Lauritsen, "Stable Cation Inversion at the $MgAl_2O_4(100)$ Surface," *Phys Rev Lett*, vol. 107, p. 036102, 2011.

[255] P. F. Ndione, Y. Shi, V. Stevanovic, S. Lany, A. Zakutayev, P. A. Parilla, J. D. Perkins, J. J. Berry, D. S. Ginley, and M. F. Toney, "Control of the electrical properties in spinel oxides by manipulating the cation disorder," *Advanced Functional Materials*, vol. 24, pp. 610–618, 2014.

[256] K. R. Sanchez-Lievanos, J. L. Stair, and K. E. Knowles, "Cation distribution in spinel ferrite nanocrystals: Characterization, impact on their physical properties, and opportunities for synthetic control," *Inorg Chem*, vol. 60, p. 4291–4305, 2021.

[257] E. Wang, R. Uppuluri, B. J. Kwon, E. Sarnello, S. Lapidus, and B. Key, "Structural Characterization and Electrochemical Performance of Spinel Oxide Cathodes for High Voltage Mg-Ion Batteries," in *244th ECS Meeting*, ECS, 2023.

APPENDIX A

Hydrosauna Synthesis Observations via In-Situ X-Ray Diffraction

In-situ XRD experiments in this section were done in Northwestern's J. B. Cohen X-Ray Facility under the direction of J. Carsello and E. Goldfine. A Smartlab 9kW Gen3 diffractometer was used in the Bragg-Brentano geometry with a source wavelength of 1.5406 Å. The chamber was loaded with $NdScO_3$ precursor gel, heated to 450, 600, or 750°C at a rate of 5°C/min, and held at each temperature for 12 hours. Dry nitrogen gas was passed through a water bubbler and then flowed through the sample chamber at a rate of 50 mL/min to approximate the hydrosauna condition as closely as possible. The experimental set-up can be visualized from Figure A.1. An illustration of the position of the sample within the chamber is shown in Figure A.1(a), where the $NdScO_3$ precursor gel (pale blue) is piled onto the alumina stage at such a height that it will not interfere with instrumentation in the chamber. Figure A.1(b) is a photograph of the gel in the sample holder before synthesis; the top surface of the gel sits nearly 4 mm above the surface of the sample holder. After calcining according to the hydrosauna method, the resulting product has lost much of the mass and volume of the gel, resulting in the small pellet of powder, about 7 mm across and 2.5 mm thick, photographed in Figure A.1(c).

The precursor gel contains about 75% water by volume on average. It therefore shrinks dramatically throughout calcination. To obtain quality XRD data, the cross section of

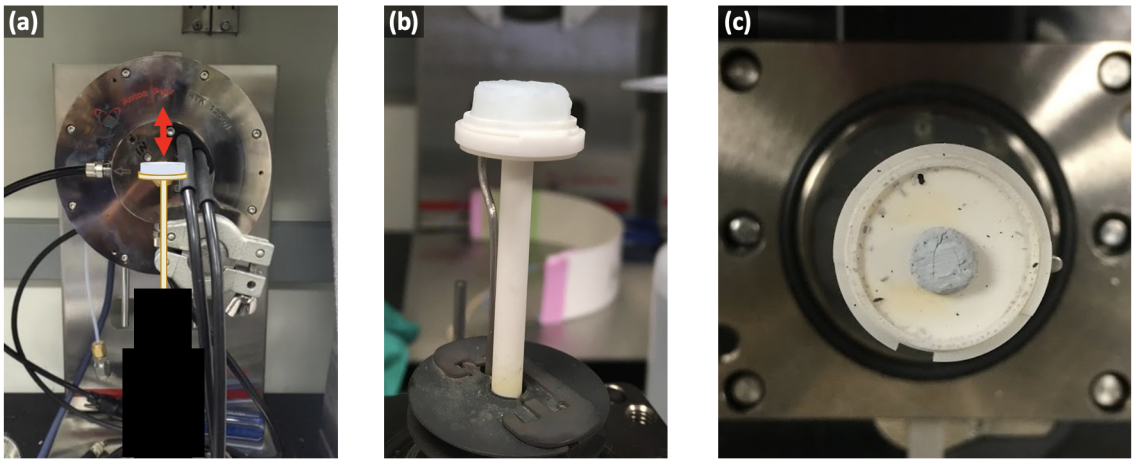

Figure A.1. (a) Illustration of the position of the sample in the sample chamber of the Smartlab 9kW Gen3 diffractometer. (b) Photograph of the $NdScO_3$ precursor gel, $NdSc(OH)_6 \cdot xH_2O$, in its alumina sample holder before calcining. (c) Sample, $NdScO_3$ powder, in its alumina sample holder after calcining at 750 °C for 12 hours.

the X-ray beam incident upon the sample, which is around 10 mm in the described configuration, should be filled entirely with sample after calcining. However, the permissible volume of loaded precursor material is determined by the geometry of the sample chamber, which is not configured to accommodate materials of dramatically changing size. Thus, not enough material can be loaded into the sample chamber such that a quantity of material sufficient to cover the beam footprint remains after calcination, as shown in Figure A.1(c).

For the reflectance geometry and diffractometer used, there are some workarounds that can account for the sample's shape change during heating. First, one should pack the gel in a uniform shape with as flat a top as possible, hence the configuration shown in Figure A.1(b). This ensures that the diffractometer is aligned to the surface of the

sample holder, rather than the surface of the gel, thus maximizing the accessible ratio of sample size to beam cross section.

However, these adjustments ultimately did not allow for a successful in-situ XRD monitoring of a $LnScO_3$ hydrosauna synthesis. The results of a representative experiment are shown in Figure A.2, following diffraction patterns as a function of time throughout heating from room temperature to 750°C. We start with the largely amorphous pattern of the gel at room temperature, though it is important to note that at this early time, the diffractometer is aligned to the sample holder surface rather than the gel surface (as previously described), which reduces the signal of scattering from the gel. By about 100°C, the diffraction pattern clearly displays the peaks associated with the alumina sample holder. Once the sample reaches 750 °C, a peak appears at about 31°, where one would expect a cluster of peaks in the $NdScO_3$ pattern.

Ex-situ XRD conducted at room temperature in an amorphous (glass) sample holder and shown in the bottom pattern of Figure A.3 revealed the correct phase was synthesized in this experimental set-up. However, during the in-situ experiment there is not enough signal from the powder itself to resolve these peaks separately, nor to identify any others, let alone those from other minority phases or intermediates that may be present.

The loss of such a large fraction of the gel's volume to evaporating water is difficult to accomodate even with other experimental geometries. Aside from the gel's thick, toothpaste-like consistency, which makes capillaries difficult to fill, the shape change that occurs at high temperatures will become especially pronounced when smaller total amounts of material are used. Furthermore, in changing the sample configuration, e.g. by using a capillary or other tightly packed and enclosed holder, the gel packing density

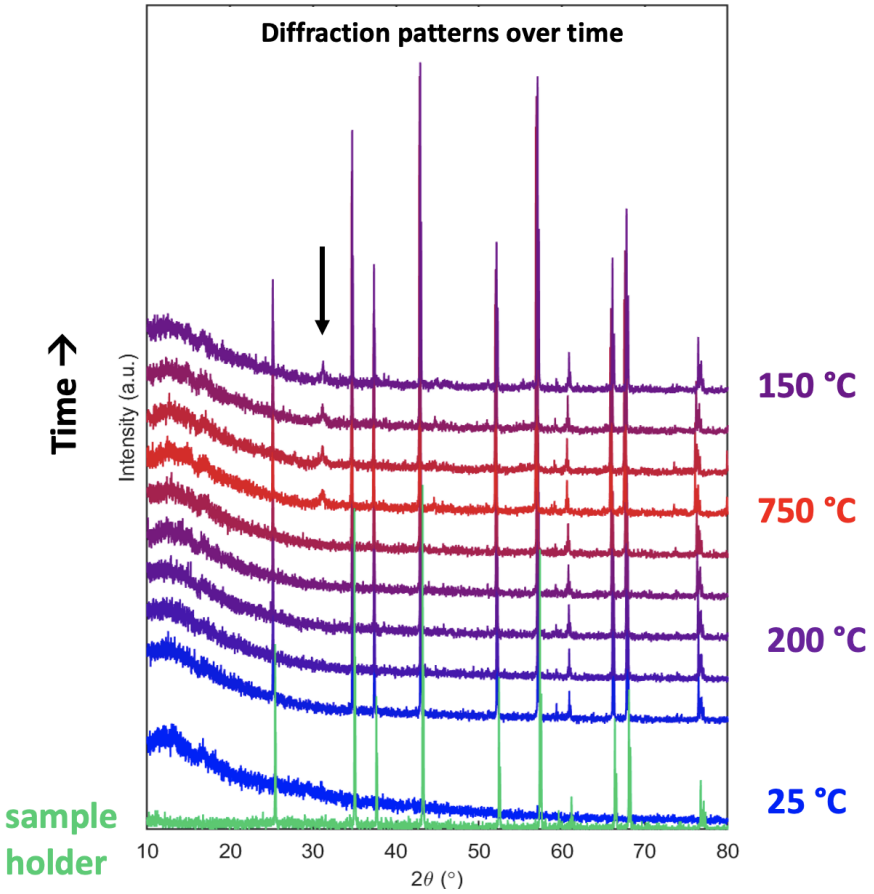

Figure A.2. X-ray diffraction patterns taken throughout heating and cooling of a $NdScO_3$ precursor gel. The green pattern at the bottom is of the empty alumina sample holder. The black arrow indicates a peak at about 31° that is not present in the sample holder pattern and is present in $NdSCO_3$ patterns.

and surface area exposed to flowing gas both alter the gel's water exposure and drying rate. As demonstrated in Chapters 3 and 4, these can hinder crystallization of the desired phase. Keeping the sample in the footprint of the beam and maintaining an appropriate humidity throughout heating would require a specialized experimental set-up beyond the scope of a typical university X-ray lab. A synchrotron source, which can produce a much

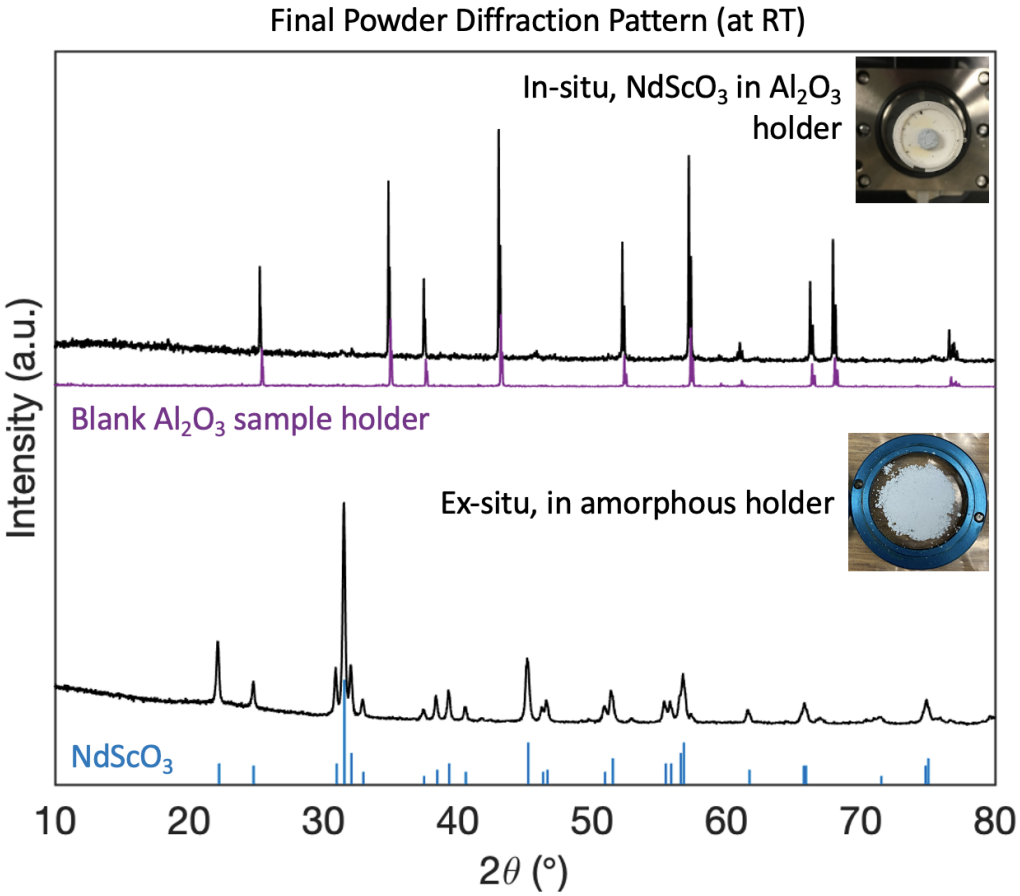

Figure A.3. X-ray diffraction patterns of $NdScO_3$ (top) in-situ at 450 °C during hydrosauna synthesis in an alumina sample holder and (bottom) ex-situ at room temperature in an amorphous sample holder. Ex-situ results show that $NdScO_3$ was formed, though only the diffraction from the ceramic high-temperature sample holder can be resolved in-situ as the gel shrinks.

smaller beam to hit the sample more consistently, may be used instead to greater effect.

See Chapter 8 for further discussion of potential in-situ hydrosauna methods.

APPENDIX B

Effects of Platinum Particle Size on CO DRIFTS

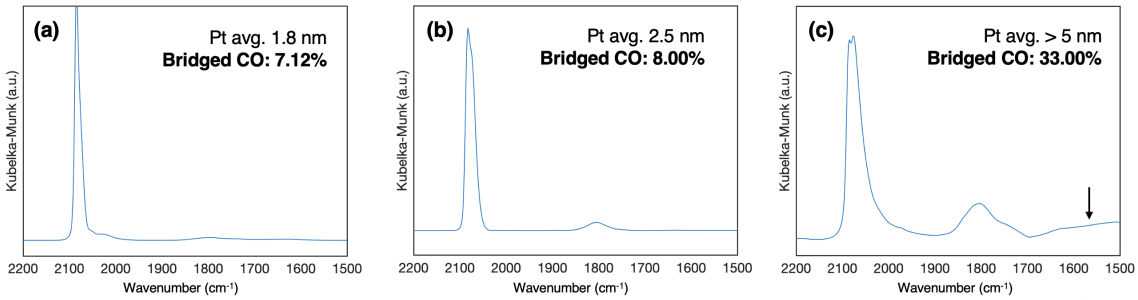

Figure B.1. DRIFTS of $Pt/SmScO_3$ after CO saturation for three different sizes of Pt: (a) Average Pt particle diameter is 1.8 nm, (b) average Pt particle diameter is 2.5 nm, and (c) $Pt/SmScO_3$ was allowed to reduce under H_2/Ar at 400 °C for one hour to induce particle sintering. Post-situ average Pt particle diameter was greater than 5 nm, and the arrow around 1560 cm^{-1} indicates the formation of carbonate species. Pt particle sizes were measured using TEM. As the average Pt size increases, the "linear" CO peak (2100 to 1900 cm^{-1}) broadens, and the fraction of CO bound in a bridged configuration (i.e. atop multiple Pt atoms, 1971 –1770 cm^{-1}) increases.